

https://dspace.org/

Fabrication of polyaniline/indium oxide /onion-like carbon ternary nanocomposite for room tempera ture gas sensing applications

Mathe, Boipelo Nicholette

2022-08
University of the Witwatersrand, Johannesburg
https://hdl.handle.net/10539/38459

Downloaded from a DSpace repository. https://dspace.org/

Fabrication of polyaniline/indium oxide /onion-like carbon ternary nanocomposite for room temperature gas sensing applications

By

Boipelo Nicholette Mathe

A dissertation submitted in fulfilment of the requirements for the degree of

Master of Science in the Faculty of Science

School of Chemistry

University of the Witwatersrand

Private Bag X03

WITS

2050

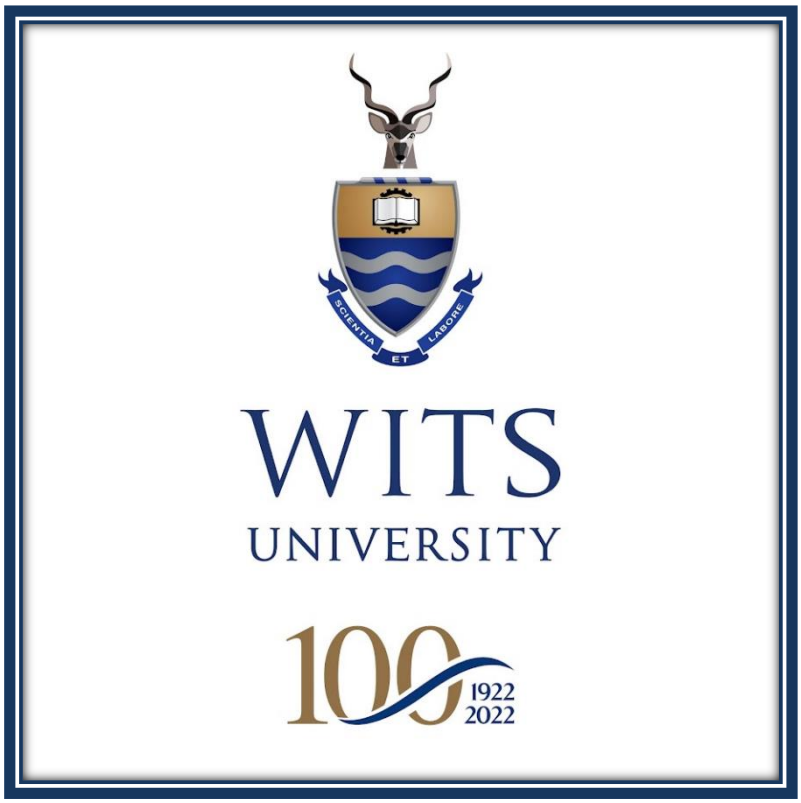
Supervisor: Dr EC Linganiso

Co-supervisor: Dr Z Tetana

Co-supervisor: Dr J Moma

Declaration

I declare that solely I have composed this thesis and that it has not been submitted, in whole or in part, in any previous application for a degree. Except where states otherwise by reference or acknowledgement, the work presented is entirely my own.



Name: Boipelo Nicholette Mathe Date: 15/08/2022

Signature:

Abstract

Monitoring and documenting chemical stimuli or environmental fluctuations is vital to daily health care and environmental monitoring. This objective can be accomplished through the development of high-performance sensors able to detect toxic gases such as ammonia, volatile organic compounds (VOCs) and many more. The modification of carbon nano-onions with metal oxides/conducting polymer could enhance sensing performances at room temperature. This research focuses on the development of a flexible room temperature gas sensor for ammonia sensing with a sensing layer composed of indium oxide (In_2O_3)/onion-like carbons (OLCs)/ polyaniline (PANI). The current sensors were tested at a 40-45 percentage humidity.

Polyaniline was produced utilizing the rapid polymerization technique with aniline and ammonium persulfate as precursors. Carbon nano-onions were obtained by the flame pyrolysis process with candle wax as the carbon source. The present study compared two microwave-assisted solution-phase methods for the synthesis of indium oxides. The first methods produced indium hydroxide ($In(OH)_3$) followed by its conversion to In_2O_3 through annealing at 400 ^oC, and the second used a one-step method where ethanol was used as a solvent instead of water.

Different reaction times were used to determine the effect of microwave power on the indium oxide formed through a solution-phase method, and several characterizations techniques were performed to characterize the products, including transmission electron microscopy, X-ray diffraction, Fourier transform infrared spectroscopy, Raman spectroscopy, scanning electron microscopy, Brunauer-Emmett-Teller, X-ray photoelectron spectroscopy and Ultraviolet-visible spectroscopy.

The ternary In_2O_3/PANI/OLCs nanocomposite was fabricated using physical mixing by adding varying amounts of In_2O_3 to fixed quantities of PANI and OLCs. Using gold-plated interdigitated electrodes (IDEs) embedded on a printed circuit board (PCB) substrate, inexpensive and room temperature functional sensors based on plain PANI, OLCs, OLCs/PANI, and OLCs/PANI/In_2O_3 were developed. The sensors based on ternary composites outperformed of sensors based on pure PANI, OLCs, and PANI/OLCs, due synergic effect of PANI, OLCs and In_2O_3 when combined. The sensor with the highest response among the sensors with the ternary nanocomposite as the sensing layer, was chosen for further evaluations of recovery time, reaction time, repeatability, and selectivity. The sensor containing (4.6 mg) B-In_2O_3/PANI/OLCs was particularly responsive to ammonia in comparison to other analytes (hexane, isopropanol,

and acetone), with the response and recovery durations of 2.2 minutes and 4.3 minutes, respectively, spanning a concentration range of 25 ppm to 125 ppm. Current results showed that In_2O_3 materials can be successfully applied in room temperature gas sensing application and further enhance the sensing response to levels that cannot be obtained when using PANI or OLC individually.

Dedication

This dissertation is dedicated to the all mighty God and my family

Mr R Mathe (Son)

Mr SJ Mathe (Father)

Mrs OE Mathe (Mother)

Acknowledgements

- A special thanks go to God almighty, for his grace, mercy, protection, guidance and undeserved love until to date.
- Special gratitude goes to my supervisors: Dr Ella Cebisa Linganiso, Dr John Moma and Dr Zikhona Tetana, for their supervision throughout my research.
- I would want to express my gratitude to my colleagues for their support and welcoming atmosphere, particularly Dr Pumza Mente, Ms Boitumelo Tlhaole, Ms Khanyisile Masemola, Ms Kamogelo Modisane, Ms Mmamma Sebake, Ms Lindokuhle Magagula, Mr Clinton Masemola and Dr Thomas Mongwe.
- I would like to convey my appreciation to Dr Messai Mamo and Ms Rammike of the University of Johannesburg for their assistance with research.
- Special gratitude goes to the national research foundation (NRF) Thuthuka for funding my research and the School of Chemistry at the University of Witwatersrand for registering me for this degree.

Presentations

- Fabrication of polyaniline-indium oxide nanocomposite for room temperature gas sensing application (**Oral presentation**) SANI virtual conference, September 2021
- Fabrication of polyaniline-indium oxide nanocomposite for room temperature gas sensing applications (**Poster presentation**) NYRS National virtual symposium (***second price***), October 2021
- Fabrication of polyaniline-indium oxide nanocomposite for room temperature gas sensing applications (**poster presentation**) CATSA annual conference (virtual), November 2021

Contents

Declaration		**i**
Abstract		**ii**
Dedication		**iv**
Acknowledgements		**v**
Presentations		**vi**
List of figures		**xiii**
List of tables		**xvi**
Abbreviations		**xvii**
	Chapter 1: Introduction and motivation	**1**
1.1	Introduction	1
1.1.1	A concise summary of the study	1-3
1.2	Aim of research	4
1.3	Objectives of research	4
1.4	Dissertation outline	4-5
1.5	References	6-7
	Chapter 2: Literature review	**8**
2.1	Introduction	8
2.1.1	What are nanomaterials?	8
2.1.2	The Dimensional Classification of Nanomaterials	8-9
2.1.3	Synthesis of nanomaterials	9

2.2	Gas Sensor	10
2.2.1	Characteristics of gas sensors	10-11
2.2.2	Chemiresistive gas sensor	11
2.2.3	Gas sensing mechanism	11-14
2.2.4	Metal oxides as gas sensors	14
2.2.5	Indium oxide	14-15
2.3	Several methods for synthesizing indium oxide	15
2.3.1	Sol-gel	15
2.3.2	Chemical vapour deposition (CVD)	16
2.3.3	Sputtering	16
2.3.4	Hydrothermal/Solvothermal Process	16
2.3.5	Thermal evaporation deposition	16-17
2.4	Microwave synthesis techniques	17
2.4.1	Principle of microwave synthesis	17-18
2.4.2	Advantages of microwave heating over conventional thermal heating	18-19
2.5	Conducting polymers	19
2.5.1	Conducting Polymer Systems Requirements	20-21
2.5.2	Doping of organic polymers	21
2.5.3	Polyaniline (PANI)	22
2.6	Onion-like carbons	23
2.7	Polymer nanocomposite-based sensor	24-25

2.8	References	26-37
	Chapter 3: Microwave-assisted hydrothermal synthesis of In_2O_3 nanostructures and the synthesises of polyaniline	**38**
3.1	Introduction	38-39
3.1.1	Synthesis and characterization of B-In_2O_3 and Y-In_2O_3	39
3.1.2	Procedure for conducting experiments	39
3.1.2.1	Reagents	39
3.1.2.2	Synthesis of Y-In_2O_3	40
3.1.2.3	Synthesis of B-In_2O_3	40
3.1.2.4	Characterization techniques	40
3.1.2.5	Plausible reaction mechanism of Y-In_2O_3 and B-In_2O_3 synthesis	41
3.1.3	Discussion of the findings	41
3.1.3.1	Conversion of In $(OH)_3$ to Y-In_2O_3 at different microwave time exposures.	42
3.1.3.2	XRD analysis	42-43
3.1.3.3	FTIR analysis	44
3.1.3.4	SEM and TEM analysis	44-45
3.1.4	Y-In_2O_3 and B-In_2O_3 comparison	48
3.1.4.1	FTIR analysis	48-49
3.1.4.2	XRD analysis	49-50
3.1.4.3	SEM and EDS analysis	50
3.1.4.4	TEM analysis	51
3.1.4.5	UV-Visible Spectroscopy	51-52

3.1.4.6	BET analysis	52-53
3.1.4.7	XPS analysis	53-54
3.1.5	Conclusion	54-55
3.2	**Synthesis of polyaniline**	55
3.2.1	Introduction	55-57
3.2.2	Procedure for conducting experiments	57
3.2.2.1	Reagents	57
3.2.2.2	Synthesis of HCl doped Polyaniline nanofibers	57-58
3.2.2.3	Characterization techniques	58
3.2.3	Discussion of the findings	58
3.2.3.1	TEM analysis	58-59
3.2.3.2	XRD analysis	59-60
3.2.3.3	FT-IR analysis	60
3.2.3.4	BET analysis	61-62
3.2.3.5	UV-Vis spectroscopic analysis	62-63
3.2.4	Conclusion	63
3.2.5	References	64-73
	Chapter 4: Synthesis and characterization of onion-like carbons	**74**
4.1	Introduction	74-75
4.2	Procedure for conducting experiments	75
4.2.1	Reagents	75-76

4.2.2	Synthesis of OLCs using candlesticks	76
4.2.3	Characterization techniques	77
4.3	Discussion of the findings	77
4.3.1	XRD analysis	77-78
4.3.2	TEM analysis	78-79
4.3.3	SEM analysis	79
4.3.4	BET analysis	80
4.3.5	FT-IR analysis	80-81
4.3.6	Raman spectroscopy analysis	81-82
4.3.7	Thermal stability analysis	82-83
4.4	Conclusion	83
4.5	References	84-86
	Chapter 5: Synthesis and characterization of PANI/In_2O_3/OLCs composite for room temperature gas sensing application	**87**
5.1	Introduction	87-88
5.2	Procedure for conducting experiments	88
5.2.1	Reagents	88
5.2.2	Synthesis of In_2O_3/PANI/OLCs nanocomposite	88-89
5.2.3	The preparation of sensing electrode	89-90
5.2.4	Characterization techniques	90
5.3	Discussion of the findings	90

5.3.1	TEM analysis	90-91
5.3.2	SEM analysis	91-92
5.3.3	XRD analysis	92-93
5.3.4	BET analysis	93-94
5.3.5	FTIR analysis	95
5.3.2	Gas sensing applications	96
5.3.2.1	Plausible sensing mechanism	96
5.3.2.2	Gas sensing measurements	97-98
5.3.2.3	NH_3 sensing performance of In_2O_3/PANI/OLCs nanocomposite	98-99
5.3.2.4	Sensing performance of B-IPC_4	99-100
5.3.2.5	NH_3 sensing performance of Y-In_2O_3 and B-In_2O_3	101
5.4	Conclusion	102
5.5	References	103-105
5.6	Supplementary data	106
	Chapter 6: Conclusions and recommendations	**107**
6.1	General conclusions	107-108
6.2	Recommendations	101-109

List of Figures

Figures		Pages
2.1	Dimensions of nanomaterials	8
2.2	Synthesis of nanomaterials	9
2.3	Graphical illustration of P and N, type sensing behaviour	13
2.4	Crystal structure of (a) I213, (b) Ia3 and R3	15
2.5	Conventional heating (a)vs. (b)Microwave heating	18
2.6	Structural illustration of conducting polymers	19
2.7	Structural illustration of forms of polyaniline	23
2.8	Schematic illustration of Carbon structures with various allotropes	23
3.1.1	Schematic illustration of formation of Y-In_2O_3 and B-In_2O_3	42
3.1.2	XRD patterns of a, In $(OH)_3$ at 10 min, 20 min, 30 min, 45 min ,1hr of microwave radiation and (b) In_2O_3 after annealing indium hydroxides	43
3.1.3	FT-IR spectra of (a) $In(OH)_3$ synthesized under different MW reaction times and (b) In_2O_3 after annealing In_2O_3	44
3.1.4	SEM micrographs of $In(OH)_3$ at different microwave irradiation times (10min-1hr (a_1-e_1)) and the In_2O_3 after annealing indium hydroxides (a_2-e_2)	46
3.1.5	TEM micrographs of $In(OH)_3$ at different microwave irradiation times (10min-1hr (a_1-e_1)) and the In_2O_3 after annealing indium hydroxides (a_2-e_2)	47
3.1.6	FT-IR spectra of Y-In_2O_3 and B-In_2O_3	49
3.1.7	X-ray diffractogram of Y-In_2O_3 and B-In_2O_3	50
3.1.8	SEM micrographs of, (a)Y-In_2O_3 ,(b)B-In_2O_3 and EDS spectra of ,(c) Y-In_2O_3 ,(d) B-In_2O_3	50
3.1.9	TEM micrographs (a), $In(OH)_3$, (b) Y-In_2O_3 and B-In_2O_3	51
3.1.10	UV spectra of (a) Y-In_2O_3 and (b) B-In_2O_3	52
3.1.11	Gas adsorption-desorption isotherm curves and Pore size distribution curve of (a) Y-In_2O_3 and (b) B-In_2O_3	53

3.1.12	XPS (a & b) survey, (c & d) In3d and (e & f) O1s of Y-In_2O_3 and B-In_2O_3	53-54
3.2.1	Doping and de-doping of PANI	56
3.2.2	Graphical illustration of PANI synthesis via rapid polymerization method	58
3.2.3	TEM images (a & b) and (c) average particle size histogram of PANI	59
3.2.4	XRD diffractogram of PANI	60
3.2.5	FT-IR spectra of PANI	61
3.2.6	(a) Gas adsorption-desorption isotherm curve and (b) Pore size distribution curve of PANI	62
3.2.7	UV-Vis spectra of PANI	63
4.1	Photographs of (a) metal stand and (b) brass collecting plate	76
4.2	Graphical illustration of OLCs synthesis via flame pyrolysis method	76
4.3	XRD profile of OLCs synthesized from candlesticks	78
4.4	TEM micrograph, (a) NPs, (b) Multi layers, (c) Chain-like connection and (d) particle size distribution of OLCs	79
4.5	SEM micrographs of OLCs	79
4.6	(a) Gas adsorption-desorption isotherm curve and (b) Pore size distribution curve of OLCs	80
4.7	FTIR spectrum of OLCs	81
4.8	Raman spectrum of OLCs	82
4.9	Thermographic profile (a) and (b) first order derivative weight loss curve of OLCs	82
5.1	Graphical illustration synthesis of In_2O_3/PANI/OLCs	89
5.2	Graphical illustration of the preparation of In_2O_3/PANI/OLCs sensing electrode	90
5.3	TEM micrographs of In_2O_3/PANI/OLCs composites, (a) B-IPC_1, (b) B-IPC_2, (c) Y-IPC, (d) B-IPC_3 and (e) B-IPC_4	91
5.4	SEM micrographs of In_2O_3/PANI/OLCs composites, (a) B-IPC_1, (b) B-IPC_2, (c) Y-IPC, (d) B-IPC3 and (e) B-IPC_4	92

5.5	X-ray diffractogram of In_2O_3/PANI/OLCs nanocomposites	93
5.6	Gas adsorption-desorption isotherm curves of (a) B-IPC$_1$, (b) B-IPC$_2$, (c) Y-IPC, (d) B-IPC$_3$, (e) B-IPC$_4$ and (f) Pore size distribution curves of all composites.	94
5.7	FT-IR spectra of In_2O_3/PANI/OLCs nanocomposites	96
5.8	Schematic depiction of (a) sensing mechanism and (b) bandgap structure diagram of In_2O_3/PANI/OLCs nanocomposites	97
5.9	Image of gas sensing equipment used in this study	98
5.10	(a) Dynamic response–recovery curves of In_2O_3/PANI/OLCs and (b) response of all nanocomposite constituents	99
5.11	(a) Dynamic response-recovery curve, (b) response-recovery time plot, and (c) reproducibility curves for B-IPC$_4$ sensor	100
5.12	The selectivity of B-IPC$_4$ tested at 100 ppm towards NH_3, C_3H_8O, C_6H_{14} and CH_3COCH_3	101
5.13	(a) Dynamic response–recovery curves and (b) response–concentration fitting curves, (c) reproducibility curves, (d &e) response-recovery plots of Y-In_2O_3 and B-In_2O_3 sensor.	102
5.14	Dynamic response–recovery curves of bare PANI,OLCs and PANI/OLCs	106

List of Tables

3.1.1	Average particle size of In_2O_3 prepared from dehydration of indium hydroxide	43
3.1.2	FTIR assignment bands of (a) In $(OH)_3$ and (b) In_2O_3 prepared from dehydration of indium hydroxide	44
3.1.3	Particle sizes of Y-In_2O_3 and B-In_2O_3, calculated using Scherer equation	49
3.1.4	BET surface area, pore size and pore volume distribution of Y-In_2O_3 and B-In_2O_3	52
3.2.1	Assignments of main FTIR bands of PANI	61
3.2.2	BET surface area, pore size and pore volume distribution of PANI	62
3.2.3	Uv-Vis absorption peak positions	63
4.1	BET surface area, pore size and pore volume distribution of OLC	81
4.2	Assignments FTIR bands of OLCs	82
5.1	Variation of Y-In_2O_3 and B-In_2O_3 loadings on the composites	90
5.2	BET surface area, pore size and pore volume distribution of In_2O_3/PANI/OLCs composite	95
5.3	FTIR assignments bands of In_2O_3/PANI/OLCs	96

Abbreviations

Abbreviations	Terminology
PANI	Polyaniline
APS	Ammonium persulfate
HMT	Hexamethylenetetramine
MW	Microwave
MOS	Metal oxide semiconductor
TEM	Transmission electron microscopy
SEM	Scanning electron microscopy
XRD	X-ray diffraction
EDS	Energy dispersive X-ray spectroscopy
FTIR	Fourier transformed infrared spectroscopy
VOCs	Volatile organic compounds
BET	Brunauer-Emmett-Teller
XPS	X-ray photoelectron spectroscopy
IDEs	Interdigitated electrodes
Nm	Nanometres
DMF	N, N Dimethylformamide
Ppm	Parts per million
OLCs	Onion-like carbons
HCSA	camphor sulphonic acid
p-TSA	p-toluene sulfonic acid
DBSA	Dodecyl benzene sulfonic acid
CP	Conducting polymer

HCl	Hydrochloric acid
H_2SO_4	Sulphuric acid
H_3PO_4	Phosphoric acid

CHAPTER 1

INTRODUCTION

1. Introduction

1.1.1 A concise summary of the study

As a result of expanding industrialization and urbanization, the globe is facing severe air pollution, as shown by the increasing massive volumes of hazardous and poisonous gases being released into the atmosphere, these pollutants include toxic fumes like CO, SO_2, NO_2, H_2S, NH_3, and volatile organic compounds (VOCs) including benzene, toluene, ethanol, acetaldehyde, and formaldehyde, to mention a few. For example, an estimated 3.8 million individuals each year suffer from serious diseases that can be deadly and are caused by air pollution [1]. Furthermore, home pollution is responsible for about 20% of cardiovascular fatalities and 20% of stroke deaths [1]. Poisonous gases can harm the respiratory tract and may even be detrimental to the neurological and immunological systems [1, 2].

Extreme air pollution, in particular, can cause changes in lung surfactant composition and lung damage, leaving individuals more prone to illnesses like COVID-19 [3]. As a result, air pollution has emerged as a major worldwide issue, causing numerous health organizations to establish short-term exposure limits (STELs) for different hazardous and VOC gases [4, 5]. Furthermore, to limit the possible harm to human health, pollutant gases in the air must be continually monitored using sensitive and dependable electronic instruments. Hazardous gas monitoring is becoming increasingly essential in several industries such as mining, outdoor and indoor air quality monitoring, and public safety, among others. Optic, auditory, gas chromatography, chemilluminescence ion chromatography, and spectrophotometry are all methods for detecting toxic gases. [6]. However, the technologies outlined are inefficient, difficult, and unsuitable for extensive, continuous gas monitoring.

Gas detectors, also known as gas sensors, are electrical devices that detect and identify different gases and converts chemical data to a useful analytical signal in a systematic manner [7]. A gas sensor typically consists of two functions: the receptor function, which identifies or recognizes a chemical substance, and the transducer function, which converts the chemical signal to the

sensor's output signal [8]. An ideal gas sensor requires high receptivity, high selectivity, quick response/retrieval, high stability/repetitiveness, room temperature operation, cheap cost and convenient manufacturing [9].

In 1952, Brattain and Bardeen demonstrated that certain semiconductor materials vary their resistivity depending on their surroundings, which led to the first use of metal oxides as chemiresistive gas sensors [10]. Metal oxides (MOx) such as TiO_2, WO_3, SnO_2, ZnO, In_2O_3, just to mention a few, have been frequently utilized as gas sensors because of their structural stability, low cost, and ease of integration. MOx as gas sensors has several drawbacks, which include a lack of selectivity and flexibility, and the need for high working temperatures (over 200 degrees Celsius) [9, 10, &11]. High working temperatures can result in massive power consumption, safety risks, and short shelf life. Considerable attempts have been made to develop gas sensors that function at normal temperature to overcome the challenges that metal oxide-based gas sensors have displayed to address this, carbon nanomaterials (e.g. carbon nanotubes, carbon dots, carbon nano onions, etc.), and conducting polymers (CP) (e.g. poly (p-phenylene vinylene), polypyrrole, polyaniline, etc.) are commonly used to produce superior sensing features such as increased sensitivity and room temperature operation. [12 &13].

Conducting polymers, due to their outstanding electrochemical and electrical characteristics, the low-cost advantages and lengthy stability and ease of production, are highly considered for efficient gas sensing technology [14]. The performance limitations such as limited sensitivity, sluggish response and recovery, poor thermal stability and selectivity also restrict the use of CPs as sensing layers [15]. Interestingly, scientists proved that nanocomposites of polymers/metal oxides may not only minimize polymer flaws or metal oxide flaws but they can also increase sensitivity, heat stability and reaction rate efficiently. The charge transfer mechanism is used to enhance sensing between MOx and CP, with CP replacing the inorganic components of MOx [16, 17].

Carbon nanomaterials provide a plethora of options for improving gas sensing properties due to their distinct electrical, catalytic, mechanical, and optical capabilities, making them promising candidates for the evolution of a new generation of low-power consumption, downsized, and wearable sensors [18]. This could potentially lead to the development of room-temperature operated gas sensors capable of detecting traces of various air pollutants [19].

Metal oxide nanomaterials have been synthesized utilizing a variety of methods, including vapour phase deposition, sol-gel, and microwave aided hydrothermal synthesis, and chemical vapour deposition [20]. Microwave synthesis has gained popularity in the synthesis of nanomaterials; it has an advantage over traditional methods due to the short reaction times caused by the combination of electrical and magnetic forces present in microwave radiation, which causes abrasion and collision of particles within the material [21-23]. Another benefit of microwave synthesis is that the material is heated uniformly, resulting in consistent nucleation and rapid crystal formation, resulting in a limited size product dispersion [23].

The most often utilized synthesis methods for CPs are rapid mixing polymerization, electrochemical technique, interfacial polymerization, and soft/hard template conducting polymers. Some of these techniques, however, have apparent disadvantages, such as post-treatment for template removal, time-consuming parameter settings, limited manufacturing yield, poor control of morphology/size homogeneity, and generally entail severe conditions [24-26]. As a result, the rapid mixing method has received increasing attention due to its environmental friendliness, use of common solvents such as water, large-scale manufacturing, and ability to provide control over their sizes, morphologies, and forms [27].

The chemical vapour deposition method and flame pyrolysis method, are two extensively used techniques for carbon synthesis nanomaterials (especially carbon nano-onions) [28]. Flame pyrolysis is preferred since it does not require the use of a catalyst, it uses flammable hydrocarbons as carbon sources to create carbon materials in the gram scale (e.g., wood fibre, diesel, lycopene (from tomato), and petrol (gasoline) [29-30].

A ternary nanocomposite containing various amounts of indium oxide, fixed amounts of polyaniline, and carbon nano-onions were prepared and employed as gas sensing layers for the detection of ammonia and a few volatile organic chemicals in this work. When compared to sensors that simply use metal oxides, the working capacity of the sensors should be enhanced. Furthermore, the efficacy of the products as sensing layers was examined using an alcohol enhanced reduction approach for indium oxide production and a conventional process that generally requires annealing.

1.2 Aim of research

The goal of this research was to synthesize a ternary nanocomposite consisting of polyaniline, indium oxide, and carbon nano-onions that can detect ammonia and a few other volatile organic compounds at normal temperatures.

1.3 Objectives of the research

- To prepare polyaniline nanostructures utilizing the rapid polymerization technique.
- To synthesize indium oxide nanoparticles using a microwave-assisted hydrothermal technique, with a special focus on the ethanol enhanced reduction method of synthesis.
- To make carbon nano-onions using the flame pyrolysis process.
- To create ternary nanocomposites of polyaniline, indium oxide, and carbon nano-onions, for room temperature gas detection application.
- To characterize the synthesized materials using various techniques, which include XRD (X-ray diffraction), UV-Vis (Ultra Violet-visible spectroscopy), TEM (transmission electron microscope), EDS (energy dispersive X-ray), SEM (scanning Electron microscopy) FTIR (Fourier transform infrared spectroscopy), and BET (Brunauer-Emmett-Teller).

1.4 Dissertation outline

Chapter 1: provides a synopsis of the research and its justification. It also describes the goals and objectives of the study.

Chapter 2: A comprehensive overview of relevant literature on Indium oxide, polyaniline, onions like carbon and their ternary nanocomposite applications for room-temperature gas detection.

Chapter 3: focuses on the microwave-irradiation procedure for the preparation and characterisation of indium oxide from different solvents (water and ethanol). The characteristics of indium oxide produced in various solvents are compared in this section and it also concentrates on the fabrication and applications of polyaniline by the rapid polymerization technique.

Chapter 4: Describes the synthesis and characterization of onions like carbon through flame pyrolysis method.

Chapter 5: focuses on the fabrication of a gas sensor for room temperature gas detection as well as the synthesis of ternary nanocomposite comprised of variable amounts of In_2O_3 and fixed amounts of PANI and OLC.

Chapter 6: Provides broad conclusions and future suggestions based on the findings concerning the study's goals and objectives.

1.5 References

[1] Andersen, Z.J et al. (2011).Chronic obstructive pulmonary disease and long-term exposure to traffic-related air pollution. American journal of respiratory and critical care medicine. 183(4), pp. 455-461. doi: 10.1164/rccm.201006-0937OC

[2] Annenberg, S.C., Horowitz, L.W., Tong, D.Q., & West, J.J. (2020).An estimate of the global burden of anthropogenic modelling. Environmental health perspective, 118(9), pp. 1189-1195.

[3] W. H. organisation, "Ambient air pollution: a global assessment of exposure and burden of disease." WHO, 2016.

[4] Woodruff, T. J., Axelrad, D. A., Caldwell, J., Morello-Frosch, R., & Rosenbaum, A. (1998). Public Health Implications of 1990 Air Toxics Concentrations across the United States. Environmental Health Perspectives, 106(5), pp.245–251. https://doi.org/10.2307/3434011 (Accessed August 2021)

[5] Doroftei, C., & Leontie, L. (2018). Nanostructured Oxide Semiconductor Compounds with Possible Applications for Gas Sensors. In M. R. Pagnola, J. U. Vivero, & A. G. Marrugo (Eds.), New Uses of Micro and Nanomaterials. IntechOpen. https://doi.org/10.5772/intechopen.79079 (Accessed July 2021)

[6] Li, G., Sun, S., Wilson, R. J., White, R. L., Pourmand, N., & Wang, S. X. (2006). Spin valve sensors for ultrasensitive detection of superparamagnetic nanoparticles for biological applications. Sensors and actuators. A, Physical, 126(1), 98–106. https://doi.org/10.1016/j.sna.2005.10.001

[7] Liu,F.S., Moh,C.H., & Timothy, M.(2015) .Single-walled carbon nanotube-Metalloporphyrin chemistry gas sensor arrays for volatile organic compounds,Chemistry of materials. 27(10), pp. 3560-3563.

[8] Zhang J et al. (2017).Metal-oxide semiconductor based gas sensor: screening preparation and integration. Chemical physics.19 (9), pp. 6313.

[9] Sunil, T.T., Chaudhuri, S., & Mishra, V. (2015). Optimal selection of SAW sensors for E-Nose applications. Sensors and actuators B: Chemical, 219, pp. 238-244.

[10] Manzoli A et al. (2012).Layer-by-layer fabrication of AgCl–PANI hybrid nanocomposite films for electronic tongues.55 (7), pp. 1866-1874.

[11] Nylabder, C., M. Armgrath, M., & Lundstrom,I.(1983). An Ammonia Detector Based on a Conducting Polymer. Proceedings of the International Meeting on Chemical Sensors, Fukuoka, 19(22), pp. 203-207.

[12] Timmer B.H et al. (2005).Ammonia sensors and their applications. Sensors and actuators B: Chemical. 107(2), pp. 666-677.

[13] Nicolas-Debarnot, D., & Poncin-Epaillard, F. (2003). Polyaniline as a new sensitive layer for gas sensors.Analytical chemical actuators.475 (1-2), pp. 1-15.

[14] Ibanez G.J et al. (2018) .Conducting polymers in the fields of energy, environmental remediation, and chemical-chiral sensors.Chemical reviews, 118(9), pp. 4731-4816.

[15] He L et al. (2013).Core-shell noble-metal@metal-organic-framework nanoparticles with highly selective sensing property, 52(13), pp. 3741-3745.

[16] Nalwa, H.S. (1997). Handbook of organic conductive molecules and polymers. 4, p. 728, 1997.

[17] Huang, J., Virji, S., Weiller,B.H., & Richard, B. (2003).Polyaniline nanofibers: Facile synthesis and chemical sensors. American chemical society, 125(2), pp. 314-315.

[18] Namsheer, K., & Rout, C, S. (2021).Synthesis and characterization of thin films of conducting polymers for gas sensing applications, pp. 5659-5697.

[19] Matsuguchi,M, et al. (2021).Highly sensitive ammonia gas sensors using micrometre-sized core-shell-type spherical polyaniline particles, MPDI Journals.21(22), pp.7522.

[20] Walter, C. (2000).Nanocomposite of polymers and metals or semiconductors: Historical background and optical properties Macromol. Rapid communications, 21(11), pp. 705-722.

[21] Jiang, H., Moon, K.S., Zhang, Z. et al. (2006). Variable Frequency Microwave Synthesis of Silver Nanoparticles. J Nanopart Res .8, 117–124. https://doi.org/10.1007/s11051-005-7522-6 (Accessed June 2021)

[22] Slocombe, D.R., & A. Porch, A. (2021).Microwaves in Chemistry. IEEE Journal of Microwaves.1 (1), pp. 32-42. doi: 10.1109/JMW.2020.3029337.(Accessed June 2021)

[23] Aggarwal et al. (2019).Surface-passivated, soluble and non-toxic graphene nano-sheets for the selective sensing of toxic Cr (VI) and Hg (II) metal ions and as a blue fluorescent ink. Nanoscale Advances.11, pp.192.

[24] Mohapatra, D et al. (2016). Facile wick-and-oil flame synthesis of high-quality hydrophilic onion-like carbon nanoparticles. Materials chemistry and physics.174, pp. 112-119.

[25] Ghosh, M. (2011). Carbon nano-onions for imaging the life cycle of drosophila melanogaster. 7(22), pp. 3170-3177.

[26] Miriyla N et al. (2020). Synthesis of carbon onion and its application as a porous carrier for amorphous drug delivery.Crystals.10 (4), pp.144-146.

[27] Elhaes, H., Fakhry, A., & Medhat Ibrahim. (2016).Carbon nanomaterials as gas sensors. Materials today: proceedings.3 (6), pp 2483-2492. https://doi.org/10.1016/j.matpr.2016.04.166. (Accessed June 2021).

[28] Salahuddin B et al. (2021).Carbonaceous materials coated carbon fibre reinforced polymer matrix composites.Polymers.13 (16), pp. 2771.

[29] Ewels, C.P. (2005).Nitrogen doping in carbon nanotubes. Nanoscience and Nanotechnology, 5(9), pp. 1345-1336.

CHAPTER 2

LITERATURE REVIEW

2.1 Introduction (Overview)

2.1.1 What are nanomaterials?

Nanomaterials are described as materials with at least one dimension of fewer than 100 nanometres. One millionth of a millimetre, or ten thousand times less than the diameter of a human hair, is a nanometre. Nanomaterials are intriguing because of their remarkable optical, magnetic, electrical, and other characteristics develop at the nanoscale. These characteristics have the potential to make a significant effect in electronics, medicine, and other disciplines [1].

2.1.2 The Dimensional Classification of Nanomaterials

Nanomaterials are available in a variety of sizes, including zero, one, two, and composites (Figure 2.1). They come in spherical, tubular, and irregular shapes and can be solitary, fused, aggregated, or agglomerated. Nanotubes, dendrimers, quantum dots, and fullerenes are examples of common nanomaterials. [2].

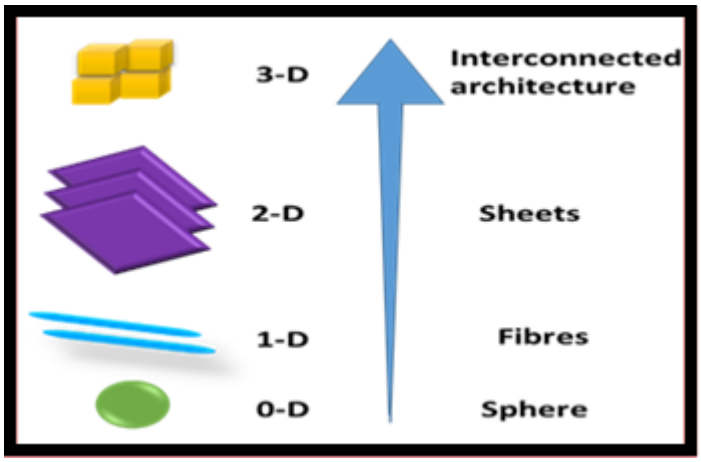


Figure 2.1 Dimensions of nanomaterials

As shown in the diagram above, various modulation dimensions can be used to create nanomaterials: zero (atomic clusters, filaments, and cluster assemblies), one (multilayers), two (ultrafine-grained over layers or buried layers), and three (ultrafine-grained over layers or buried layers) (Nanophase materials consisting of equiaxed nanometre-sized grains) [3].

2.1.3 Synthesis of nanomaterials

Nanomaterials can be synthesized via two major methods (Figure 2.2); the top-down strategy (in which large materials are segmented) and the bottom-up approach (small molecules or atoms are mixed to create nanomaterials) [4]. These approaches encompass a variety of synthesis processes and fall into four distinct categories: chemical, physical, mechanical, and biological. Typical top-down techniques include high-energy ball milling, severe deformations, etching, dynamic alloys, lithography, dynamic milling, and micromachining. Bottom–up synthesis techniques include sol–gel, chemical, spinning, and CVD [5]. Nanomaterials have unique physicochemical features that have garnered considerable attention in a variety of applications, of which few are discussed below:

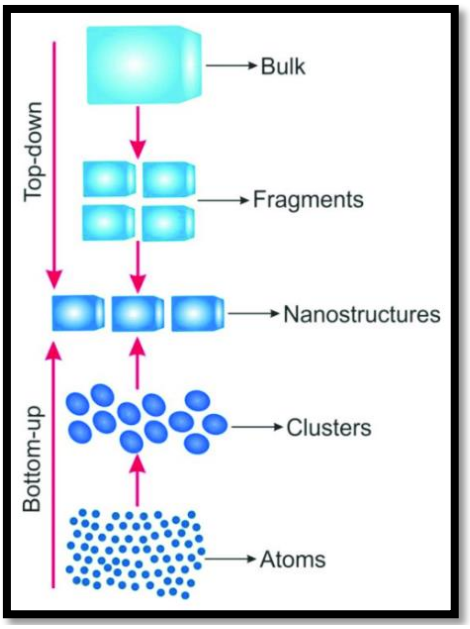


Figure 2.2 Synthesis of nanomaterials [6]

i. Catalysis

Catalysis is the pioneering use of nanoparticles. For many years, several elements and materials such as aluminium, iron, titanium dioxide, clays, and silica have been employed as nanoscale catalysts. Nano catalysis has risen to prominence in recent years as a result of its increased

activity, selectivity, and efficiency. Small metal nanoparticles with sizes ranging from 1 to 10 nm demonstrate exceptional catalytic activity, sometimes outperforming the equivalent metal complexes. The high activity of Nano catalysis is related to several critical variables, including a high specific surface area ratio, surface geometrical effect, electronic effect, and quantum size impact [7].

ii. Water treatment

The use of nanomaterials in treating wastewater has received a lot of interest lately. Nanomaterials have high adsorption capabilities and reactivity due to their tiny sizes and hence huge specific surface areas. Heavy metals [8], organic contaminants [9], inorganic anions [10], and microorganisms [11] have all been effectively eliminated from waste water by different nanomaterials [12].

iii. Sensors

The creation of a diverse range of nanomaterials has prepared the path for their use in the construction of high-performance electrochemical sensing devices. The use of nanomaterials in gas sensing has many advantages, including high surface-to-volume ratios, high adsorptive power, and high reactive capacity. Their broad surface areas improve catalytic and sensing responsiveness by enabling analyte molecules to pass quickly through the material [13]. Furthermore, by minimizing dynamic range and/or confining structures in a certain crystallographic direction, the physical, catalytic, and electrical properties of nanomaterials can be easily tuned [14].

2.2 Gas Sensor

Gas sensors detect the presence and quantity of a variety of toxic gases and vapours, including poisonous or explosive gases, volatile organic compounds (VOCs), humidity, and odours [15].

2.2.1 Characteristics of gas sensors

Sensitivity (S) is frequently stated as Ra/Rg for reducing gases and Rg/Ra for oxidizing gases, wherein Ra refers to the resistance of gas sensors in the standard gas (usually air) and Rg refers to the resistance of gas sensors in the test gas [16]. Selectivity is described as a sensor's capacity to distinguish or precisely respond to a certain gas among a variety of other gases. Selectivity

is generated by the slope of S (%) versus gas concentration (Cg). The responsiveness of a sensor is defined as the time required to achieve 90% of its entire response, such as resistance, after being exposed to the target gas is known as response time [17]. Recovery time is defined as the time required for a sensor to return to 90% of the original baseline signal upon removal of the target gas [18]. Reversibility is described as a sensor's output signal's capacity to recover to its initial baseline following gas cut-off. Repeatability is a measurement of the similarity of two or more sensor batches or the ability of a sensor to consistently provide the same output signal for the same gas concentration [19; 20]**.**

2.2.2 Chemiresistive gas sensor

Chemiresistors are conductive materials having an intrinsic resistance or conductance that may alter in reaction to changes in the surrounding environment's chemical properties [20]. The principle of chemiresistive type sensors is controlled by changes in the sensing entity's resistance value in a chemical environment [21]. Tuning of the sensing elements' resistance is dependent on the structure and type of the target gas employed. In chemiresistive gas sensors, metal oxides, conducting polymers, and carbon-based materials have been utilized as sensing layer materials. Metal oxide compounds and their geometric models have been widely researched as sensing layers over the last few decades [22; 23].

In_2O_3, ZnO, MoO_3, ZrO_2, Fe_2O_3, as well as several others, because of their tuneable transport properties, have been utilized as sensing elements in chemiresistive sensors. Micro-heaters are commonly used in combination with these sensing elements to enhance the sensing response [24]. The elevated operational temperatures of these sensors results in reduced dependability over time. One of the difficulties in establishing the reliability of sensors in the nanoscale regime is the development of inner grains of sensing elements at elevated operating temperatures [25]. To maximize one's potential, including lengthy reliability, it is critical to design a room temperature controlled gas sensor by employing nanostructured materials to reduce working temperatures; for less power consumption and safer operation [26].

2.2.3 Gas sensing mechanism

Gas-sensing responses are acquired by measuring the time-dependent variation in the film’s resistivity as a consequence of the target gas concentration. When exposed to reducing/oxidizing gas, the film resistance value changes and eventually returns to its original condition when

the desired gas flow is ceased. The gas sensing response is a result of both simple diffusion of test gas molecules onto the sensing films and the electron capture/donation procedure of the polymer matrices engrained with inorganic nanoparticles, which is assisted by intersection effects at the conducting polymer-inorganic/organic integrations [27].

Depending on the nature of the organic or inorganic nanoparticles implanted in the conducting polymer matrix, a Schottky heterojunction (P-N) is produced at the boundaries of the conducting polymers and nanoparticle interface [28]. The interaction of the targeted gas molecules with the nanocomposite film surface causes the polymers to lose or gain electrons, resulting in a change in the breadth of the depletion zone, which might limit or broaden the polymers' conductive route.

Due to the low content of metal oxide nanostructures in conducting polymers, typically between 0.1 and 10 % by mass, the resistivity of nanocomposite films is mostly governed by the carbon material/conducting polymer composition. The increased sensitivity of the nanocomposite films towards the target analyte is due to the synergistic effects of the altered conductivity and conductive routes of the polymers in the nanocomposite films [28; 29].

The adsorption and desorption of interfacial oxygen species is widely acknowledged as the mechanism by which n-type semiconductor metal oxides such as Fe_2O_3, MnO_2, ZnO, SnO_2, and In_2O_3 sense gases. The oxygen molecules in the air absorb charge carriers when they adsorb on the surface of n-type semiconductor metal oxides, forming chemisorbed oxygen species (O_2^-, O_2^{-2}, and O^{-2}) as a result of the charge capture, a depletion zone forms on the surface of the semiconductor metal oxide [30].

When analyte vapour molecules interact with surface oxygen species, induced sorption from the surface occurs, allowing captured electrons to be injected back into n-type semiconductor metal oxides and decreasing the resistance of the n-type of semiconductors. The supply of oxygen placed on the surface of the semiconductor metal oxide also has an effect on response characteristics; a substantial amount of oxygen adsorbed on the surface allows for further surface reactions [31].In general, the behaviour of p-type conductance is caused by the covering of the sensing materials' surfaces with oxygen chemisorbed from the environment. Adsorbing oxygen molecules absorb electrons and ionize them, resulting in the formation of a hole accumulation layer [31; 32]. When detecting materials are subjected to a reducing gas (e.g. NH_3), the analyte gas reacts with the surface oxygen species on the basis of transfer of electrons from

the reacting analyte vapour to the detecting materials [32-34]. The electrons introduced into the sensing materials recombine with the vacancies, resulting in a decrease in charge carrier concentration and an increase in sensing material resistivity.

During sensing, it is common to see that n-type sensing materials behave similarly to p-type sensing materials and conversely. Temperature or concentration variations can both encourage such changes. At high temperatures, n-type sensing materials converts to p-type, according to Hao et al. [35]. The reason for this is that the adsorbed oxygen species are O_2 species at low temperatures. However, O_2^- and O^{-2} species coexist at high temperatures, and these oxygen species can grab more electrons than those at low temperatures [36; 37].

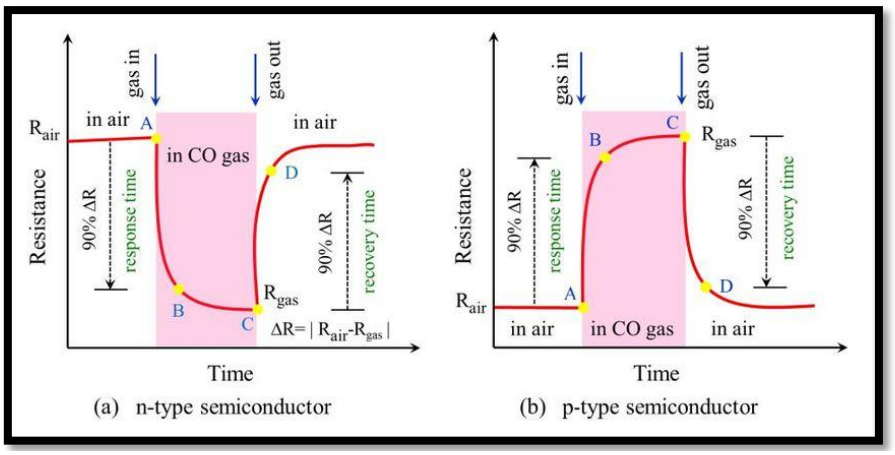


Figure 2.3 Graphical illustration of P and N, type sensing behavior [37]

Xue et al reported sensing based on temperature behaviour of Pt@SnO_2 nanoribbon as the sensing material [38]. They discovered anomalous p-type conductivity at low temperatures. Nonetheless, at a temperature of 300 degrees Celsius, the anticipated n-type conductivity was found; nevertheless, this unexpected p-type behaviour was elucidated [38; 39]. As a result, not only did a change in temperature create an unusual finding, but so did a change in analyte vapour concentration. According to Siciliano et al. [39], the conductivity of sensing materials changes from n-type at low concentrations to p-type at high concentrations depending on the concentration of the analyte. In general, the sensing process entails complete oxidation to carbon dioxide and water. The following are the hypothesized reactions of oxygen molecules with ethanol.

$$O_2\,(gas) \rightarrow O_2\,(ads) \quad (1)$$

$$O_2\,(gas) + e^- \rightarrow O_2^-\,(ads) \quad (2)$$

$$O_2^-\,(ads) + e^- \rightarrow 2O^-\,(ads) \quad (3)$$

$$C_2H_5OH + 6O^- \rightarrow 2CO_2 + 3H_2O + 6e^- \quad (4)$$

2.2.4 Metal oxides as gas sensors

The ability to manage the physiochemical properties of metal oxides (MOx) is the foundation of modern intellectual and functional materials and technologies. Many chemical and structural factors influence the functional qualities of MOx; chemical composition, structural defects, shape, size distribution, and surface area, to name a few. In terms of physics and materials science, MOx is the most diverse family of materials. It has features that cover almost every area of physics and materials science in the fields of semiconductivity, superconductivity, ferroelectricity, and magnetism [40]

The modification of any of these features enables control of their attributes. Sensing materials for semiconductor gas sensors include SnO_2, ZnO, In_2O_3, tungsten trioxide (WO_3), CdO, TiO_2, and various MOx [41]. They are classed as translucent conductive oxides due to a unique collection of functional properties, the most notable of which include electrical conductivity, opacity over a broad range of spectral ranges, and a high degree of surface reactivity. Nonetheless, challenges with using metal oxides as gas sensors are the lack of selectivity, flexibility and use of high operating temperatures (more than 200℃). High operating temperatures may lead to enormous power consumption, safety hazards and compact shelf life [41-43].

2.2.5 Indium oxide

In_2O_3 (Indium oxide) is an n-type semiconductor with a direct band gap of 3.5–3.7 eV and an interband gap of 2.6 eV [44]. It is complicated cubic bixbyite architecture is produced from an arrangement of empty tetragonal oxygen anion positions. The n-type semiconducting characteristic of In_2O_3 is owing to stoichiometric composition variations, and extra indium atoms or

oxygen vacancies can act as donors. In_2O_3 can exist in three distinct phases, which are distinguished by space group symmetries $I2_13$, $R3$, and $Ia3$ (crystal structures figure 2.4); $I2_13$ and $R3$ are rarely studied [45]. The cubic lattice of In_2O_3 has the $Ia3$ space group; the unit cell contains 16 formula units and 80 atoms [46]. The crystal's atoms create a layer structure comprising layers that alternate of indium and oxygen atoms. Each unit cell is made up of four layers of oxygen atoms and four layers of indium atoms [47].

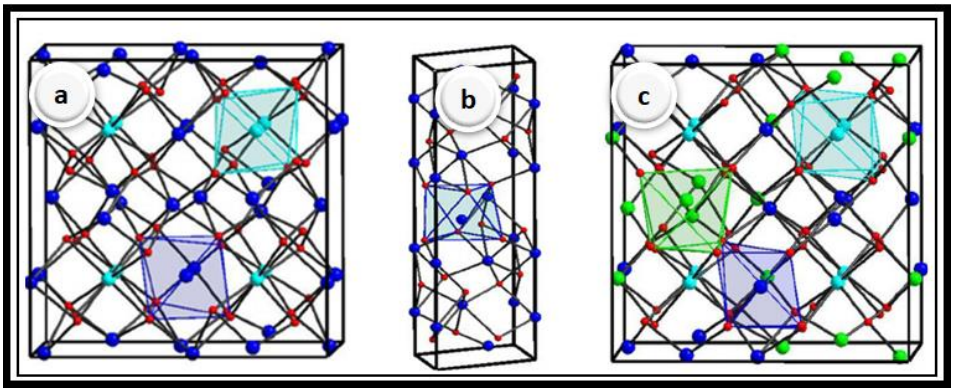


Figure 2.4 Crystal structure of (a) $I2_13$, (b) Ia3 and R3

Indium oxide-based materials are currently being used in electro-optic modulators, such as window heating systems, solar panels, electrochromic lenses and flat-panel displays in the electronic industry. In contrast, indium oxide-based nanostructures are appealing device materials for chemical sensors and building blocks for future Nanoelectronics [48]. Metal oxide nanoparticles' possible technological uses have piqued the curiosity of scientists in material science, health, agribusiness, computer technology, biomedical, photonic, gas sensing, catalysis, climate, and energy [49; 50]. Several synthetic techniques have been established for synthesizing MOx nanomaterials methods include:

i. Sol-gel

A homogeneous solution of fine materials in a fluid solution is what this is. This gel is composed of a tiny solid molecule suspended in a liquid solution. Because of its simplicity, the sol-gel method, a wet procedure in which chemical regents are used as precursor molecules for nanoparticle synthesis, is commonly used for nanoparticle production. Heating, accompanied by stirring, shaking, or sonication, disperses these metal oxides and chlorides

in liquid medium [51]. The resulting mixture contains both solid and liquid phases. Separation of the nanoparticles is accomplished using a variety of techniques, including centrifugation, filtration, and sedimentation [52].

ii. Chemical vapour deposition (CVD)

This method is based on the deposition of gaseous molecules on a solid substrate at an optimal temperature in a reaction compartment. When gaseous molecules come into touch with the heated substrate, the reaction begins [53]. This process offers numerous advantages, including the creation of extremely pure, hard, and uniform nanoparticles. The temperature has a considerable impact on the nanoparticle formation reaction. However, this method has some drawbacks, including the generation of poisonous gaseous by-products and the need for specialized equipment for the synthesis process [54].

iii. Sputtering

This approach relies on collisions between ejecting materials and ions to deposit nanoparticles on the surface [55]. Nanoparticles are frequently deposited on a surface in the shape of a thin coating. The thickness of the deposited layer is determined by temperature, annealing time, and the materials employed in the synthesis, among other factors. The size and shape of nanoparticles are likewise determined by these characteristics [56].

iv. Hydrothermal/Solvothermal Process

The phrase "hydrothermal/Solvothermal process" refers to the process of executing chemical reactions in solvents confined in closed containers in which the temperature of the solvents can be raised to near critical degrees by heating with autogenous pressures at the same time [57]. When water is employed as the solvent, the process is referred to as "hydrothermal." In some circumstances, this phrase is also used to describe processes that take place under normal settings. When organics are utilized as solvents, the term "Solvothermal process" is used [58].

v. Thermal evaporation deposition

Thermal Evaporation is a typical method of PVD (Physical Vapour Deposition). Thin Film Coating is a sort of vacuum technique used to cover the surfaces of various objects with pure materials. Coatings, often known as films, are typically in the angstrom to micron thickness range and May be made with a single material or stacked comprising numerous components [59]. Thermal evaporation technologies can be used to transfer single atomic elements, which include metals and non - metals, and also compounds such as oxides and nitrides. The substrate is the object that will be coated, and it can be anything from semiconductor wafers to solar cells to optical components, among many other options [60]. Thermal evaporation is the process of burning a solid inside a high sealed container to a temperature that causes vapour pressure to develop. Even a very modest vapour pressure inside the vacuum chamber is sufficient to produce a vapour cloud. This evaporated substance now forms a vapour stream that travels through the chamber and adheres to the substrate as a coating or film [61].

2.4 Microwave synthesis techniques

2.4.1 Principle of microwave synthesis

The microwave part of the electromagnetic continuum has wavelengths ranging from 1cm to 1m (frequencies of 300GHz to 300MHz). Microwaves are most commonly used in point-to-point networking, satellite television broadcasting, and RADAR systems. Aside from that, they are used in commercial, pharmaceutical, chemical, and science research contexts. The microwave has gained widespread acceptance as a method for synthesizing different compounds (organic and inorganic) in research laboratories and industries [62]. Dr Percy Spencer established the heating property of microwaves in 1946 as a result of a contextual experiment of radar-oriented research. Microwave radiation has since ushered in a new age of science. The methodology is no longer restricted to the food industry but has had an impact in several other fields as well [63]. An electrical field exerts a force on charged particles and dipoles, causing microwave heating. When the substance receives microwave radiation, it undergoes rotational excitation, and the increased kinetic energy of the molecules is recorded as a temperature rise. Microwaves' heating effect is produced by two main mechanisms: dipole polarization and ionic

conduction, all of which are mediated by the electric field portion. Compact molecules, with irreversible dipole moments, deal with microwave radiation in the gaseous state [64].

The frequency of irradiation in the dipole polarization system is such that the molecular dipoles react by rotating in response to the alternating electric field. The molecules coordinate their dipoles with the surrounding field, and energy is lost because of molecular friction and spontaneous collisions, resulting in dielectric heating. The ionic conduction process involves the movement of ions as a result of an electric field's effect, with the kinetic energy emitted as heat as the collision rate increases [65]. In recent years, microwave radiation has become more commonly used in organic chemistry, citing reports of faster reaction times and cleaner, easier-to-prepare reactions than those produced by typical heating processes. In certain cases, higher yields have also been published [66].

2.4.2. Advantages of microwave heating over conventional thermal heating

Microwave irradiation has many benefits over traditional thermal heating of reactants. Traditional thermal heating typically requires the need for a furnace or oil bath to heat the reactor walls using convection or conduction. The sample's centre takes a lot longer to attain the target temperature, and as a result, the sample is not heated evenly. Heating the furnace or oil bath often absorbs enormous energy [67]. During microwave heating, there is no direct interaction between the energy source and the sample as a result of the introduction of microwave energy into the sample remotely. Microwave dielectric heating is similar to a flash heating process except that the energy is generated much faster and the sample cools much faster at the end of the reaction (Figure 2.5).

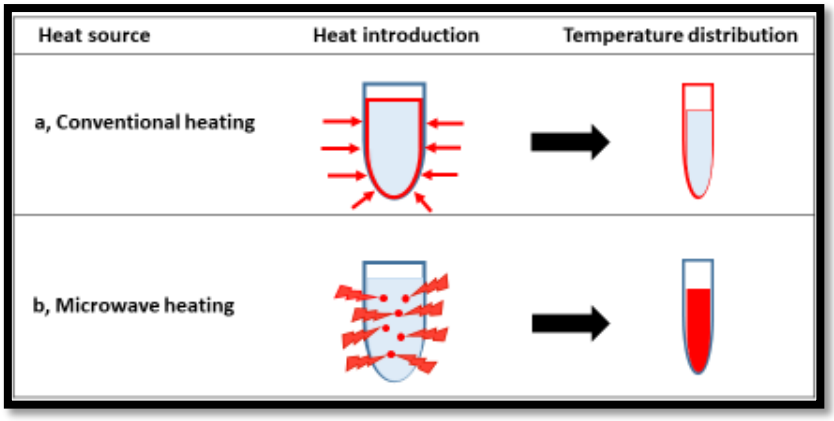


Figure 2.5 (a) Conventional heating vs. (b) Microwave heating [68]

As compared to traditional heating, this results in very different temperature-time profiles, which could lead to vastly different products [68]. Yields are often usually higher, and the process may be used to synthesize compounds that are not currently usable. The process can also be used to create materials with greater purity, finer particle sizes, narrower particle diameter distributions and improved physicochemical properties [69]. Furthermore, microwave methods are remarkable in that they can be scaled up without suffering from thermal gradient effects, resulting in a potentially industrially significant breakthrough in large-scale nanoparticle synthesis [70].

2.5 Conducting polymers

Conducting polymers, because their electrical conductivity can alter when exposed to oxidative or reductive gas molecules at ambient temperature, have seen fast development and have shown significant promise in chemical gas sensors for ambient temperature. [71; 72]. When they engage with gas particles, they either act as an electron donor or recipient, causing changes in carrier concentration and, as a consequence, a change in the electrical properties or resistance of the sensing polymers. Polyaniline (PANI), polypyrrole (PPy), polythiophene (PT), poly (3, 4-ethylene dioxythiophene) (PEDOT), Polyacetylene (PA), poly (phenylene vinylene) (PPV) (Figure 2.6), and their derivatives are among the conducting polymers identified as sensitive materials in the literature [73; 74].

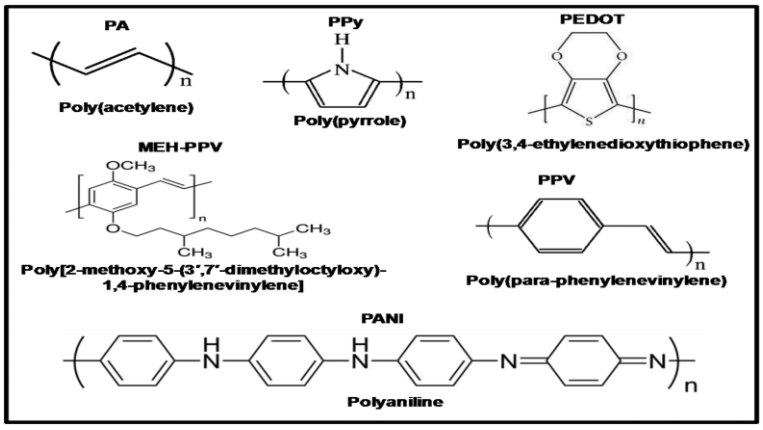


Figure 2.6 Structural illustration of conducting polymers [74]

Conjugated electron backbones in conducting polymers (CPs) such as polypyrrole, polythiophene, and polyaniline show peculiar low power optical shifts, low activation potentials, and strong electron affinities are examples of electronic characteristics. [75]. CPs are of critical relevance because they have unusual attractive mechanical qualities and manufacturing advantages of polymeric materials, these materials have optical and electrical properties that match metals or inorganic semiconductors., which are referred to as "synthetic metals." A range of benefits is included, including ease of preparation practices, morphology stability, structural durability, lightweight, and cost-effectiveness [76-78].

In past few decades, there has been significant scientific progress in conducting polymers-based room-temperature gas sensors. Nevertheless, because of their low conductivity and strong affinity for VOCs and water molecules, they always have poor sensitivity, low stability, and inadequate gas selectivity, this limits their usage in gas sensing applications. [79; 80]. Conducting polymers have been historically synthesized with acid or peroxide initiators, either by chemical or electrochemical oxidation routes, which result in isolation materials that involve post-doping processes [81]. Interfacial polymerization and rapid mixing procedures have recently been established as two new directed conducting polymer synthesis technologies. Two immiscible organic/aqueous liquids are used in the Interfacial polymerization technique, and polymerization occurs at the interface of two solutions.

The CP, as produced, immediately diffuses into the aqueous layer, preventing subsequent growth. However, the poor yield of CPs generated is the method's primary drawback. As a result, this approach is ineffective for the bulk manufacturing of CPs. The fast mixing technique, on the other hand, entails rapidly combining monomers with the oxidant in suitable proportions to produce vast numbers of CPs, with the diameter being dependent on the acid medium employed in the process [82].

2.5.1 Conducting Polymer Systems Requirements

Valence electrons are found in the outermost shell of electrons in a substance and can be grouped in the valence band, which determines their lowest energy states. An electron must gain enough energy to be promoted to the conduction band. It is widely accepted that an organic

polymer must have an overlapping collection of molecular orbitals to facilitate electronic conduction and allow for fair carrier mobility along the polymer chain [83]. Conducting polymers are usually polyconjugated materials that are insulators in their pure form, which may be converted into polymeric salts with conductivities comparable to metals when treated with an oxidizing or reducing agent [84].

The fundamental structural feature of all conjugated polymers is their semi-infinite π system, which spans a vast number of repeating monomer units. Because of this function, materials with directional conductivity are generated [85]. The expanded conjugated polymer structure is extremely sensitive to chemical or electrical oxidation or reduction. This modifies the electronic and optical properties of the polymer, and by carefully controlling the oxidation and reduction processes, it is able to precisely control the electrical and optical properties. [86].

Conjugated polymers are intrinsic semiconductors in their non-doped form, with the band difference determined not only by the chemical composition of the conjugated backbone but also by the configuration of the substituents connected to the main chain. Thus, by using sufficient functionalization, the optical and electronic properties of conjugated polymers can be greatly altered [87]. Conducting polymers have an expanded p-orbital system that allows electrons to move from one end to the other. The bonding in conjugated polymers results in one unpaired π-electron per carbon atom. Furthermore, π bonding causes electron delocalization on the polymer's backbone when the carbon orbitals are in the sp^2 P_z arrangement and the orbitals of consecutive carbon atoms in the backbone overlap [88].

2.5.2 Doping of organic polymers

Doping is the one-of-a-kind, fundamental, defining, and merge theme that separates Conducting polymers are distinguished from all other types of polymers. During the doping process, an organic polymer that is either an insulator or a semiconductor with a conductivity, typically between 10^{-10} and 10^{1} S/cm, is changed into a polymer with a ‘metallic' conductivity (1 to 10^{4} S/cm). Doping of organic polymers entails removing electrons from the valence band (p-doping) or adding electrons to the conduction band (n-doping, which is significantly less common). To dope organic polymers, electrons are removed from the valence band (p-doping) or added

to the conduction band (n-doping). Doping (either p or n) results in the formation of charge carriers that migrate in the presence of an electric field. Charges that are positive (holes) or negative (electrons) move to opposite electrodes. Electrical conductivity is determined by this charge mobility. [89]. The regulated addition of recognized, nonstoichiometric concentrations of chemical species (usually less than 10%) causes significant changes in the polymer's mechanical, magnetic, optical, electrical and structural properties. Doping may be reversed to return the polymer to its original state with minimal to no deterioration of the polymer backbone [90]. Chemical and electrochemical doping and dedoping procedures are both possible. Both include dopant counter-ions that maintain the doped state. [91]. by carefully managing the doping standard, a conductance between the undoped and wholly doped forms of the polymer may easily be obtained. This enables the optimal properties of each polymer type to be optimized. [92].

2.5.3 Polyaniline (PANI)

Polyaniline has received a lot of interest in recent years because of its propensity to display a significant degree of conductance. It has been discovered in several colour variations, some of which are not electrically conductive [93]. To comprehend the chemical characteristics of polyaniline, it is required to connect colour and conductance with structure in a way that is compatible with the conditions of preparation (oxidative polymerization of aniline) and the conditions of interaction between the various forms. (Figure 2.7) [94].The current state of knowledge regarding the nature of the numerous polyaniline species and their conversions may be summarized in a simple reaction mechanism, which will serve as a beneficial basis for future advancements in polyaniline chemistry. Protonated emeraldine, the most common type of polyaniline, is green and electrically conductive, and it is made via oxidative polymerization of aniline, which is usually in the form of hydrochloride. It may be transformed to protonated pernigraniline, which is blue and may be predicted to be conducting if harsher oxidizing conditions are used. Subsequent treatment with alkali leads to the pernigraniline base, which is violet and non-conducting [95].

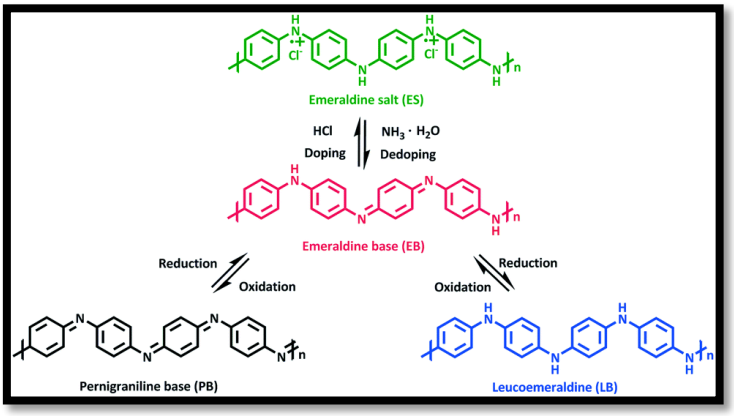


Figure 2.7 Structural illustration of forms of polyaniline [94]

2.6 Onion like-carbons

Carbonic nanomaterials like nano diamonds, carbon nanotubes, fullerenes, fluorescent carbon nanoparticles, graphene sheets, and or onion-like carbons (OLCs) have stimulated significant research due to their diverse technical applications (Figure 2.8). Among the electrical and physicochemical properties of OLCs, their optical characteristics, especially their fluorescence emission, have garnered recent attention. For several years, semiconductor quantum dots have been actively explored for their strong and adjustable fluorescence emission properties, which enable their usage in sensors and cell imaging. [96].

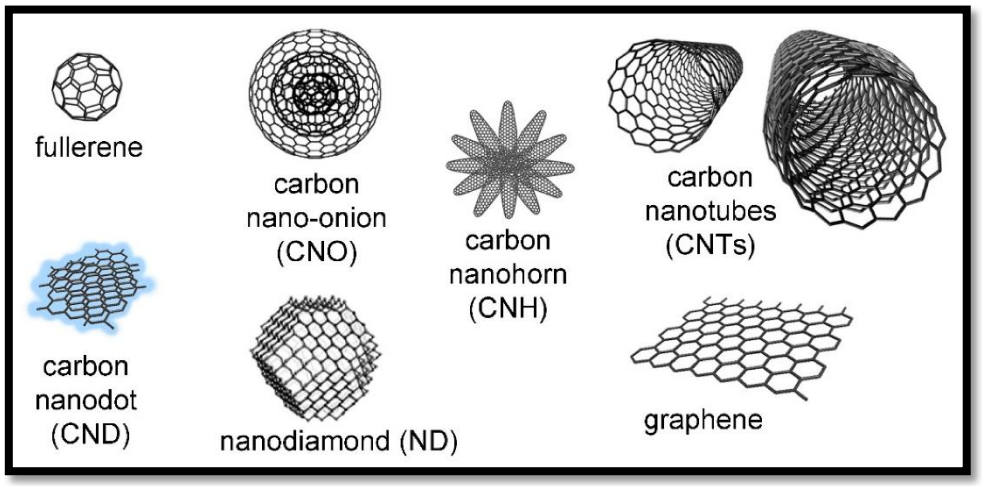


Figure 2.8 Schematic illustration of Carbon structures with various allotropes. [96]

Physical and chemical processes, including arc discharge [97], laser ablation [98], plasma method [99], chemical vapour deposition (CVD), and high-temperature annealing [100], have

been effectively used for the production of OLCs. OLCs have demonstrated enormous ability as adaptable nanomaterials for extensive variety of applications, including chemical sensing, bio-sensing, and bio-imaging, drug administration, photodynamic treatment, photo-catalysis, and electro-catalysis, as a category of newly discovered fluorescent nanomaterials [101]. OLCs' unique characteristics, such as their innocuous chemical composition, tuneable fluorescence emissions, ease of derivatization, and outstanding physicochemical and photochemical consistency (non-photo bleaching or non-photo blinking), make them very appealing for technical applications when compared to conventional semiconductor quantum dots [102].

2.7 Polymer nanocomposite-based sensor

MOX materials such as ZnO, MnO_2, α-$Fe_2O_3SnO_2$, and In_2O_3 have several advantages in sensors such as structural stability, ease of integration, cost-effectiveness, and capacity to sense the majority of hazardous gases, which have all contributed to the ongoing developments and widespread applications for the detection of chemical compounds [103]. However, MO_X is also constrained by a lack of flexibility and selectivity, as well as functioning at high temperatures (more than 200 °C), leading to significant power consumption, safety concerns, and limited lives. Thus, to increase the electrical conductivity and room temperature operation of MO_X, many ways have been discovered, encompass doping with conductors like as carbon nanoparticles, graphene, carbon nanotubes, and others, as well as polymers. [104].

OLCs exhibit a one-of-a-kind combination of mechanical, chemical, and physical features, these qualities, when combined with acceptable compatibility, can lead to the creation of composite materials [105]. The combination of OLCs and other compounds can result in fascinating materials with characteristics derived from the separate components. Combining OLCs with conducting polymers, in particular, produces novel materials [106] that are particularly appealing as electrode materials for electrochemical and medicinal applications.

Although pristine PANI-based sensors in various shapes have better sensor properties than bulk PANI, they have drawbacks such as limited repeatability, selectivity, and sensitivity. According to the literature [107], the inclusion of inorganic/organic NPs in the CP matrix can enhance the gas-sensing characteristics of the resultant hybrid nanocomposites. The characteristics may be changed primarily in two ways: first, n-type semiconducting materials (e.g., WO_3, TiO_2, SnO_2, and In_2O_3 etc.) can modify the p–n heterojunctions at the CP/oxide interfaces [108-110]. Polymer nanocomposite-based sensors based on polyaniline (PANI), carbon Nano-onions

(OLCs), and indium oxide (In_2O_3) nanoparticles were synthesized in this study to identify and comprehend the ammonia sensing mechanism and specific VOCs.

2.8 References

[1] Khan, I., Saeed. & Khan, I. (2019).Nanoparticles: Properties, applications and toxicities. Arabian Journal of chemistry.12 (7), pp. 908-931.

[2] Abouelmagd S.A et al. (2016) .Tannic Acid-Mediated Surface Functionalization of Polymeric Nanoparticles. ACS Biomaterials science & Engineering.2(12), pp. 2294-2303,

[3] Ali, A., Zafar, H., Zia, M., Haq, I., Phull, A.R., Joham Sarfraz Ali, J.S.,&Hussain A (2016).Synthesis, characterization, applications, and challenges of iron oxide nanoparticles," Nanotechnology, science and applications.6(9), pp. 49-67.

[4] Harrison,P., & Valavanis,A.(2005) .Quantum Wells, Wires and Dots: Theoretical and Computational Physics of Semiconductor Nanostructures. Chichester: John Wiley & sons.

[5] Murali, A.,Lokhande,G.,Deo,K.A., Brokesh,A.,Gaharwa,A.K.(2020).Emerging bio-applications of two-dimensional nanoheterostructure materials," 2D Nanoscale heterostrutures materials.6(8), pp. 243-255.

[6] GalstyanV et al. (2018).Metal oxide nanostructures in food applications: Quality and packaging," Chemo sensors.6 (2), pp. 16.

[7] Mohammadparast F et al. (2019). C-C Coupling reactions catalyzed by gold nanoparticles: Evidence for substrate-mediated leaching of surface atoms using localized surface Plasmon resonance spectroscopy. The journal of physical chemistry.123, pp. 11539-11545.

[8] Lu H et al. (2016) .An Overview of Nanomaterials for Water and Wastewater Treatment. Advances in materials science and engineering, 2016, pp. 10. https://doi.org/10.1155/2016/4964828 (Acessed May 2021)

[9] Yan, J., Han, L., Gao,W., Xue, S.,& Chen M.(2014).Biochar supported nanoscale zerovalent iron composite used as persulfate activator for removing trichloroethylene," Bioresource technology.175, pp. 269-274.

[10] Liu F et al. (2014).Graphene-supported nanoscale zero-valent iron: removal of phosphorus from aqueous solution and mechanistic study," Journal of environmental sciences.26 (6), pp. 1751-1762.

[11] Kalhapure, R. S., Sonawane, S. J., Sikwal, D. R., Jadhav, M., Rambharose, S., Mocktar, C., & Govender, T. (2015). Solid lipid nanoparticles of clotrimazole silver complex: An efficient nano antibacterial against Staphylococcus aureus and MRSA. Colloids and surfaces. B, Biointerfaces, 136, 651–658. https://doi.org/10.1016/j.colsurfb.2015.10.003 (Accessed May 2021)

[12] Buzea, C., Pacheco, I. I., & Robbie, K. (2007). Nanomaterials and nanoparticles: sources and toxicity. Biointerphases, 2(4), MR17–MR71. https://doi.org/10.1116/1.2815690 (Acessed June 2021)

[13] Manikandan,V.S.,Adhikarib,B., & Chen,A. (2018).Nanomaterial based electrochemical sensors for the safety and quality control of food and beverages.Analyst,143(19), pp. 4537-4554.

[14] Dresselhaus,M.S., & Eklund,P.C. (2000) Phonons in carbon nanotubes, Advances in Physics,49(6), 705-814. DOI: 10.1080/000187300413184 (Acessed May 2021)

[15] Gleiter H. (2000).Nanostructured Materials: Basic Concepts and Microstructure," Acta material.48 (1), pp. 1-29.

[16] Patrick, T.M. (2017) .Progress in The Development of Semiconducting Metal Oxide Gas Sensors: A Review, Measurement science and technology.28 (8), pp. 820.

[17] Wang, C., Yin, L., Zhang, L., Xiang, D., & Gao, R. (2010).Metal Oxide Gas Sensors: Sensitivity and Influencing Factors. Sensors. 10, 2088-2106. https://doi.org/10.3390/s100302088 (Assessed May 2021)

[18] Arafat, M.M., Dinan, B., Akbar, S.A., & Haseeb, A.S.M.A. (2012).Gas Sensors Based on One Dimensional Nanostructured Metal-Oxides: A Review. Sensors. 12, 7207-7258. https://doi.org/10.3390/s120607207 (Assessed May 2021)

[19] Chen, W., Zhou, Q., Wan, F., & Gao, T. (2012).Gas Sensing Properties and Mechanism of Nano-SnO_2-Based Sensor for Hydrogen and Carbon Monoxide," Journal of nanomaterials, pp. 1-9.

[20] Taylor, R.F., & Schultz, J.S. (1996).Solid State, Resistive Gas Sensors, in Handbook of Chemical and Biological Sensors," in Institute of physics, Philadelphia.

[21] Chauhan, P., & Sharma, S. (2016).Nanomaterials for Sensing Applications. Journal of Nano medicine research. 3(5).

[22] Nanto, H., Morita, T., & Habara, H. (1996).Doping effect of SnO2 on gas sensing characteristics of sputtered ZnO thin film chemical sensor.Sensors and actuators B,. 36,(1-3), pp. 348-387.

[23] Jia, Q., Ji, H., Zhang, Y., Chen, Y., Sun, X., & Jin, Z. (2014). Rapid and selective detection of acetone using hierarchical ZnO gas sensor for hazardous odor markers application. Journal of hazardous materials, 276, pp. 262–270. https://doi.org/10.1016/j.jhazmat.2014.05.044 (Acessed June 2021)

[24] Baratto, C., Sberveglieri,G., Onischuk,.A, B Caruso, B., & Stasio, S. (2014).Low temperature selective NO_2 sensors by nanostructured fibers of ZnO,Sensors and actuators,100(1-2), pp. 261-265.

[25] Hooker, S.A. (2002) Nanotechnology Advantages Applied to Gas Sensor Development, The nanoparticles conference proceedings, USA.

[26] Xu, P et al. (2008).High aspect ratio In_2O_3 nanowires: synthesis and NO_2 gas sensing properties, Sensors and actual, 130, pp. 802-808.

[27] Jin X et al. (2014) .Flexible TiO2/cellulose acetate hybrid film as a recyclable photo catalyst." RCS. 4, pp. 12640-12648.

[28] Freitas, R. R. M., Senna, A. M. , & Botaro, V. R. (2017).Influence of degree of substitution on thermal dynamic mechanical and physicochemical properties of cellulose acetate," Ind. 109, pp. 452-458.

[29] Liu, X. Y., Huang, M., Ma, H. L., Zhang, Z. Q., Gao, J. M., Zhu, Y. L., Han, X. J., & Guo, X. Y. (2010). Preparation of a carbon-based solid acid catalyst by sulfonating activated carbon in a chemical reduction process. Molecules (Basel, Switzerland), 15(10), 7188–7196. https://doi.org/10.3390/molecules15107188 (Assessed June 2021)

[30] Sánchez-Márquez, J.A et al. (2015). Membrane made of cellulose acetate with polyacrylic acid reinforced with carbon nanotubes and its applicability for chromium removal," International journal of polymers, 1(12).

[31] Kumar, N.P., & Munichandraiah, N. (Jun 2012). Rapid sonochemical synthesis of mesoporous MnO_2 for supercapacitor applications. Materials Science and Engineering B, Solid-State Materials for Advanced Technology, 177(11), 849-854. doi:101016/jmseb201204004 (Assessed June 2021)

[32] Wang, T.; Ramnarayanan, A.; & Cheng, H. (2018) Real Time Analysis of Bioanalytes in Healthcare, Food, Zoology and Botany. Sensors, 18, 5. https://doi.org/10.3390/s18010005 (Assessed July 2021)

[33] Horsfall L.A et al. (2017) .An array of WO_3 and CTO heterojunction semiconducting metal oxide gas sensors is used as a tool for explosive detection," Journal of material science.5, pp. 2172-2179.

[34] Minglang, Y., Liu, X.Q., Wang, Y., Youbin, Z., Jiawang, Z., Mingyang, L., Wei, L., & Qing, S. (2012). Gas sensing properties of p-type semiconducting vanadium oxide nanotubes. Applied Surface Science. 258. 9554–9558. 10.1016/j.apsusc.2012.05.120 (Assessed July 2021)

[35] Kim, H.J., & Lee, J.H. (2014).Highly sensitive and selective gas sensors using p-type oxide semiconductors: Overview," Sensors and actuators.192, pp. 607-627.

[36] Quanyi, H., Limiao, L., Xiaoming, Y., Shuang, J., Qiuhong, L., & Taihong, W. (2011). Anomalous conductivity-type transition sensing behaviors of n-type porous α-Fe2O3 nanostructures toward H2S. Materials Science and Engineering B-advanced Functional Solid-state Materials. 176. 600-605. 10.1016/j.mseb.2011.02.002.

[37] Kusior, A., Synowiec, M., Zakrzewska, K., & Radecka, M. (2017).Abnormal p-type sensing response of TiO_2 nanosheets with exposed facets," Journal of alloys and compounds.705, pp. 112-117.

[38] Sifang, L., Guoliang, Y., & Guoqin, C. (2009). Low-Temperature Preparation and Characterization of Nanocrystalline Anatase TiO 2. Journal of Physical Chemistry C - J PHYS CHEM C. 113. 4031-4037. 10.1021/jp8076936.

[39] Kyong, S.H., Vigneswaran, S., Jeevetha, K., Hadi, Z., Kim, J., Cho, D., & Jeong-Hoon K. (2009). Preparation and Characterization of Titanium Dioxide (TiO_2) from Sludge produced by TiCl4 Flocculation with $FeCl_3$, $Al_2(SO_4)_3$ and Ca (OH) $_2$ Coagulant Aids in Wastewater. Separation Science and Technology. 44. 1525-1543. 10.1080/01496390902775810.

[40] Siciliano, T., Tepore, A., Micocci, G., Alessandra, G., Siciliano, M., Emanuela, F. (2009). Transition from n- to p-type electrical conductivity induced by ethanol adsorption on tellurium dioxide nanowires. Sensors and Actuators B: Chemical. 138. 207-213. 10.1016/j.snb.2009.02.007.

[41] Tiemann M. (2007). Porous metal oxides as gas sensors. Chemistry (Weinheim an der Bergstrasse, Germany), 13(30), 8376–8388. https://doi.org/10.1002/chem.200700927.

[42] Eranna, G., Joshi, B.C., Runthala, D.P., & Gupta, R.P. (2004) Oxide Materials for Development of Integrated Gas Sensors—A Comprehensive Review, Critical Reviews in Solid State and Materials Sciences, 29:3-4, 111-188, DOI: 10.1080/10408430490888977

[43] Kanazawa, E et al. (2001). Metal Oxide Semiconductor N2O Sensor for Medical Use," Sensors and actuators. 77(1-2), pp. 72-77.

[44] Henrich V.E. (2013).The Surface Science of Metal Oxides," Cambridge University press, 2013.

[45] Li, C., Zhang, D., Han, S., Liu, X., Tang, T., Lei, B., Liu, Z., & Zhou, C. (2003). Synthesis, electronic properties, and applications of indium oxide nanowires. Annals of the New York Academy of Sciences, 1006, 104–121. https://doi.org/10.1196/annals.1292.007

[46] Karazhanov S et al. (2007).Phase stability, electronic structure, and optical properties of indium oxide polytopes," Physics review. 76 (7), p. 75129.

[47] Makhija, K., Arabinda, R., Patel, R., Urmesh, T., & Himanshu, K. (2005). Indium oxide thin film based ammonia gas and ethanol vapor sensor. Bulletin of Materials Science. 28. 9-17. 10.1007/BF02711165.

[48] Korotcenkov, G., Brinzari, V., Joseph, S., Iuri, B., & Valeriu, C. (2007). The nature of processes controlling the kinetics of indium oxide-based thin film gas sensor response. Sensors and Actuators B-chemical - SENSOR ACTUATOR B-CHEM. 128. 51-63. 10.1016/j.snb.2007.05.028.

[49] Saxena, V., & Chandra, U. (2011). Microwave Synthesis: a Physical Concept. In (Ed.), Microwave Heating. IntechOpen. https://doi.org/10.5772/22888 (Accessed October 2021).

[50] Glasnov, T.N., & Kappe, C.O. (2007)"Microwave-Assisted Synthesis under Continuous-Flow Conditions," Macromolecular rapid communications. 28(4), pp. 395-410.

[51] Hayes, B.L. (2003).The Synergistic Effect of Applied Microwave Energy with Simultaneous Cooling,in International microwaves in chemistry, Gainesville.

[52] Ramesh, S. (2013) Sol-Gel Synthesis and Characterization of Nanoparticles," Journal of nanoscience.2013. Article ID 929321, 8 pages, 2013. https://doi.org/10.1155/2013/929321

[53] Stephen, M., Sandra, L., & Burkett., S.A. (1997). Sol−Gel Synthesis of Organized Matter. Chemistry of Materials, 9(11), 2300-2310. doi: 10.1021/CM970274U

[54] Bhaviripudi, S., Ervin Mile, E.,Steiner, S.A., Zare,A.T. (2007).CVD Synthesis of Single-Walled Carbon Nanotubes from Gold Nanoparticle Catalysts," Journal of American chemistry society.129(6), pp. 1516-1517.

[55] Adachi, M., Kusumi, M., & Tsukui, S. (2004).Ion-induced nucleation in nanoparticle synthesis by ionization chemical vapor deposition." Aerosol science and technology.38 (5), pp. 496-505.

[56] Ealia, A.M., & Saravanakumar, M.P. (2017).A review on the classification, characterization, synthesis of nanoparticles and their application," in IOP conference series: Materials science and engineering, India.

[57] Lugscheider, E., Bärwulf, S., Barimani, C., Riester, M., & Hilgers, H. (1998).Magnetron-sputtered hard material coatings on thermoplastic polymers for clean room applications," Surface coatings technology.108 (109), pp. 398-402.

[58] Byrappa, K., & Yoshimura, M. (2013).Hydrothermal Technology—Principles and Applications," in Handbook of Hydrothermal Technology (Second Edition), William Andrew Publishing, 2013, pp. 1-49.

[59] Jari, K. (2014). Cathodic-Arc and Thermal-Evaporation Deposition. 10.1016/B978-0-08-096532-1.00409-X.

[60] Osama, F., Adel, I., Zaki, Z., Reda M. (2006). Zinc Oxide Thin Films Prepared by Thermal Evaporation Deposition and Its Photocatalytic Activity. Applied Catalysis B: Environmental. 62. 144-149. 10.1016/j.apcatb.2005.07.006.

[61] MoslimIdnan, H., & Rostam, M. (2016). Effect of annealing on optical properties of Zn doped NiO thin films deposited by magnetron sputtering. International Journal of Advanced Research. 4. 280-283. 10.21474/IJAR01/1127.

[62] Leadbeater, N.E., Torenius, H.M. & Tye, H.(2003).Microwave-assisted Mannich-type three-component reactions. Mol Divers 7, 135–144. https://doi.org/10.1023/B:MODI.0000006822.51884.e6

[63] Aljohani, G., Said, M. A., Lentz, D., Basar, N., Albar, A., Alraqa, S. Y., & Ali, A. A. (2019). Microwave-Assisted Synthesis of Mono- and Disubstituted 4-Hydroxyacetophenone Derivatives via Mannich Reaction: Synthesis, XRD and HS-Analysis. Molecules (Basel, Switzerland), 24(3), 590. https://doi.org/10.3390/molecules24030590

[64] Li, W., Fang, X., Lyu, J. et al. (2021).Co_3O_4 Decorated Ti/TiO_2 Nanotubes for Photogenerated Cathodic Protection of 304 Stainless Steel. Chem. Res. Chin. Univ. 37, 704–710. https://doi.org/10.1007/s40242-020-0226-8

[65] Vasant, C., Tillu, V.H., Vijay, N., Hanumant, B., & Radhika, W. (2003). Microwave assisted solvent-free synthesis of dihydropyrimidinones by Biginelli reaction over Si-MCM-41 supported $FeCl_3$ catalyst. Catalysis Communications. 4. 449-453. 10.1016/S1566-7367(03)00111-0.

[66] Mazaahir, K., Shilpi, S., Richa, M., & Venkataramanan, R. (2002). A novel one pot synthesis of nitrogen containing heterocycles: an alternate methodology to the Biginelli and Hantzsch reactions *Journal of the Chemical Society*. http://www.rsc.org/suppdata/p1/b2/b205539m.

[67] Coleman, C. M., MacElroy, J. M., Gallagher, J. F., & O'Shea, D. F. (2002). Microwave parallel library generation: comparison of a conventional- and microwave-generated substituted 4(5)-sulfanyl-1H-imidazole library. Journal of combinatorial chemistry, 4(1), 87–93. https://doi.org/10.1021/cc0100619

[68] Lingayya, R., Vellakkaran, M., Nagaiah, K., Tadikamalla, P. R., & Nanubolu, J. B. (2017). Palladium (ii)-catalyzed direct O-alkenylation of 2-arylquinazolinones with N-tosylhydrazones: an efficient route to O-alkenylquinazolines. Chemical communications (Cambridge, England), 53(10), 1672–1675. https://doi.org/10.1039/c6cc09445g

[69] Ansari M.O., Ansari S.A., Cho M.H., Ansari S.P., Abdel-wahab M.S., & Alshahrie A. (2019) .Conducting Polymer Nanocomposites as Gas Sensors. Polymers and Polymeric Composites: A Reference Series. Springer, Cham. https://doi.org/10.1007/978-3-319-92067-2_25-1

[70] Capelli, L., Sironi, S., & Del Rosso, R. (2014).Electronic Noses for Environmental Monitoring Applications. Sensors. 14, 19979-20007. https://doi.org/10.3390/s141119979

[71] Al-Mashat, L., Debiemme-Chouvy, C., Borensztajn, S., & Wojtek Wlodarski. (2012). Electro polymerized Polypyrrole Nanowires for Hydrogen Gas Sensing," the journal of physical chemistry. 116 (24), pp. 13388-13394.

[72] Radhakrishnan, S., & Deshpande, S.D. (2002). Conducting Polymers Functionalized with Phthalocyanine as Nitrogen Dioxide Sensors. Sensors.2, 185-194. https://doi.org/10.3390/s20500185

[73] Heyu, Y. (2018). CMOS Monolithic Electrochemical Gas Sensor Microsystem Using Room Temperature Ionic Liquid." IEEE Sens J, vol. 18, no. 19, pp. 7899-7906.

[74] Mustafin, A.G., Latypova, L.R., & Andriianova, A.N. (1995).Synthesis and Characterization of Polyaniline Derivatives: Poly (2-alkoxyanilines) and Poly (2, 5-dialkoxyanilines)," Chemistry of materials.7 (1), pp. 33-42.

[75] Yin, H., Mu, X., Li, H., Liu, X., & Mason, A. J. (2018). CMOS Monolithic Electrochemical Gas Sensor Microsystem Using Room Temperature Ionic Liquid. IEEE sensors journal, 18(19), 7899–7906. https://doi.org/10.1109/JSEN.2018.2863644

[76] Schierbaum, K.D., Weimar, U., & Göpel, W. (1986). Multidimensional sensor for gas analysis," Sensors actuators.2 (1), pp. 71-78, 1986.

[77] Bott, B., & Jones, T.A. (1986).The use of multisensory systems in monitoring hazardous atmospheres," Sensors and actuators. 9(1), pp. 19-25.

[78] Palacios, M.A et al. (2008). Rational Design of a Minimal Size Sensor Array for Metal Ion Detection. Journal of the American Chemical Society.130 (31), 10307-10314. DOI: 10.1021/ja802377k

[79] Grate, J.W., & Abraham, M.H. (1987).Multicomponent Analysis Using an Array of Piezoelectric Crystal Sensors". Analytical." Chemistry American chemical society, vol. 59, no. 11, pp. 1529-1534.

[80] Heinze, J., Frontana-Uribe, B. A., & Ludwigs, S. (2010). Electrochemistry of Conducting Polymers—Persistent Models and New Concepts. Chemical Reviews, 110(8), 4724–4771. https://doi.org/10.1021/CR900226K

[81] Le, T., Kim, Y., & Yoon, H. (2017).Electrical and Electrochemical Properties of Conducting Polymers," Polymers. 9(4), pp. 150.

[82] Yu, Y.Z., Wong, Y.K., & Garito, A.F. (1997) .Nonlinear Optics of Organic Molecules and Polymers," Optical engineering. 36(9), pp. 2622.

[83] Roth, S., & Carroll, D. (1999). Handbook of Conducting Polymers, 2nd Edition," IEEE Electrical insulation magazine. 15(1), pp. 37-39.

[84] Zhang, X.-G. et al. (2010) .Synthesis of 1-Substituted 2-(Trifluoromethyl) Indoles Via a Palladium-Catalyzed Double Amination Reaction," Chemistry synthesis, 9, pp. 1521-1525.

[85] MacDiarmid A.G et al. (2001).Electrostatically-Generated Nanofibers of Electronic Polymers, Synthetic Metals.119 (1-3), pp. 27-30.

[86] Tang, Q., Wu, J., Sun, X., Li, Q., & Jianming Lin. (2009).Shape and Size Control of Oriented Polyaniline Microstructure by A Self-Assembly Method," Langmuir American society. 25(9), pp. 5253-5257.

[87] Deronzier, A., & Moutet, J-C. (1996).Polypyrrole Films Containing Metal Complexes: Syntheses and Applications"," Coordination chemistry reviews. 147, pp. 339-371.

[88] Wang, Y., & Levon, K. (2012).Influence of Dopant on Electro activity of Polyaniline," Macromolecular symposia, .1, pp. 317-318.

[89] Bavane, R.K.G et al. (2014).Ammonia Gas Sensing Characteristics of Spin Coated Polyaniline Films. Journal of advances in physics. 3(3), pp. 241-248.

[90] Srinives, S., Sarkar, T., & Mulchandani, A. (2013).Nano thin Polyaniline Film for Highly Sensitive Chemiresistive Gas Sensing.," Electro analysis. 25(6), pp. 1439-1445.

[91] Fratoddi, I., Venditti,I., Cametti,C., & Russo, M.V.(2015).Chemiresistive polyaniline-based gas sensors: A mini review. Sensors and actuators. 220, pp. 534-548.

[92] Mekki, Ahmed & Joshi, Nirav et al. (2014).H2S sensing using in situ photo-polymerized polyaniline–silver nanocomposite films on flexible substrates. Organic Electronics. 15. 71–81. 10.1016/j.orgel.2013.10.012.

[93] Adorinni, S., Cringoli, M.C., Perathoner, S., Fornasiero, P., & Marchesan, S.(2021). Green Approaches to Carbon Nanostructure-Based Biomaterials. Appl. Sci., 11, 2490. https://doi.org/10.3390/app11062490

[94] Uthaman, S., Lee, S.J., Cherukula, K., Cho, C-S., & In-Kyu P. (2015).Polysaccharide-Coated Magnetic Nanoparticles for Imaging and Gene Therapy", BioMed Research International, vol. 2015, Article ID 959175, pp.14. https://doi.org/10.1155/2015/959175 (Assessed July 2021)

[95] Dorobantu, D., Bota, P.M., Boerasu, I. et al. (2014). Pulse laser ablation system for carbon nano-onions fabrication. Surf. Engin. Appl.Electrochem. 50, 390–394. https://doi.org/10.3103/S1068375514050044 (Accessed July 2021)

[96] German, C-S et al. (2005). Induction plasma synthesis of fullerenes and nanotubes using carbon black–nickel particles. Carbon. 43. 3153-3166. 10.1016/j.carbon.2005.06.018.

[97] Qiao, Z., Li, J., Zhao, N., Shi, C., & Nash, P. (2006).Graphitization and microstructure transformation of Nano diamond to onion-like carbon." Science material, vol. 54, no. 2, pp. 225-229.

[98] Robertson, J., & O'Reilly, E.P. (1987).Electronic and atomic structure of amorphous carbon," Matter materials and physics. 35, pp. 2946-2957.

[99] Mathioudakis, C et al. (2005).Electronic and optical properties of tight-binding molecular dynamics simulations," Thin solid films. 482, pp. 151-155.

[100] Zhang, Z., Wen, Z., Ye, Z., & Zhu, L. (2015). Gas sensors based on ultrathin porous Co_3O_4 nanosheets to detect acetone at low temperature. RSC Advances, 5, 59976-59982.

[101] Isokoski, K., Poteet, C.A., & Linnartz, H. (2013). Highly resolved infrared spectra of pure CO_2 ice (15−75K). Astron. Astrophysics, p. 55.

[102] Mykhailiv, O., Zubyk, H., & Plonska-Brzezinska, M.E. (2017). Carbon nano-onions: Unique carbon nanostructures with fascinating properties and their potential applications. Inorganica Chimica Acta, 468, 49-66.

[103] Bartelmess, J., Giordani, S., & Beilstein J. Nanotechnol. 2014, 5, 1980–1998. doi:10.3762/bjnano.5.207

[104] Mykhailiv, O et al. (2015). Chemical versus Electrochemical Synthesis of Carbon Nano-onion/Polypyrrole Composites for Supercapacitor Electrodes.," Chemistry European journal, vol. 21, pp. 5783-5793.

[105] Anthony, P., Brzezinska, P.M., Olena, M., Luis, E., & Ilias, E. (2015). Combined high permittivity and high electrical conductivity of carbon nano-onion/polyaniline composites. Synthetic Metals. 209. 583-587. 10.1016/j.synthmet.2015.08.020.

[106] Gradzka E et al. (2013). Comparison of the electrochemical properties of thin films of MWCNTs/C60-Pd, SWCNTs/C60-Pd and ox-CNOs/C60-Pd.," Electrochemistry actuators. 96, pp. 274-284.

[107] Peng C et al. (2008) .Polyaniline/single-wall carbon nanotube (PANI/SWCNT) composites for high-performance supercapacitor. Electro him," Electrochemistry actuators, 52 (4), pp. 1721-1726.

[108] Heba I.A et al. (2015) .An additional tool towards overcoming the absence of specificity of carbon nanostructure-based electrochemical sensors application to estriol and estradiol detection and distinction." J. Solid State Electrochemistry. 19, pp. 3045-3050.

[109] Okechukwu, V.O et al. (2019).Concomitant in Situ FTIR and Impedance Measurements to Address the 2-Methylcyclopentanone Vapor-Sensing Mechanism in MnO2–Polymer Nanocomposites," ACS omega. 4(5), pp. 8324-8333.

[110] Zhang, J., Guo, J., Xu, H., & Cao, B. (2013).Reactive-Template Fabrication of Porous SnO_2 Nanotubes and Their Remarkable Gas-Sensing Performance.," ACS Applied Materials & Interfaces.5(16), pp. 7893-7898.

CHAPTER 3

MICROWAVE-ASSISTED HYDROTHERMAL SYNTHESIS OF In_2O_3 NANOSTRUCTURES AND THE SYNTHESISES OF POLYANILINE

3.1 Introduction

Metal oxide nanoparticles, such as Al_2O_3, MgO, ZrO_2, AgO, TiO_2, ZnO, In_2O_3, and others, have attained considerable attention in recent years because to their novel features in comparison to their bulkier rivals, such as compact size and high density of edge surfaces [1]. The magnetic, conducting, chemical and electrical properties of these materials have prompted extensive research into new applications, such as batteries, magnetic storage media, gas sensors, solar cells, catalysis, energy conversion, architecture, medicine, food, agriculture, cosmetics, textiles, and antennas [2]. Indium oxide (In_2O_3), has large bandgap n-type semiconductor with a direct bandgap of approximately 3.6 eV. It has gained considerable attention for its potential applications at room temperature in solar cells, field-emission displays, lithium-ion batteries, nanoscale biosensors, optoelectronics, and photocatalysis and gas sensors, [3].

Chemical vapour deposition, sol-gel, microemulsion, and spray pyrolysis, are all methods utilized to manufacture these metal oxides. The microwave-assisted hydrothermal process has been highly utilized in recent years for nanoscale synthesis [4]. This is because the addition of microwaves to hydrothermal processes enables rapid, easy, and cost-effective methods of obtaining the desired products from a chemical reaction [5]. The microwave (MW) creates uniform reaction heating, which enables a more homogenous size distribution of the component's materials, which is not possible with other heating procedures. Additionally, the solvents employed is environmentally friendly and hazardous by-products can be eliminated or minimized [6].

This opens up the possibility of using microwave reactors in industrial applications for the bulk production of nanomaterials. Controlling numerous factors such as solvent, reaction time, temperature, and strain, allows for the resolution of issues such as nanomaterial particle size and shape [7]. The use of a stabilizing agent to control the shape and size of nanomaterials has been widely investigated and has been demonstrated to be a viable alternative method for achieving

the desired attributes of crystalline nanostructures. However, this is limited in the application of nanomaterials [8].

The goal of this study was to look into an alcohol reduction method for synthesizing indium oxide that does not require annealing and compare the results to those from a conventional method that does require annealing. It is well known that indium hydroxide may be dehydrated through heat treatment to create indium oxide with comparable morphologies and sizes. The conventional method entails converting indium hydroxide to indium oxide. However, in this investigation, the indium hydroxides were synthesized using the same microwave power of 700 watts at varying reaction times (10 minutes, 20 minutes, 30 minutes, 45 minutes, and 1 hour). The In (OH) $_3$ products were heated for two hours at 400 °C to convert them to In_2O_3. Separately, the formed indium oxides were employed to create a ternary composite (In_2O_3/PANI/OLCs). The composites were then employed as gas sensing layers, and their effectiveness was evaluated (refer to chapter 6). For the sake of simplicity, the indium oxide synthesized via the alcohol reduction approach will be referred to as B-In_2O_3, while the one synthesized by the standard method will be referred to as Y-In_2O_3. TEM (Transmission electron microscope), XRD (X-ray Diffraction), FTIR (Fourier transform Infrared), UV-Vis (Ultraviolet–Visible spectroscopy), BET (Brunauer-Emmett-Teller), SEM (Scanning Electron Microscopy) were used to characterize the synthesized materials and XPS (X-ray photoelectron spectroscopy).

This chapter is divided into two parts:

1.1 Synthesis and characterization of B-In_2O_3 and Y-In_2O_3

1.2 Synthesis of polyaniline

3.1.1 Synthesis and characterization of B-In_2O_3 and Y-In_2O_3

3.1.2 Procedure for conducting experiments

3.1.2.1 Reagents

The microwave-assisted hydrothermal synthesis of indium oxides described in this work is a modification of an existing approach [9]. Sigma Aldrich supplied indium (III) nitrate hydrate [In $(NO_3)_3$. xH_2O], hexamethylenetetramine [HMT, $C_6H_{12}N_4$], and acetone, which were used

without additional purification. MK chemicals supplied the ethanol, and WITS University's School of Chemistry produced the deionized water.

3.1.2.2 Synthesis of Y-In_2O_3

The measured amounts of indium (III) nitrate hydrate [In $(NO_3)_3$. xH_2O] and hexamethylene-tetramine [HMT, $C_6H_{12}N_4$] were dissolved in water separately in different containers. The solutions were then transferred to a set of Teflon lined vessels, mounted onto the rotor and further transferred to a microwave reactor operating at 700W for 10 minutes. The reactor was then cooled and the white indium hydroxide precipitate was centrifuge, washed several times with deionized water, and oven-dried at 120℃ for 6 hours. After annealing the indium hydroxide at 400 degrees Celsius for two hours, a yellow indium oxide was formed.

3.1.2.3 Synthesis of B-In_2O_3

The measured amounts of indium (III) nitrate hydrate [In $(NO_3)_3$. xH_2O] and hexamethylene-tetramine [HMT, $C_6H_{12}N_4$] were dissolved in ethanol separately in different containers. The solutions were then transferred to a set of Teflon lined vessels, mounted onto the rotor and further transferred to a microwave reactor operating at 700W for 10 minutes. The reactor was cooled and the brown precipitate was centrifuge washed several times with water, ethanol and acetone, and oven-dried at 120℃ for 6 hours.

3.1.2.4 Characterization techniques

A Bruker Tensor 27 Fourier Transform Infrared spectrometer was used for the FTIR spectroscopy analysis. After dispersing the samples in ethanol, dropping them on a carbon tape, and coating them with a layer (10 nm) of gold–palladium and a layer (10 nm) of carbon, SEM examination was done at 20 kV on a ZEISS SIGMA 03–39 FESEM. The materials were disseminated in ethanol by ultrasonication and then put onto a lace carbon copper grid for TEM examination using a Tecnai Spirit T12 at 120 kV. PXRD data was recorded on a Bruker D2 Phaser using Cu radiation, with each scan lasting 1 hour. The surface area and pore volume were determined using a Micromeritics Tristar 3000 surface area and porosity analyser.

3.1.3.1 Reaction mechanism of Y-In_2O_3 and B-In_2O_3 synthesis

The solvent plays a significant role in nanoparticle development and assembly. The interaction of the nanoparticle surface with the solvent molecules, as well as the solvent molecules with the ligand molecules, has a substantial effect on the final particle size and shape. [10]. Ethanol is used as a solvent and HMT acts as a structural guiding agent, but it also limits particle growth by forming a shield around the nanoparticle to restrict further growth. It is also stated that HMT may be hydrolysed in distilled water and progressively produces OH^- ions at a temperature of 100 ˚C, the mechanism is described by equations three to six. [11].

$$In(NO_3)_3.H_2O + 3C_2H_5OH \rightarrow In(OH)_3 + 3C_2H_5NO_3 + H_2O \quad (1)$$

$$In(OH)_3 \xrightarrow{MW,\ 700W} In_2O_3 \quad (2)$$

$$(CH_2)_6N_4 + 6H_2O \rightarrow 6COH_2 + 4NH_3 \quad (3)$$

$$NH_3 + H_2O \rightarrow NH_4^+ + OH^- \quad (4)$$

$$In(NO_3)_3.H_2O \rightarrow In^{3+} + NO^{3-} + H_2O \quad (5)$$

$$2In^{3+} + 6OH^- \rightarrow In_2O_3 + 3H_2O \quad (6)$$

When the reactions do not incorporate microwaves (equation 1); annealing will be required regardless of whether the reaction is conducted in the presence of water or ethanol. When microwaves are used, reactions conducted in the presence of ethanol do not require annealing (equation 2); however, when water is used, annealing is required to obtain In_2O_3. To understand why we cannot just go to the desired product because microwave is used in both circumstances, one must first understand how microwave heats different solvents. The ability of a solvent to absorb microwave energy is significant; ethanol is a high microwave absorber when compared to water [12], thus it heats up quickly within the microwave chamber, producing indium oxide in a single step. Water takes longer to achieve required temperatures, therefore the product offered is indium hydroxide, which requires dehydration to yield indium hydroxide. Figure 3.1 illustrates formation of Y-In_2O_3 and B-In_2O_3.

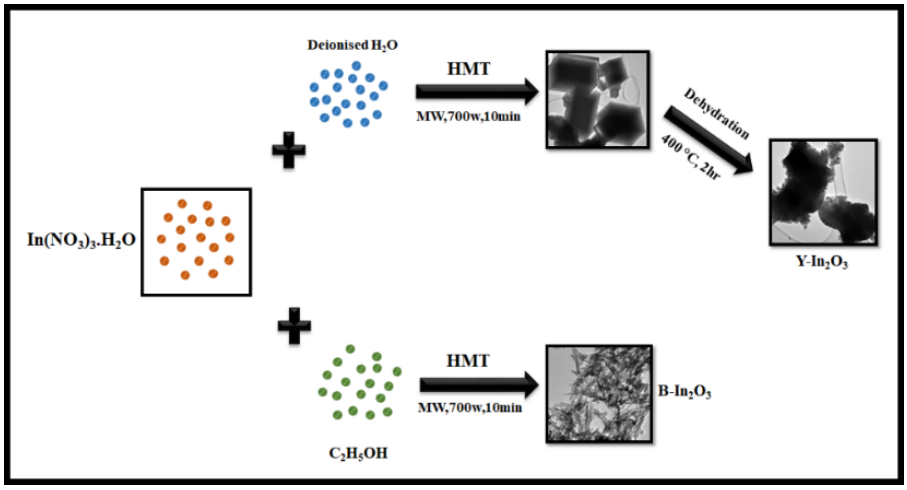


Figure 3.1.1 Schematic illustration of formation of Y-In_2O_3 and B-In_2O_3

3.1.4 Discussion of the findings

3.1.4.1 Transformation of In $(OH)_3$ to Y-In_2O_3 under various microwave exposure conditions.

3.1.4.2 XRD

As illustrated in Figure 3.1.2, the crystallinity of as-prepared samples generated using the hydrothermal microwave aided technique was assessed using XRD. Figure 3.1.2 (a) depicts the diffraction patterns of indium hydroxides generated at various microwave radiation periods. Microwave exposure durations of 10 and 20 minutes yielded indium oxyhydroxide (InOOH) with an orthorhombic lattice, as validated by PDF 01-078-4503. The cubic indium hydroxides were confirmed by PDF 00-058-0465, PDF 01-078-4503, and PDF 01-071-2277 as the exposure period increased (30 minutes, 45 minutes, and 1 hour). The XRD patterns of indium oxides produced after annealing the InOOH and In $(OH)_3$ at 400 degrees Celsius for 2 hours are shown in Figure 3.1.2 (b). Zhuang et al. [13] found comparable results with hexagonal indium oxides, In_2O_3 (10min and 20min). PDF 01-084-4697, PDF 01-083-8123, and PDF 01-083-8123, respectively, confirm that In_2O_3 (30 min, 45 min, and 1hr) are cubic phase indium

oxides. Estimating particle size of In_2O_3 products was challenging due to the uneven morphologies and severe agglomeration indicated by the particles generated in this chapter (refer to Figures 3.1.4 (a_2-e_2) and 3.1.5(a_2-e_2)), hence only the average crystalline dimension was obtained utilizing the Scherrer equation. The sizes of prepared indium oxides are shown in Table 3.1.1. The peak broadening of the peaks in the XRD pattern is a technique for determining the size of nanoparticles [14]. The Scherrer equation is illustrated below:

$$D=K\lambda/\beta\cos\theta,$$

The mean size of the nanoparticles is denoted by D, the form factor is denoted by K, the X-ray wavelength is denoted by λ, the full width at half maximum is denoted by β, and the tilt between the X-ray source and detector is denoted by θ [15].

Table 3.1.1 Average particle size of In_2O_3 prepared from dehydration of indium hydroxide

Sample	Peak position $_{avg}$ (Rad)	FWHM $_{avg}$ (Rad)	Particle size $_{avg}$ (nm)
$In_2O_{3\ (10\ min)}$	39.2	0.6	13.2
$In_2O_{3\ (20\ min)}$	32.2	0.6	12.6
$In_2O_{3\ (30min)}$	42.1	0.8	10.7
$In_2O_{3\ (45min)}$	36.0	0.5	15.9
$In_2O_{3\ (1hr)}$	38.4	0.2	33.1

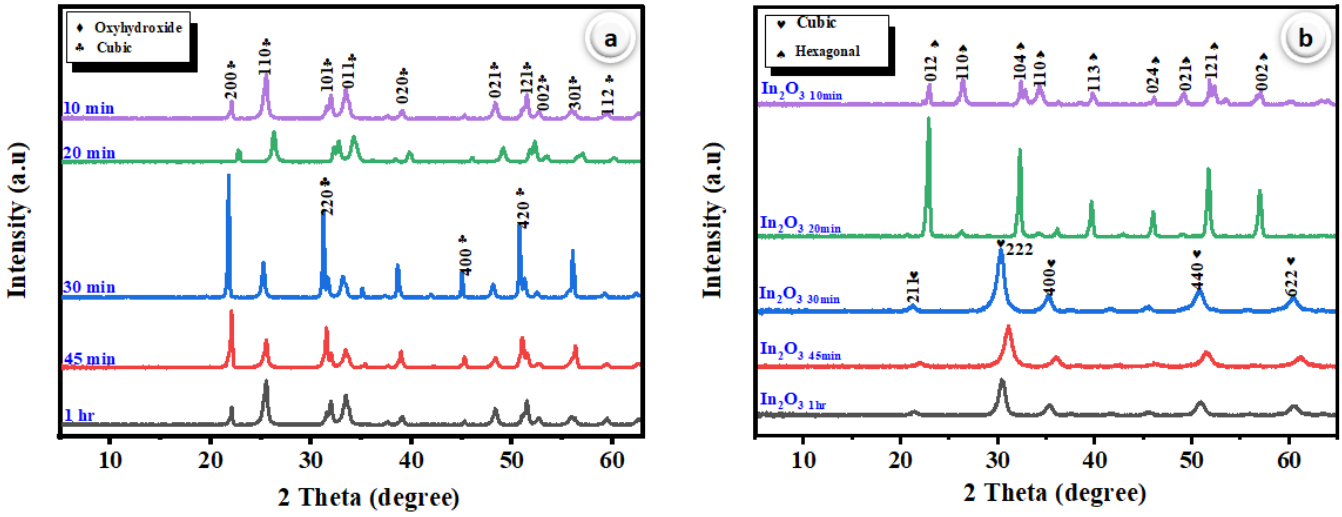


Figure 3.1.2 XRD diafactograms of (a), In $(OH)_3$ at 10 min, 20 min, 30 min, 45 min, and 1hr of microwave radiation and (b) In_2O_3 after annealing indium hydroxides

3.1.4.3 FTIR

Figure 3.1.3 (a) shows the FTIR spectrums of indium hydroxides, which are identical to the one previously reported by Mullicaet et al. [16]. Spectrums shows the absorption peaks for OH^- [1] stretching vibrations (3250 and 3133 cm^{-1}), bending vibrations (1250 and 1150 cm^{-1}), the In-OH group (855 and 789 cm^{-1}), and In–O stretching vibrations (527 cm^{-1}). In figure 3.3(b) depicts the FT-IR spectra of the In_2O_3 nanoparticles. The bands at 400 to 600 cm^{-1} are typical of In-O bending in In_2O_3, but the bands for In_2O_3(10min) and In_2O_3 (20min) aren't as strong as those for In_2O_3 (30min), In_2O_3 (45min), and In_2O_3 (1hr), which could be because of different lattices seen in XRD analysis. Table 3 shows the IR assignment bands of the prepared hydroxides and oxides.

Table 3.1.2 FTIR assignment bands of (a) In $(OH)_3$ and (b) In_2O_3 prepared from Dehydration of indium hydroxide

Wavenumber (cm^{-1})	Functional groups
3250-3133	O-H Stretching
1250-1150	O-H Bending
400-600	In-O Stretching vibration

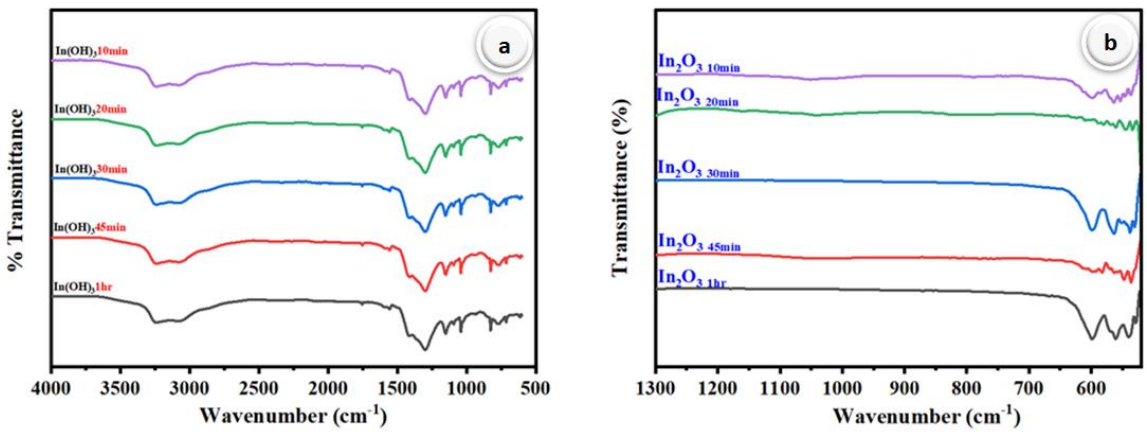


Figure 3.1.3 FT-IR spectra of (a) In $(OH)_3$ synthesized under different MW reaction times and (b) In_2O_3 after annealing In_2O_3

3.1.3.4 SEM and TEM

Figure 3.1.4 (a_1-e_1) depicts SEM images of $In(OH)_3$ exposed to the same microwave power (700w) for ten minutes, twenty minutes, thirty minutes, forty-five minutes, and one hour, as

well as In_2O_3 from annealed indium hydroxides for 2 hours at 400 degrees Celsius (Figure 3.1.4 (a2-e2)). A morphology consisting of rectangular bars, cubes, and flower-like nanoparticles of indium hydroxide is formed as shown in Figure 3.1.4 a_1. After the annealing tiny particles are generated and the morphology in a scaffold pattern appears, as shown in Figure 3.1.4 a_2. When comparing Figure 3.1.4 b_1 to Figure 3.4 a_1, the cubes and rectangular bars are relatively smaller and a flower-like morphology emerges. After annealing of b_1 (Figure 3.1.4 b_2), the scaffold structure appears somewhat deformed with aggregated small particles. A uniform flower-like morphology is observed in Figure 3.1.4 c_1. After annealing, the cluster shown in figure 3.4 b_2 changed into smaller spherical nanoparticles (Figure 3.1.4 c_2). The flower-like morphology is completely obliterated as the exposure period increases (Figure 3.1.4 d_1 and e_1), and smaller spherical aggregates appear after annealing (Figure 3.1.4 d_2 and e_2). This demonstrates that the reaction time has a significant effect on the size and morphology of the nanomaterials.

TEM images of indium hydroxides (a_1-e_1) and indium oxides (a_2-e_2) are shown in Figure 3.1.5. Figure 3.1.5 a_1 and b_1 illustrate morphology composed of a combination of rectangular bars and cubes. Figure 3.1.5 a_2 and b_2 illustrate an oblique morphology associated with strongly aggregated particles. Figure 3.1.5 Image c_1 illustrates a flower-like morphology, whereas Figure 3.5 c_2 depicts a spheroidal morphology with varying-sized lattice fringes. Their morphology is hardly distinguishable in Figures 3.1.5 d_1 and e_1. Figure 3.1.5 d_2 illustrates what appears to be irregular fibres, while figure e_2 illustrates a spherical aggregation of the irregular fibres in figure 3.1.5 d_2. These findings are consistent with SEM images.

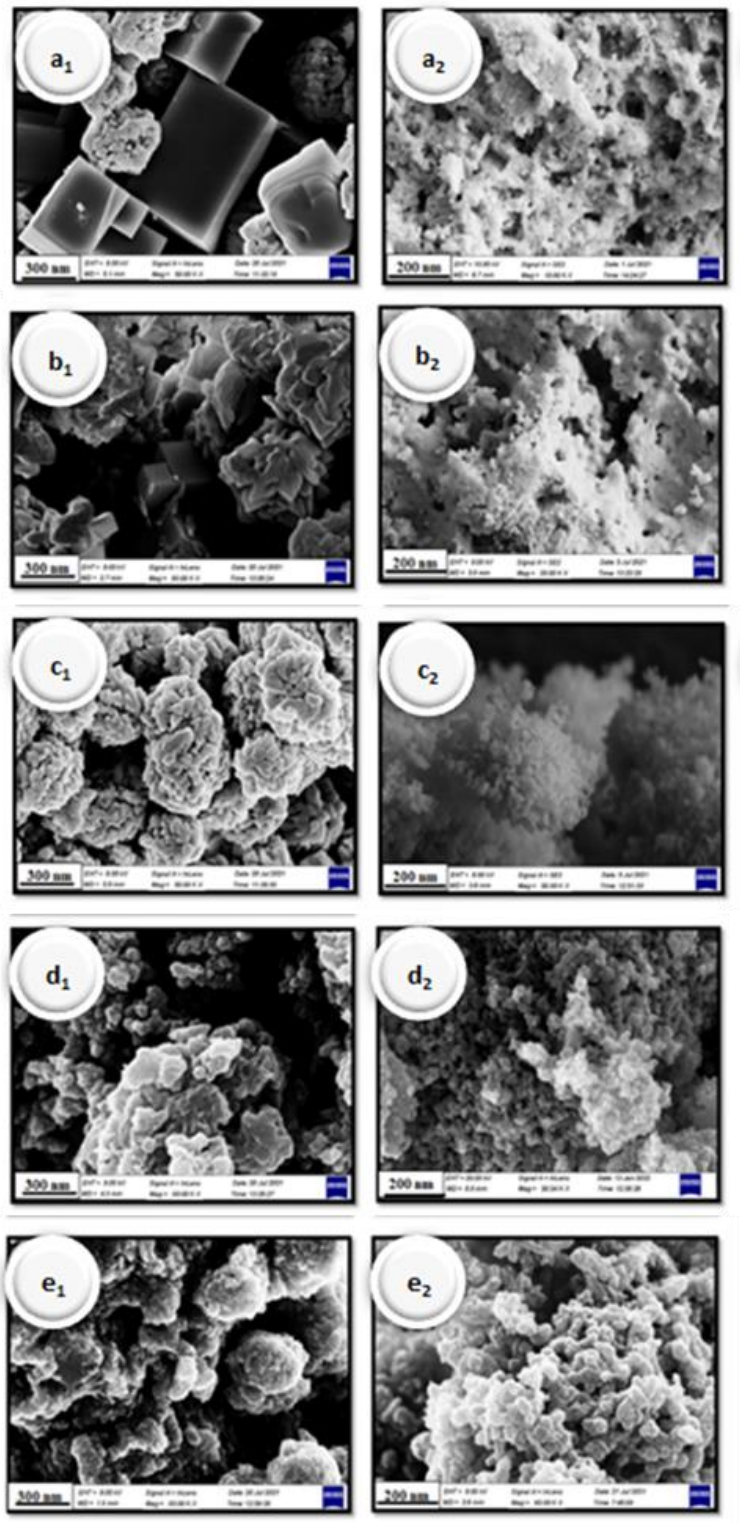


Figure 3.1.4 SEM micrographs of In $(OH)_3$ at different microwave irradiation times (10min-1hr (a_1-e_1)) and the In_2O_3 after annealing indium hydroxides (a_2-e_2)

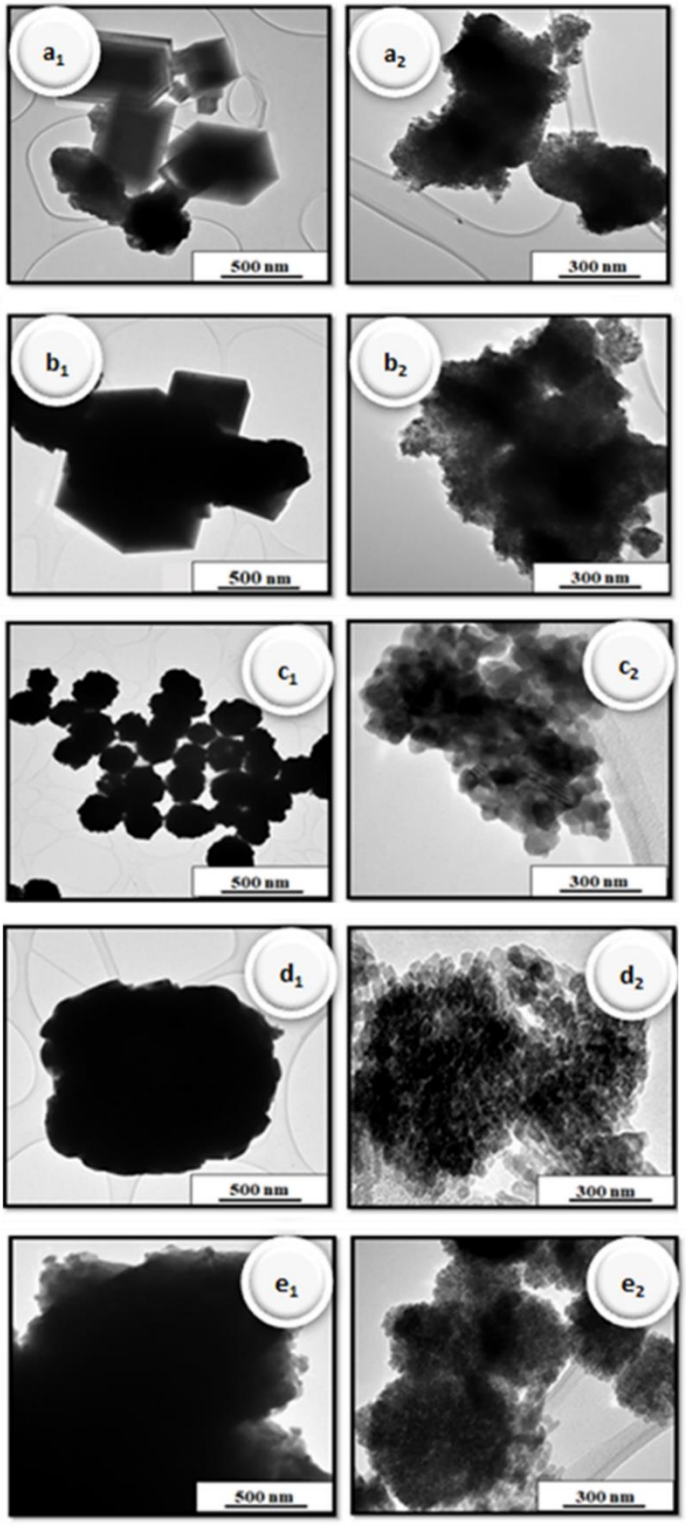


Figure 3.1.5 TEM micrographs of In $(OH)_3$ at different microwave irradiation times (10min-1hr (a_1-e_1)) and the In_2O_3 after annealing indium hydroxides (a_2-e_2)

Y-In_2O_3 and B-In_2O_3 comparison

Sol-gel, chemical precipitation/co-precipitation, microemulsion, and many other wet chemical paths for the synthesis of nano-scale metal oxides typically take a long time. Owing to its excellent in providing a higher rate of synthesis than conventional heating, microwave-assisted processing has garnered a lot of interest. Volumetric heating is possible because microwaves can penetrate materials and deliver energy, causing heat to be produced throughout the material's volume. The speed of reactions is increased by a factor of 10-1000 when it is possible to raise the temperature of a reaction well above the boiling point of the solvent. As a result, reactions are finished in minutes or even seconds [17].

The following are just a few of the benefits of microwave synthesis [18,19,20,21] : (i) faster reactions and higher yields by combining sealed-vessel (autoclave) technology with fast microwave heating; (ii) use of solvents with lower boiling points under pressure (closed vessel conditions) and heating them to temperatures much higher than their boiling point; (iv) heating the reaction mixture "in core," without the effects of walls or heat diffusion; (v) no direct contact between the energy source and the chemicals being reacted; (vi) preferential heating; and (vii) direct molecular heating and inverted temperature gradients.

Although the microwave method was used to create both Y-In_2O_3 and B-In_2O_3, using ethanol as a solvent instead of water had additional benefits because it produced the desired product (abbreviated as B-In_2O_3) without the need for annealing, which is required when using water as a solvent because indium hydroxide is what initially forms. This last observation is supported by the fact that ethanol absorbs microwave energy more effectively than water.

3.1.4.1 FTIR

Figure 3.1.6 depicts IR spectra of Y-In_2O_3 and B-In_2O_3, in most cases, interatomic vibrations in metal oxides create absorption bands less than 1000 cm^{-1}, The features of In-O vibration were assigned absorption bands in the range (679 – 550 cm^{-1}) [22].

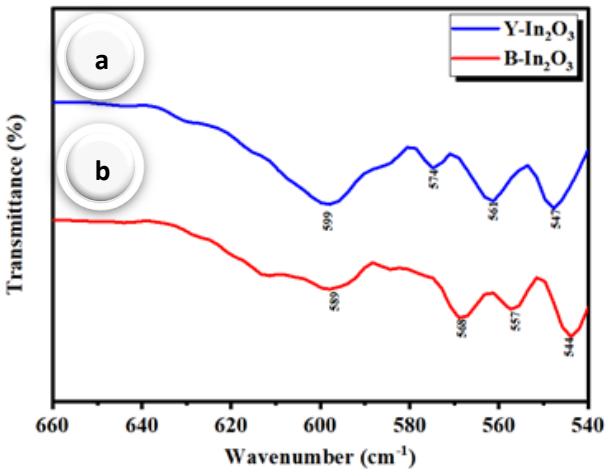


Figure 3.1.6 FT-IR spectra of (a) Y-In_2O_3 and (b) B-In_2O_3

3.1.4.2 XRD

XRD analysis was used to determine the crystal structure of Y-In_2O_3, and B-In_2O_3 nanoparticles. Y-In_2O_3 with eight peaks, as shown in Figure 3.1.7, which were assigned to crystal planes (2 1 1), (2 2 2), (4 0 0), (4 1 1), (3 2 2), (4 3 1), (4 4 0), (6 1 1), and (6 2 2), respectively. The XRD pattern revealed the cubic structural phase of In_2O_3 with no impurities [23]. B-In_2O_3 has eight peaks, as illustrated in Figure 3.1.7 which was allocated to crystal planes (2 1 1), (2 2 2), (4 0 0), (4 1 1), (3 2 2), (4 3 1), (4 4 0), (6 1 1), and (6 2 2), respectively, but when compared to Y-In_2O_3, the peaks are somewhat shifted to higher values of 2 Theta. The peak shifts are attributed to lattice distortion caused by defects in the crystal structure. The XRD peak positions shift to either a higher or lower angle as a result of tensile or compressive strain [24]. The Scherer equation was utilised to ascertain the average particle size of the produced indium oxides (Table 3.1.3)

Table 3.1.3 Particle sizes of Y-In_2O_3 and B-In_2O_3, calculated using Scherrer equation

Sample	Peak position $_{avg}$ (°)	FWHM $_{avg}$ (°)	Particle size $_{avg}$ (nm)
Y-In_2O_3	42.1	0.8	10.7
B-In_2O_3	45.8	0.9	9.4

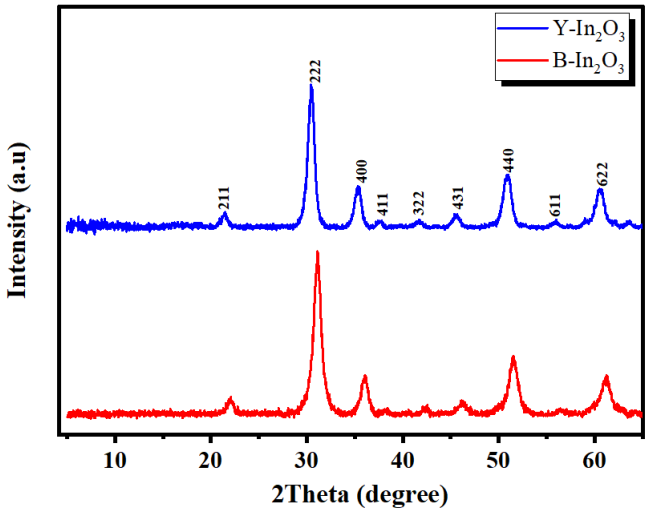


Figure 3.1.7 X-ray diffractogram of Y-In_2O_3 and B-In_2O_3

3.1.4.4 SEM and EDS

The morphological analysis of indium oxide nanoparticles has been studied using SEM. Figure 3.1.8 (a) depicts the morphology of Y-In_2O_3 discovered to be aggregated spheres, while figure 3.1.8 (b) depicts the morphology of B-In_2O_3 discovered to be nanorods. The elemental composition of the produced samples, Y-In_2O_3, and B-In_2O_3 was determined by energy-dispersive X-ray (EDS) spectroscopy, as shown in Figure 3.1.8 (c & d). The EDS spectrum exhibited main peaks of In and O ions, indicating that indium oxide was produced.

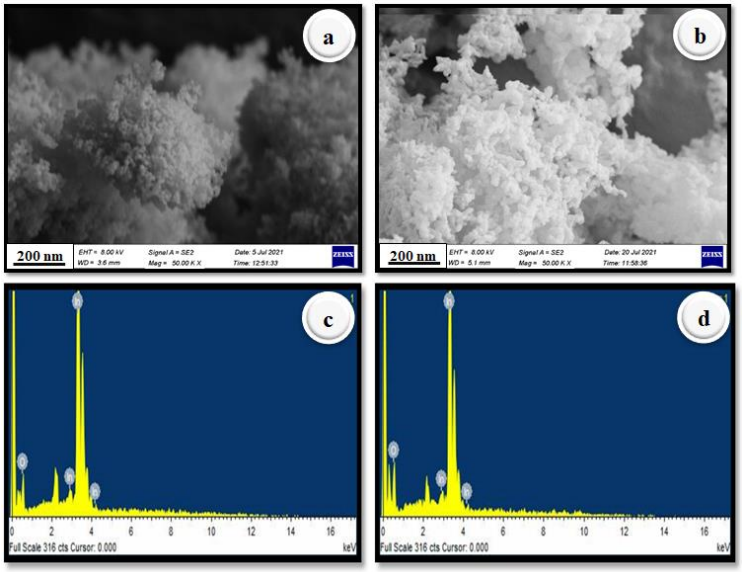


Figure 3.1.8 SEM micrographs of, (a) Y-In_2O_3, (b) B-In_2O_3 and EDS spectra of, (c) Y-In_2O_3, (d) B-In_2O_3

3.1.4.4 TEM

Figure 3.1.9 shows TEM micrographs of indium oxide products. Figure 3.1.9 (a) depicts a TEM image of aggregated Nano grains of Y-In_2O_3 that were obtained after two hours of annealing indium hydroxide at 400 degrees Celsius, the original morphology of the indium hydroxide was destroyed, presumably because of water evolution and weight loss (Figure 3.1.5 c_1) [25]. Figure 3.1.9 (b) displays the morphology of B-In_2O_3, which was produced using the alcohol solvent approach and did not require annealing; it has a Nano rod form. Following this, it is clear that the synthesis conditions used, have an effect on the morphological outline of the final product. In this case, ethanol addition as a solvent, the microwave and the reagents, were able to produce uniform rod-like structures.

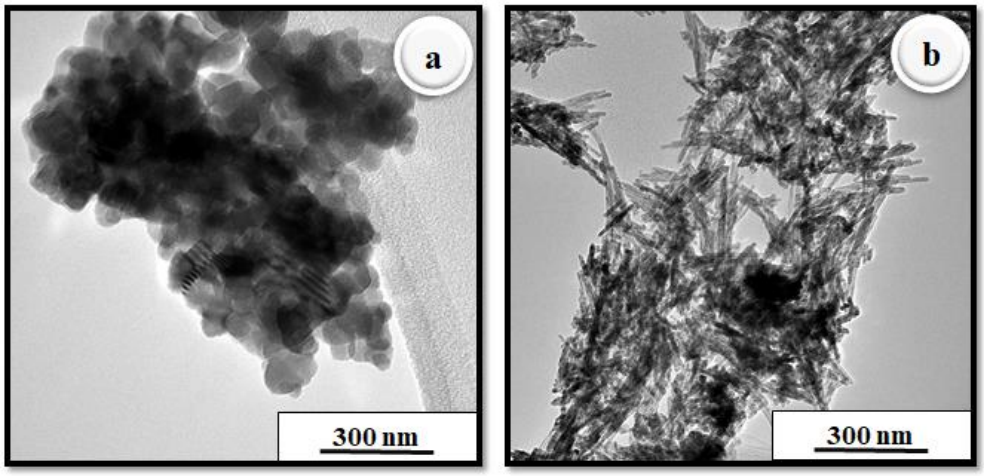


Figure 3.1.9 TEM micrographs (a) Y-In_2O_3 and (b) B-In_2O_3

3.1.4.5 UV-Visible Spectroscopy

The optical properties of Y-In_2O_3 and B-In_2O_3 nanoparticles were investigated using UV-Visible absorption spectroscopy. Figure 3.1.10 illustrates the absorbance spectra of Y-In_2O_3 and B-In_2O_3 nanoparticles (a & b). Y-In_2O_3 has an absorbance peak of 302 nm, while B-In_2O_3 has an absorbance peak of 297 nm. Different parameters like particle size, bandgap, oxygen vacancies, and others influence the absorbance peak of materials [26]. Tauc's equation [27] was used to compute the energy band gap of Y-In_2O_3 and B-In_2O_3. The energy band gaps of Y-In_2O_3 and B-In_2O_3 are 3.2 eV and 3.6 eV, respectively, as shown in the inserted graphs in Figure 3.1.10 (a & b). The particle size and band gap are affected by the annealing temperature. In general, the optical band gap of In_2O_3 nanoparticles increases with increasing annealing temperature

[28], which is due to improved crystallinity and a decrease in oxygen deficiency [29], and this statement accounts for the difference in band gaps obtained in this study. Rashed et al. discovered a comparable band gap to that of B-In_2O_3 [30].

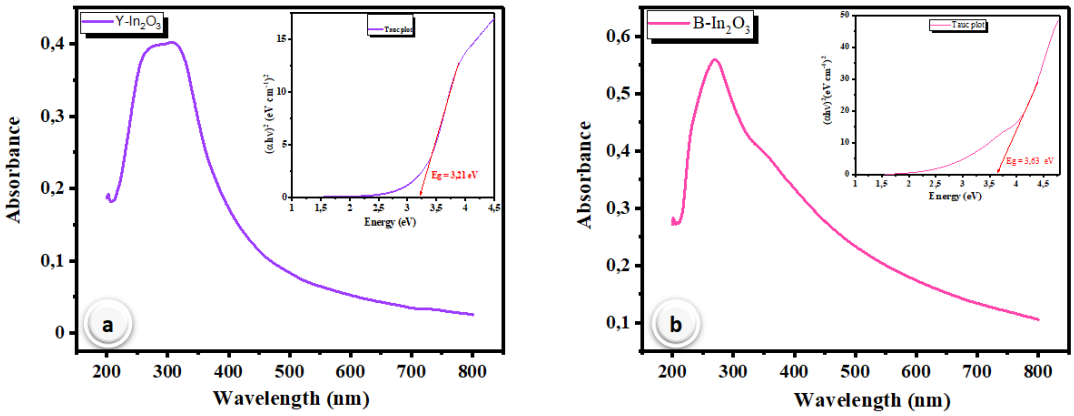


Figure 3.1.10 UV spectra of (a) Y-In_2O_3 and (b) B-In_2O_3

3.1.4.6 BET

Surface area and permeability of Y-In_2O_3 and B-In_2O_3 samples were determined using the N_2 adsorption-desorption method. Figure 3.1.11 (a & b) exhibit typical type III isotherms to pressure differential (0.1< P/P0 <1.0) with a type H3 hysteresis loop and no clear saturation adsorption platform, indicating highly irregular pore structures [31]. Table 3.1.4 lists the particle properties of Y-In_2O_3 and B-In_2O_3, such as, pore diameter, surface area and volume distribution. The surface area of B-In_2O_3 is much greater than that of Y-In_2O_3. This may be due to grain growth which may have occurred during the annealing step to obtain Y-In_2O_3. The Barrett–Joyner–Halenda (BJH) method was used to determine the pore-size distribution. Pore diameters in Y-In_2O_3 range from 6 to 65 nm. The pore size diameters of the B-In_2O_3 sample is around 35 nm; both materials appear to be mesoporous based on the pore size values.

Table 3.1.4 BET surface area, pore size and pore volume distribution of Y-In_2O_3 and B-In_2O_3

Sample	Surface area ($m^2 g^{-1}$)	Pore size (nm)	Pore volume ($cm^3 g^{-1}$)
Y-In_2O_3	20.2	28.4	0.15
B-In_2O_3	45.3	28.7	0.33

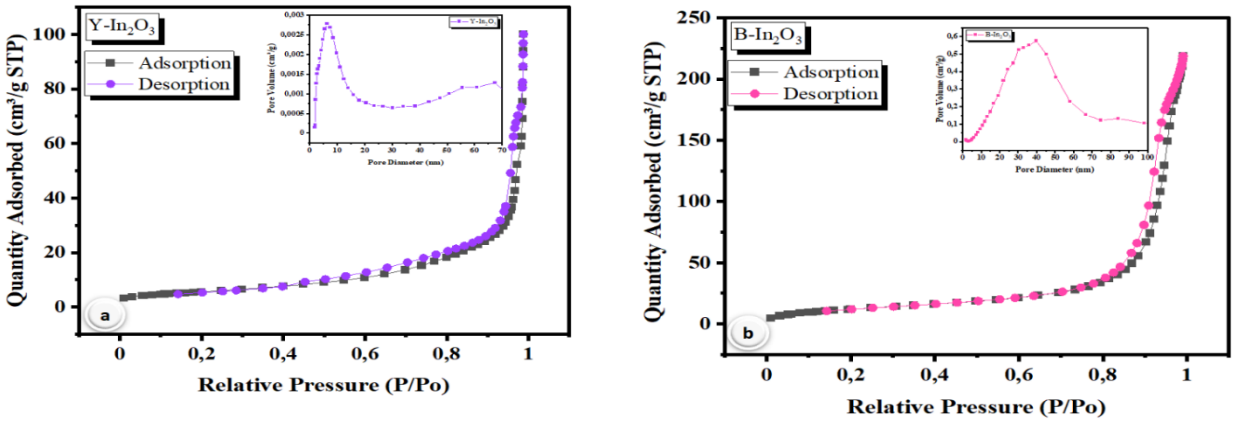
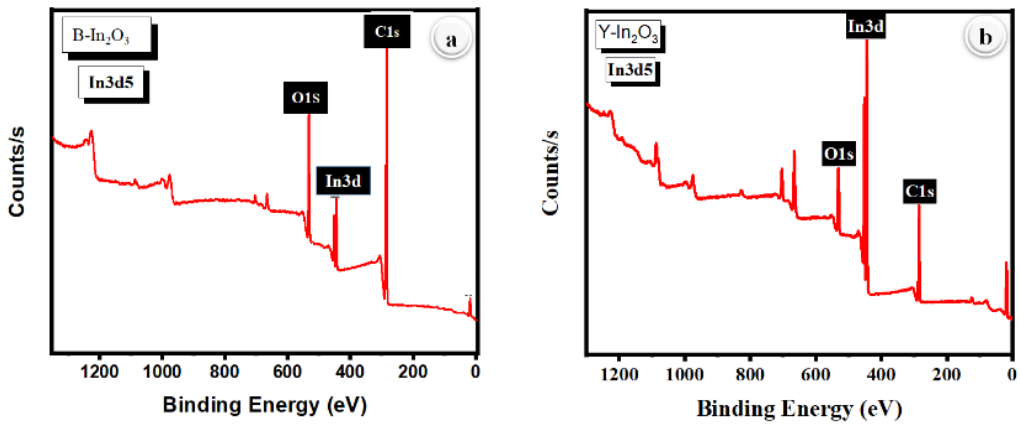


Figure 3.1.11 BET isotherm curves and Pore size diameter curve of (a) Y-In_2O_3 and (b) B-In_2O_3

3.1.4.7 XPS

The electronic structure and composition of Y-In_2O_3 and B-In_2O_3 were studied using X-ray photoelectron spectroscopy. Figure 3.1.12 (a & b) display the survey XPS spectra of Y-In_2O_3 and B-In_2O_3, which clearly shows distinct peaks at roughly 500, 440, and 230 eV, correlating to O, In, and inadvertent C [32], correspondingly for In_2O_3. The O1s XPS curves of B-In_2O_3 and Y-In_2O_3 are shown in Figure 3.1.12 (c & d), respectively. There are three prominent peaks positioned at approximately 531,532, and 533 that can be attributed to lattice oxygen (O_{lat}), deficient oxygen (O_{def}), and surface oxygen (O_{abs}), respectively [33]. Figure 3.1.12(e & f) shows a high-resolution spectrum of In3d of Y-In_2O_3 and B-In_2O_3, with peaks at 452 and 440 eV corresponding to the $3d_{3/2}$ and $3d_{5/2}$ spin-orbitals, respectively, demonstrating the existence of the In^{3+} oxidation state [34].



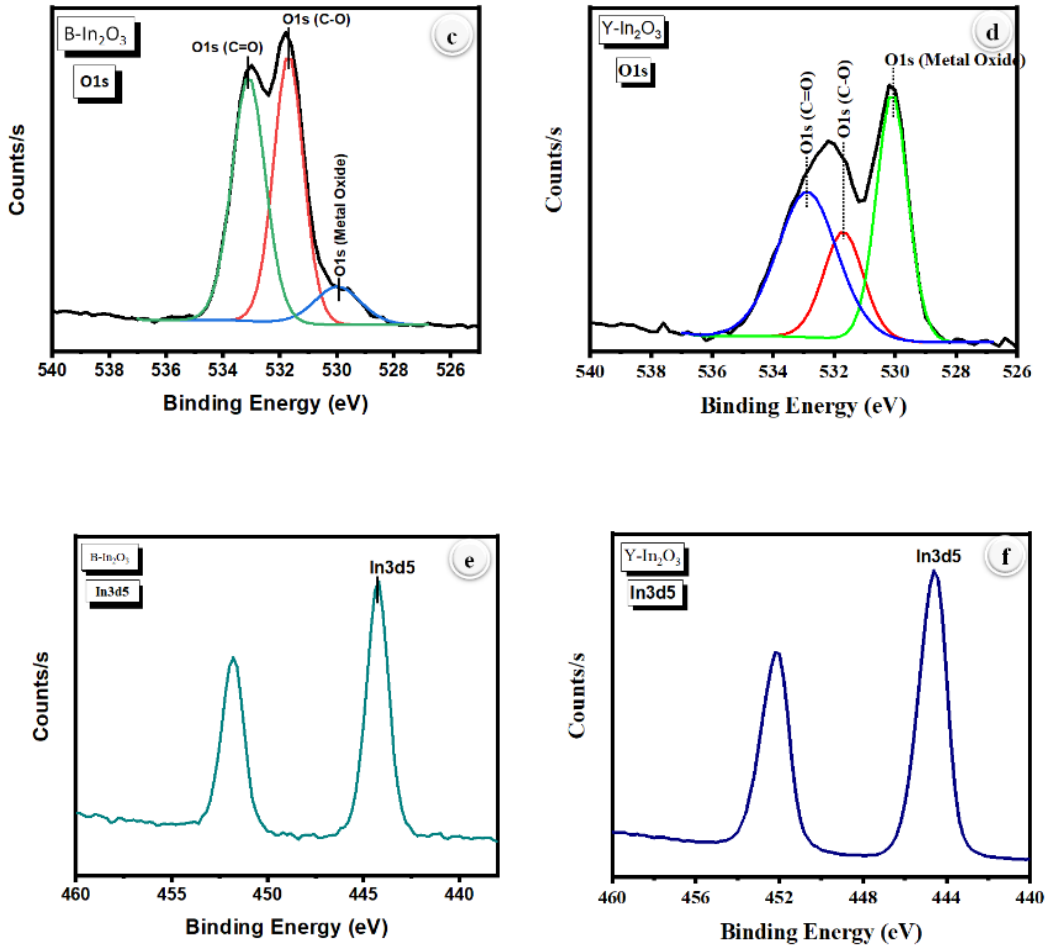


Figure 3.1.12 XPS (a & b) survey, (c & d) O1s XPS curves and (e & f) O1s of Y-In_2O_3 and B-In_2O_3

3.1.5 Conclusion

The effective synthesis of Y-In_2O_3 and B-In_2O_3 was validated using XRD, FT-IR, UV-Vis, TEM, and SEM. Time investigations of the synthesis of Y-In_2O_3 show that microwave power influences size, morphology and crystalline phase of the produced materials. From the comparison of Y-In_2O_3 and B-In_2O_3, the XRD analysis revealed that the produced materials are polycrystalline, although the diffraction peaks of B-In_2O_3 were somewhat shifted to higher 2-theta values when compared to Y-In_2O_3. Y-In_2O_3 and B-In_2O_3 had an average crystalline diameters of 10.7 and 9.4 nm, respectively. The morphology of Y-In_2O_3 was discovered to be nanograins, whereas the morphology of B-In_2O_3 was shown to be nanorods. The existence of all the predicted elements, including oxygen and indium, was confirmed by EDS. The existence

of functional groups was confirmed by FTIR for the produced materials, and so was the complete transformation of indium hydroxide to Y-indium oxide. The UV absorption spectra of Y-In_2O_3 and B-In_2O_3 nanoparticles displayed peaks at 302 and 297 nm, respectively, and the energy band gaps were determined to be 3.2 and 3.6 eV using the Tauc's plot. The surface areas of Y-In_2O_3 and B-In_2O_3 determined by BET were 20.2 and 45.3 $m^2 g^{-1}$, respectively. Following these observations, it is possible to conclude that the process of synthesis affects the properties of the materials. X-ray photoelectron spectroscopy was used to investigate the electronic structure and composition of Y-In_2O_3 and B-In_2O_3, confirming that indium oxides were successfully produced.

3.2 Synthesis of polyaniline

3.2.1 Introduction

The conducting polymer family includes polyaniline (PANI), poly (3,4ethylenedioxythiophene) (PEDOT), polypyrrole (PPY), polythiophene (PTh), and their derivatives [35]. PANI has gotten a lot of attention among conducting polymers because of its unique properties, which include simple and reproducible doping and dedoping chemistry, steady electrical conductance mechanisms, enormous environmental stability, and facile synthesis, all of which point to potential electrical device applications. PANI may be produced using either electrochemical or chemical polymerization techniques. The polymerization process employed must give accurate structures and morphologies, hence, chemical polymerization is preferred over electrochemical polymerization [36]. In acidic environments, chemical polymerization employs aniline as a monomer and ammonium persulfate (APS) as an oxidant. Interfacial polymerization, the hard template method, the soft template technique, electrospinning, and the quick mixing method are methods utilized to synthesize PANI [37].

The latter polymerization procedure is particularly important since it is the most practical approach for large-scale polyaniline manufacturing. Since the early 1980s, conductive polymers have been utilized as the active ingredient in gas sensors [38]. Conduction in these polymers is extremely complicated, as their electrical conductivity ranges by around a factor of fifteen,

which is ascribed to the creation of non-linear defects such as solitons, polarons, or bipolarons during the doping or polarization processes of monomer units [39]. Conducting polymers have several advantages, including the ability to work at room temperature and the ability to alter their chemical and physical properties utilizing various substituents. These features make conducting polymers ideal sensing layers for room-temperature gas sensors.

Sensors employing conducting polymers in various transduction modes have been developed in recent years. These sensors can be classified into five main classes: (i) amperometric mode (measurement of the current generated by an analyte's redox reaction at a sensing/working electrode) (ii) conductometric mode (changes in electrical conductivity), (iii) potentiometric mode (changes in chemical potential without current flow), (iv) colourimetric mode (changes in optical absorption), and (v) gravimetric mode (the shift in the polymer's mass as a result of analyte–polymer interaction.) [40].

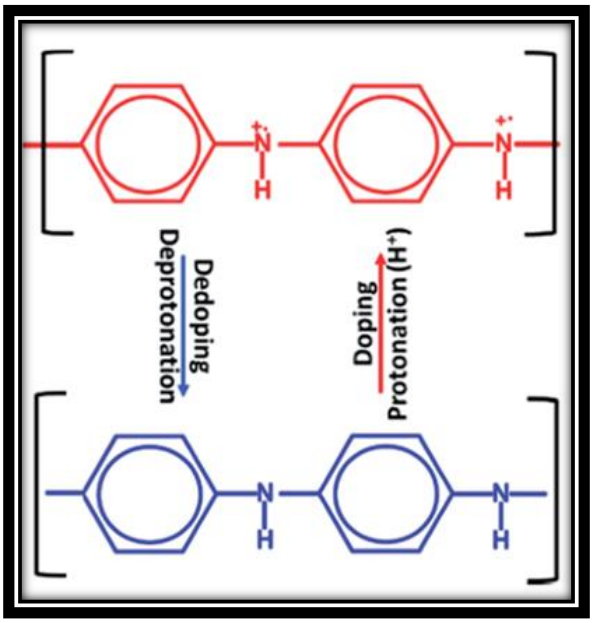


Figure 3.2.1 Doping and de-doping of PANI [7]

A common feature of these polymers is that they have a low conductivity in their pure state on the order of 10^{-10} S.cm^{-1}, that can be easily increased to values in the range of 10^{3}–10^{5} S.cm^{-1} using a doping method (Figure 3.2.1). By eliminating some electrons (either chemically or electrochemically), the polymer core becomes electrified, and the cation radical works as a charge transfer [41]. Hauang J and Cesario A observed that when several inorganic acids such

as HCl (hydrochloric acid), H_2SO_4 (sulphuric acid), and H_3PO_4 (phosphoric acid) were used to synthesize PANI, the reaction temperature was kept constant at zero degrees Celsius, and the emeraldine salts were washed with ethyl ether, ethanol, and distilled water, before being dried under a vacuum (0.075 mega pascals) at 50 degrees Celsius for 48 hours. PANI structures with sizes from 150 to 340 nm and conductivities varying from 0.1 to 10 S cm^{-1} were obtained

[42 & 43]. Olinga et al. reported that the solubility, structure, and conductance of PANI can be considerably altered by doping it with bulky protonic acids like dodecyl benzene sulfonic acid (DBSA, camphor sulphonic acid (HCSA) and p-toluene sulfonic acid (p-TSA) [44]. The lengthy alkyl chains of PANI's alkyl chains acted as surfactants, enhancing both its solubility and processing capabilities. Numerous attempts have been made to further enhance the PANI's characteristics through surface modification using nanomaterials such as carbon-based materials, and metal oxide semiconductors for gas sensing applications [45].

Because of the changes made to PANI's physicochemical properties, the gas sensing qualities of the resulting composites are projected to improve dramatically [46]. PANI was doped with HCl in this study using a rapid polymerization technique and then mixed with OLCs and In_2O_3 (in chapter 5) to generate a ternary composite suitable for room temperature gas sensing. XRD (X-ray diffraction), FTIR (Fourier transform infrared spectroscopy), TEM (transmission electron microscope), UV-Vis (Ultra Violet-visible spectroscopy) were used to characterize the produced PANI.

3.2.1 Procedure for conducting experiments

3.2.1.1 Reagents

All of the reagents in this study, including aniline monomer, hydrochloric acid (HCl), and ammonium persulfate (APS), were acquired from Sigma-Aldrich (South Africa) and utilized without additional purification.

3.2.1.2 Synthesis of HCl doped Polyaniline nanowhiskers

Rapid polymerization was used to synthesize PANI nanowhiskers as depicted in Figure 3.2.2. In a typical reaction, 5g APS was dissolved in 50 ml 1M HCl and 2 ml aniline was added to 50 ml 1M HCl separately. At ~0°C, APS (oxidant) solution was added to aniline solution with rapid stirring. Following the polymerisation, the resultant samples were filtered and washed

repeatedly with 1M HCl followed by distilled water until the supernatant was colorless subsequently, the product was washed with acetone and dried overnight at 60°C.

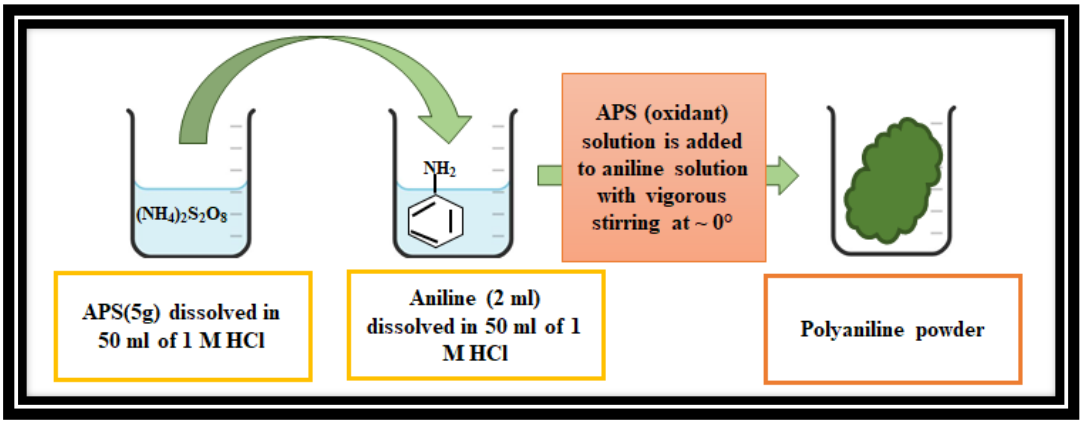


Figure 3.2.2 Graphical illustration of PANI synthesis via rapid polymerization

3.2.2 Techniques for Characterization

A Bruker Tensor 27 Fourier Transform Infrared spectrometer was used for the FTIR spectroscopy analysis. The TEM examination was performed at 120 kV using a Tecnai Spirit T12, and the samples were ultrasonically scattered in ethanol before being put onto a lacey carbon copper grid. ImageJ analysis software was used to determine the size of TEM PANI particles. PXRD data was gathered using a Bruker D2 Phaser and Cu emission, with each scan lasting one hour. The Tristar 3000 surface area and porosity analyzer was utilyzed to figure out the surface area and pore volume.

3.2.3 Discussion of the findings

3.2.3.1 TEM

Figure 3.2.3 (a & b),depicts the TEM images of the prepared PANI . The average thickness of PANI nanowhiskers [47] is 37± 9 nm (Figure 3.2.3 (c)). The nanofibers accrete, the accretion may be related to the presence of chloride ions, which generate a large number of agglomerated nanofibers as a consequence of the PANI backbone coiling effect caused by salt formation with the chloride ion [48]. The nanowhiskers generated in our investigation

had a reduced average thickness when compared to previously reported data using a similar method [49]. The decreased thickness size of PANI in this work may be a result of the experimental circumstances such as the extended polymerization times result in the creation of smoother and thinner PANI nanowhiskers, with the possibility of longer PANI nanowhiskers [50].

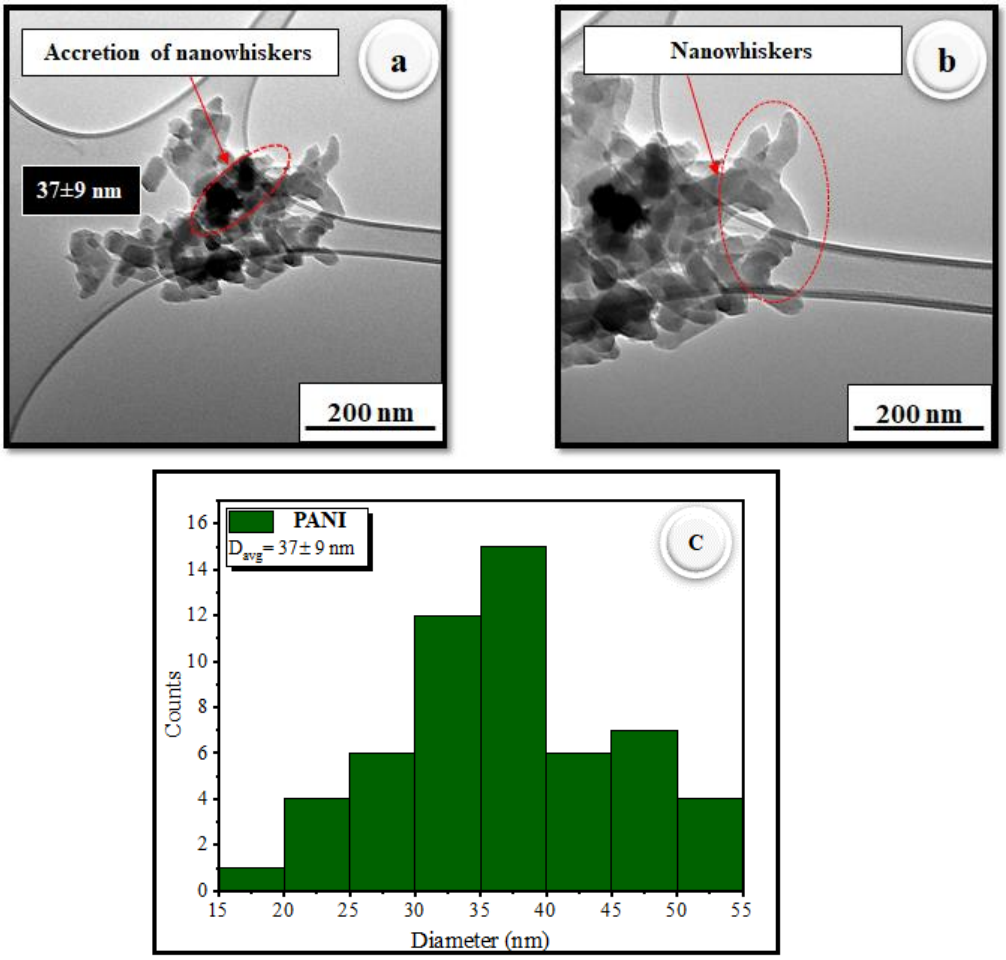


Figure 3.2.3 TEM micrographs (a & b) and (c) average particle size histogram of PANI

3.2.3.2 XRD

Figure 3.2.4 shows the XRD profile of the prepared PANI exhibited four unique peaks centred at 2θ = 9°,15°, 21°, and 25°, corresponding to the (011), (020),(100), and (200) crystal planes of PANI and all peaks are concurring with the outcomes of Pouget et al. and Rahul et al [51 & 52]. These peaks show that the PANI produced is semi-crystalline. This inherent semi-

crystallinity, according to the literature, is caused by the existence of polar nitrogen sites in the polymer backbone[53]. Additionally, the presence of polarons improves this crystallinity, resulting in increased conductance. The inter-chain spacing between neighbouring benzene rings causes the peak at 2θ = 21°, and the degree of conjugation in PANI nanofibers causes the peak at 2θ=25°[54 & 55].

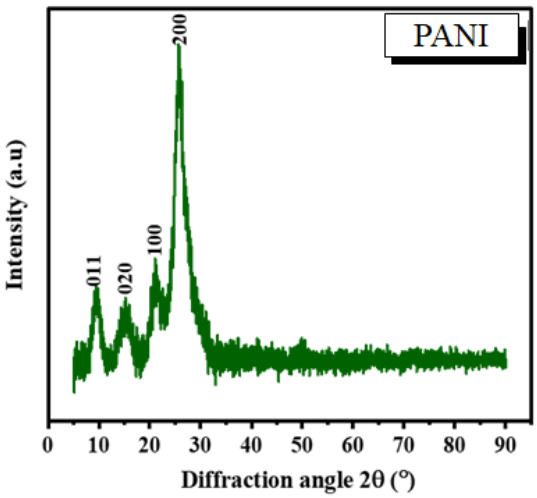


Figure 3.2.4 XRD diffractogram of PANI

3.2.3.3 FT-IR Spectroscopy

Figure 3.2.5 clearly shows that there are typical absorption bands, as given in Table 3.2.1, where the peak at 3440 cm^{-1} represents the N–H stretching peak for secondary aromatic amine and an aromatic bond's C-H stretching is responsible for a 2918 cm^{-1} peak and the band at 1293 cm^{-1} represents the C–N stretching band [56]. The major bands of protonated PANI are at 1632 and 1474 cm^{-1} are due to the stretching vibrations of the quinonoid and benzenoid rings, respectively. "The band at 1632 cm^{-1} is caused by the C = C vibration of the quinonoid ring (Q), while the band at 1474 cm^{-1} is caused by the C = C vibration of the benzenoid ring (B)" [57]. Protonation "doping" of PANI is demonstrated by the appearance of a band at 2363 cm^{-1} that carries the stretching vibration of (NH^{+}) tertiary amine salt [58]. PANI formation is indicated by the band at 609 cm^{-1}, which is suggestive of para scattered aromatic rings. [59-61]. Because the stretching vibration of B-NH^{+}=Q, a strong band at 1140 cm^{-1} and a broad strong absorption tail at 2300-2800 cm^{-1} appear, and these two bands are considered the most important FTIR bands to evidence that high electrical conductance and a elevated degree of

electron delocalization in polyanilines exist [62]. When compared to undoped PANI made in the same way by Kotresh et al. [63], the doped PANI had lower peak intensities and moved to lower wavenumbers, which is due to the HCl dopping.

Table 3.2.1 Assignments of main FTIR bands of PANI

Wavenumber (cm^{-1})	Functional groups
3440	N-H secondary amine stretch
2918	C-H of aromatic ring
2363-2853	Tertiary amine salt
1632	C=C quinoid rings
1474	C=C benzenoid rings
1293	C-N in secondary amine
1140	B-NH^{+}=Q
955	Para substitution on aromatic rings
607	N-H wagging for secondary amine

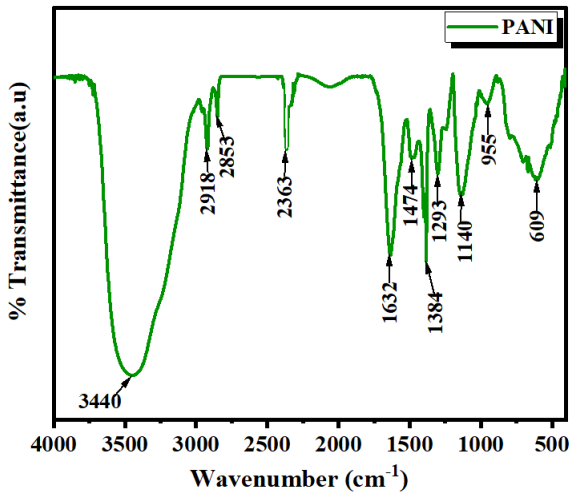


Figure 3.2.5 FT-IR spectra of PANI

3.2.3.4 BET

The particulate characteristics of PANI, such as surface area, pore size, and pore volume, were examined using the BET technique in nitrogen adsorption and desorption environments. Table 3.2.2 shows the particulate properties of PANI, such as surface area, pore size, and pore volume, which were determined to be 30.2 m^2g^{-1}, 32.8 nm, and 0.25 cm^3g^{-1}, respectively. The curves reveal Type-I isotherms typical of mesoporous and microporous materials with pore

diameters ranging from 4 to 100 nm (figure 3.2.7 (a)). Type-I isotherms have a significant rise in the amount of nitrogen adsorbed and desorbed at high relative pressures. The specific surface area achieved in this study is equivalent to that reported by Xu et al and Ayad et al for PANI produced under identical polymerization conditions [64 & 65].

Table 3.2.2 BET surface area, pore size and pore volume distribution of PANI

Measurements	PANI
Surface area (m^2g^{-1})	30.2
Pore size (nm)	32.8
Pore volume (cm^3g^{-1})	0.25

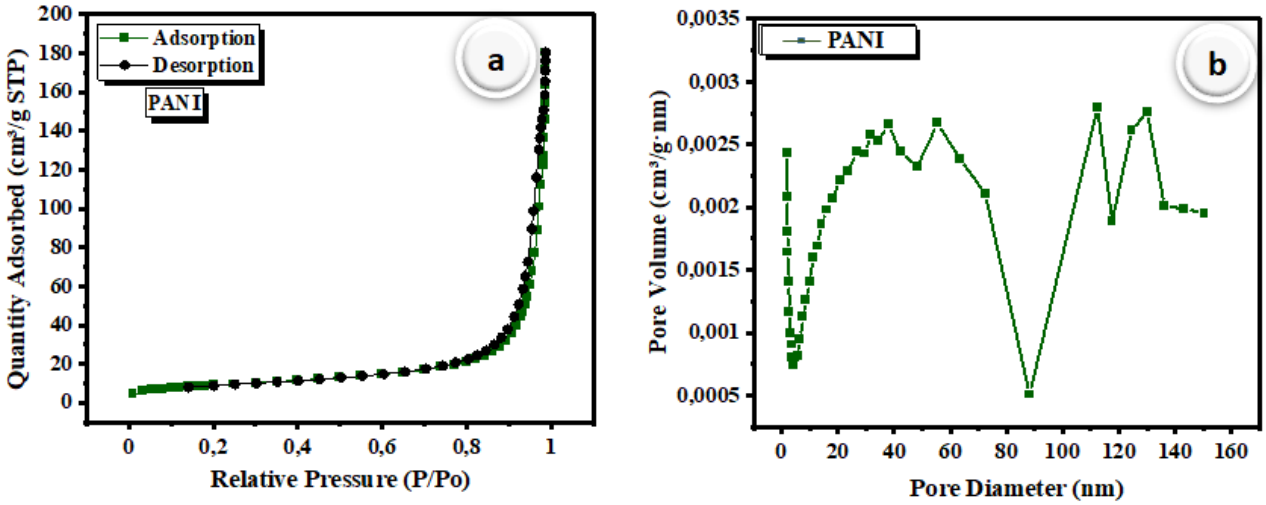


Figure 3.2.6 (a) BET isotherm curve and (b) Pore size distribution curve of PANI

3.2.3.5 UV-Vis spectroscopy

The UV-Vis spectrum of PANI is shown in Figure 3.2.7. The figure shows three distinct absorption peaks; the indication of PANI conductive polymer formation is the maximum absorption peak at 222-338 nm, which represents a $\pi \rightarrow \pi *$ transition of a conjugated ring system, and the absorption band at 351 nm, which may be ascribed to $n \rightarrow \pi *$ transition, these findings support the development of polaron bands in the bandgap of polymers after HCl doping [66]. The exciton absorptions of quinoid units are responsible for the third absorption peak at 589-600 nm. These findings are consistent with the findings in previous research reports. [67].

Table 3.2.3 Uv-Vis absorption peak positions of PANI

Measurements	Wavelength (nm)
π ⟶ π*	222-338
π ⟶ bi-Polaron transition	351
Exciton of quinoid rings	589

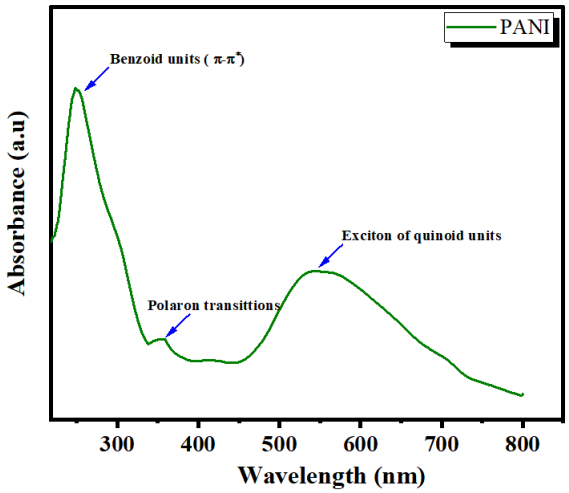


Figure 3.2.7 UV-Vis spectra of PANI

3.2.4. Conclusion

XRD, FT-IR, UV-Vis, TEM, and SEM images were used to validate the successful synthesis of HCl doped PANI through the rapid polymerization method. The XRD analysis revealed that PANI is polycrystalline. FT-IR research also revealed that PANI was successfully doped, resulting in reduced peak intensities and peak shifts to lowered wavenumbers in the presence of counter ions. Uv-Vis analysis revealed that all of the expected PANI transitions were found, verifying polyaniline's efficient HCl doping. PANI had an average size of 37±9 nm according to TEM and BET surface area, pore size and pore volume were determined to be 30.2 m^2g^{-1}, 32.8 nm and 0.25cm^3g^{-1}, respectively.

3.5 References

[1] Chandradass, J., Bae, D. S., & Kim, K. H. (2011). A simple method to prepare indium ox-ide nanoparticles: Structural, microstructural and magnetic properties. Advanced Powder Technology, 22(3), 370–374. https://doi.org/10.1016/j.apt.2010.05.006.

[2] Wu, P., Li, Q., Zhao, C., Zhang, D., Chi, L., & Xiao, T. (2008). Synthesis and photoluminescence property of indium oxide nanowires. Applied Surface Science, 255(5), 3201–3204. https://doi.org/10.1016/j.apsusc.2008.09.032.

[3] Cao, J., Wang, J., Fang, B., Chang, X., Zheng, M., & Wang, H. (2004). Microwave-assisted Synthesis of Flower-like ZnO Nanosheet Aggregates in a Room-temperature Ionic Liquid. Chemistry Letters, 33(10), 1332–1333. https://doi.org/10.1246/cl.2004.1332.

[4] Pimentel, A., Nunes, D., Duarte, P., Rodrigues, J., Costa, F. M., Monteiro, T., Martins, R., & Fortunato, E. (2014). Synthesis of Long ZnO Nanorods under Microwave Irradiation or Conventional Heating. The Journal of Physical Chemistry C, 118(26), 14629–14639. https://doi.org/10.1021/jp5027509.

[5] Caglar, Y., Gorgun, K., & Aksoy, S. (2015). Effect of deposition parameters on the structural properties of ZnO nanopowders prepared by microwave-assisted hydrothermal synthesis. Spectrochimica Acta Part A: Molecular and Biomolecular Spectroscopy, 138, 617–622. https://doi.org/10.1016/j.saa.2014.12.008.

[6] Liang, S., Zhu, L., Gai, G., Yao, Y., Huang, J., Ji, X., Zhou, X., Zhang, D., & Zhang, P. (2014). Synthesis of morphology-controlled ZnO microstructures via a microwave-assisted hydrothermal method and their gas-sensing property. Ultrasonics Sonochemistry, 21(4), 1335–1342. https://doi.org/10.1016/j.ultsonch.2014.02.007.

[7] Al-Gaashani, R., Radiman, S., Tabet, N., & Daud, A. R. (2011). Effect of microwave power on the morphology and optical property of zinc oxide nano-structures prepared

via a microwave-assisted aqueous solution method. Materials Chemistry and Physics, 125(3), 846–852. https://doi.org/10.1016/j.matchemphys.2010.09.038.

[8] Linganiso, E., Motaung, T., Linganiso, L., & Tetana, Z. (2020). One-step microwave hydrothermal synthesis of In_2O_3 nanostructures with high oxygen vacancy content. Materials Letters, 260, 126883. https://doi.org/10.1016/j.matlet.2019.126883.

[9] Singh, V. N., & Partheepan, G. (2013). Linear Sensing Response to Ethanol by Indium Oxide Nanoparticle Layers. Journal of Nanoscience, 2013, 1–4. https://doi.org/10.1155/2013/540741.

[10] Hussain, M. H., Abu Bakar, N. F., Mustapa, A. N., Low, K. F., Othman, N. H., & Adam, F. (2020). Synthesis of Various Size Gold Nanoparticles by Chemical Reduction Method with Different Solvent Polarity. Nanoscale Research Letters, 15(1). https://doi.org/10.1186/s11671-020-03370-5.

[11] Vaseem, M., Umar, A., Hahn, Y., Kim, D., Lee, K., Jang, J., & Lee, J. (2008). Flower-shaped CuO nanostructures: Structural, photocatalytic and XANES studies. Catalysis Communications, 10(1), 11–16. https://doi.org/10.1016/j.catcom.2008.07.022.

[12] Deville, G. (2012). La CEM en phase d'appel d'offres. Électronique. https://doi.org/10.51257/a-v1-e1308.

[13] Han, M. A., Kim, H. J., Lee, H. C., Park, J. S., & Lee, H. N. (2019). Effects of porosity and particle size on the gas sensing properties of SnO2 films. Applied Surface Science, 481, 133–137. https://doi.org/10.1016/j.apsusc.2019.03.043.

[14] Muniz, F. T. L., Miranda, M. A. R., Morilla Dos Santos, C., & Sasaki, J. M. (2016). The Scherrer equation and the dynamical theory of X-ray diffraction. Acta Crystallographica Section A Foundations and Advances, 72(3), 385–390. https://doi.org/10.1107/s205327331600365x.

[15] Mullica, D., Beall, G., Milligan, W., Korp, J., & Bernal, I. (1979). The crystal structure of cubic In(OH)3 by X-ray and neutron diffraction methods. Journal of Inorganic and Nu-clear Chemistry, 41(3), 277–282. https://doi.org/10.1016/0022-1902(79)80133-5.

[16] Zhang, X., Gu, R., Zhao, J., Jin, G., Zhao, M., & Xue, Y. (2015). Effects of Particle Size on the Gas Sensitivity and Catalytic Activity of In2O3. Journal of Materials Engineering and Performance, 24(10), 3815–3819. https://doi.org/10.1007/s11665-015-1698-4.

[17] Roberts, B. A., & Strauss, C. R. (2005). Toward Rapid, "Green", Predictable Microwave-AssistedSynthesis.ChemInform, 36(48). https://doi.org/10.1002/chin.200548249.

[18] Microwave-Assisted Organic Synthesis. (2007). Chemistry International Newsmagazine for IUPAC, 29(5). https://doi.org/10.1515/ci.2007.29.5.29a.

[19] Kappe, C. O., & Dallinger, D. (2005). The impact of microwave synthesis on drug dis-covery. Nature Reviews Drug Discovery, 5(1), 51–63. https://doi.org/10.1038/nrd1926.

[20] Krishnakumar, T., Jayaprakash, R., Pinna, N., Singh, V., Mehta, B., & Phani, A. (2009). Microwave-assisted synthesis and characterization of flower shaped zinc oxide nanostruc-tures. Materials Letters, 63(2), 242–245. https://doi.org/10.1016/j.matlet.2008.10.008.

[21] Das, S., Mukhopadhyay, A. K., Datta, S., & Basu, D. (2008). Prospects of microwave processing: An overview. Bulletin of Materials Science, 31(7), 943–956. https://doi.org/10.1007/s12034-008-0150-x.

[22] Zhou, S., Chen, M., Lu, Q., Zhang, Y., Zhang, J., Li, B., Wei, H., Hu, J., Wang, H., & Liu, Q. (2019). Ag Nanoparticles Sensitized In2O3 Nanograin for the Ultrasensitive

HCHO Detection at Room Temperature. Nanoscale Research Letters, 14(1). https://doi.org/10.1186/s11671-019-3213-6.

[23] Elilarassi, R., & Chandrasekaran, G. (2012). Influence of Co-doping on the structural, optical and magnetic properties of ZnO nanoparticles synthesized using auto-combustion method. Journal of Materials Science: Materials in Electronics, 24(1), 96–105. https://doi.org/10.1007/s10854-012-0893-4

[24] Pan, Q. Y., Cheng, Z. X., Wang, T. F., & Zhang, J. P. (2002). The nano-sized In2O3 powder synthesis by sol-gel method. Journal of Shanghai University (English Edition), 6(4), 353–357. https://doi.org/10.1007/s11741-002-0065-5

[25] Manafi, S., Tazikeh, S., & Joughehdoust, S. (2017). Synthesis and characterization of indium tin oxide nanoparticles via reflux method. Materials Science-Poland, 35(4), 799–805. https://doi.org/10.1515/msp-2018-0008

[26] Kumari, R., Sahai, A., & Goswami, N. (2015). Effect of nitrogen doping on structural and optical properties of ZnO nanoparticles. Progress in Natural Science: Materials Inter-national, 25(4), 300–309. https://doi.org/10.1016/j.pnsc.2015.08.003

[27] Zhuang, Z., Peng, Q., Liu, J., Wang, X., & Li, Y. (2007). Indium Hydroxides, Oxyhy-droxides, and Oxides Nanocrystals Series. Inorganic Chemistry, 46(13), 5179–5187. https://doi.org/10.1021/ic061999f

[28] Zhang, J., Gao, L., & Chen, M. (2007). A novel solvothermal method to synthesize one-dimensional chains of indium tin oxide nanoparticles. Materials Letters, 61(13), 2671–2674. https://doi.org/10.1016/j.matlet.2006.10.020

[29] Zaleta-Alejandre, E., Camargo-Martinez, J., Ramirez-Garibo, A., Pérez-Arrieta, M., Balderas-Xicohténcatl, R., Rivera-Alvarez, Z., Aguilar-Frutis, M., & Falcony, C. (2012). Structural, electrical and optical properties of indium chloride doped ZnO films

synthe-sized by Ultrasonic Spray Pyrolysis technique. Thin Solid Films, 524, 44–49. https://doi.org/10.1016/j.tsf.2012.09.050

[30] Avivi, S., Mastai, Y., & Gedanken, A. (2010). ChemInform Abstract: Sonohydroly-sis of In3+ Ions: Formation of Needlelike Particles of Indium Hydroxide. ChemInform, 31(34), no. https://doi.org/10.1002/chin.200034232

[31] Zhang, K., Qin, S., Tang, P., Feng, Y., & Li, D. (2020). Ultra-sensitive ethanol gas sen-sors based on nanosheet-assembled hierarchical ZnO-In2O3 heterostructures. Jour-nal of Hazardous Materials, 391, 122191. https://doi.org/10.1016/j.jhaz-mat.2020.122191

[32] Beena, D., Lethy, K., Vinodkumar, R., Mahadevan Pillai, V., Ganesan, V., Phase, D., & Sudheer, S. (2009). Effect of substrate temperature on structural, optical and electrical properties of pulsed laser ablated nanostructured indium oxide films. Applied Surface Sci-ence, 255(20), 8334–8342. https://doi.org/10.1016/j.apsusc.2009.05.057

[33] Fan, J. C. C., & Goodenough, J. B. (1977). X-ray photoemission spectroscopy stud-ies of Sn-doped indium-oxide films. Journal of Applied Physics, 48(8), 3524–3531. https://doi.org/10.1063/1.324149

[34] Wu, W. F., & Chiou, B. S. (1996). Optical and mechanical properties of reactively sput-tered silicon dioxide films. Semiconductor Science and Technology, 11(9), 1317–1321. https://doi.org/10.1088/0268-1242/11/9/012

[35] Valaski, R., Lessmann, R., Roman, L. S., Hümmelgen, I. A., Mello, R. M., & Micaroni, L. (2004). Poly (3-methylthiophene)-based photovoltaic devices prepared onto tin-oxide/sulfonated-polyaniline electrodes. Electrochemistry Communications, 6(4), 357–360. https://doi.org/10.1016/j.elecom.2004.02.001

[36] Zakaria, Z., Halim, N. F. A., Schleusingen, M. H. V., Islam, A. K. M. S., Hashim, U., & Ahmad, M. N. (2015). Effect of Hydrochloric Acid Concentration on Morphology of Pol-yaniline Nanofibers Synthesized by Rapid Mixing Polymerization. Journal of Nanomateri-als, 2015, 1–6. https://doi.org/10.1155/2015/218204

[37] Zhong, W., Deng, J., Yang, Y., & Yang, W. (2005). Synthesis of Large-Area Three-Dimensional Polyaniline Nanowire Networks Using a Soft Template. Macromolecular Rapid Communications, 26(5), 395–400. https://doi.org/10.1002/marc.200400463

[38] Nimbekar, A. A., Bhatia, P. G., & Deshmukh, R. R. (2021). Ammonia sensors manufac-tured by plasma enhanced grafting of conducting polymers on nylon-6 fabrics. Synthetic Metals, 279, 116840. https://doi.org/10.1016/j.synthmet.2021.116840

[39] Stenger-Smith, J. D. (1998). Intrinsically electrically conducting polymers. Synthesis, characterization, and their applications. Progress in Polymer Science, 23(1), 57–79. https://doi.org/10.1016/s0079-6700(97)00024-5

[40] Bakker, E., & Telting-Diaz, M. (2002). Electrochemical Sensors. Analytical Chemistry, 74(12), 2781–2800. https://doi.org/10.1021/ac0202278

[41] Stetter, J. R., & Li, J. (2008). Amperometric Gas SensorsA Review. Chemical Reviews, 108(2), 352–366. https://doi.org/10.1021/cr0681039

[42] Huang, J., Virji, S., Weiller, B. H., & Kaner, R. B. (2002). Polyaniline Nanofibers: Fac-ile Synthesis and Chemical Sensors. Journal of the American Chemical Society, 125(2), 314–315. https://doi.org/10.1021/ja028371y

[43] Ajpi, C., Leiva, N., Vargas, M., Lundblad, A., Lindbergh, G., & Cabrera, S. (2020). Synthesis and Characterization of LiFePO4–PANI Hybrid Material as Cathode for Lithi-um-Ion Batteries. Materials, 13(12), 2834. https://doi.org/10.3390/ma13122834

[44] Li, M., Guo, Y., Wei, Y., Macdiarmid, A., & Lelkes, P. (2006). Electrospinning polyaniline-contained gelatin nanofibers for tissue engineering applications. Biomaterials, 27(13), 2705–2715. https://doi.org/10.1016/j.biomaterials.2005.11.037

[45] Armes, S., & Miller, J. (1988). Optimum reaction conditions for the polymerization of aniline in aqueous solution by ammonium persulphate. Synthetic Metals, 22(4), 385–393. https://doi.org/10.1016/0379-6779(88)90109-9

[46] Abdiryim, T., Xiao-Gang, Z., & Jamal, R. (2005). Comparative studies of solid-state synthesized polyaniline doped with inorganic acids. Materials Chemistry and Physics, 90(2–3), 367–372. https://doi.org/10.1016/j.matchemphys.2004.10.036

[47] Lenin, R., Singh, A., & Bera, C. (2021). Effect of dopants and morphology on the electrical properties of polyaniline for various applications. Journal of Materials Science: Materials in Electronics, 32(20), 24710–24725. https://doi.org/10.1007/s10854-021-06883-6

[48] Saravanan, S., Joseph Mathai, C., Anantharaman, M., Venkatachalam, S., & Prabhakaran, P. (2006). Investigations on the electrical and structural properties of polyaniline doped with camphor sulphonic acid. Journal of Physics and Chemistry of Solids, 67(7), 1496–1501. https://doi.org/10.1016/j.jpcs.2006.01.100

[49] Rahy, A., & Yang, D. J. (2008). Synthesis of highly conductive polyaniline nanofibers. Materials Letters, 62(28), 4311–4314. https://doi.org/10.1016/j.matlet.2008.06.057

[50] Zhang, J., Shi, C., Ji, T., Wu, G., & Kou, K. (2014). Preparation and Microwave Absorbing Characteristics of Multi-Walled Carbon Nanotube/Chiral-Polyaniline Composites. Open Journal of Polymer Chemistry, 04(03), 62–72. https://doi.org/10.4236/ojpchem.2014.43008

[51] Zhang, X., Zhang, J., & Liu, Z. (2004). Tubular composite of doped polyaniline with multi-walled carbon nanotubes. Applied Physics A, 80(8), 1813–1817. https://doi.org/10.1007/s00339-003-2491-z

[52] Pouget, J. P., Jozefowicz, M. E., Epstein, A. J., Tang, X., & MacDiarmid, A. G. (1991). X-ray structure of polyaniline. Macromolecules, 24(3), 779–789. https://doi.org/10.1021/ma00003a022

[53] Patil, R., Harima, Y., Yamashita, K., Komaguchi, K., Itagaki, Y., & Shiotani, M. (2002). Charge carriers in polyaniline film: a correlation between mobility and in-situ ESR meas-urements. Journal of Electroanalytical Chemistry, 518(1), 13–19. https://doi.org/10.1016/s0022-0728(01)00689-1

[54] Diggikar, R. S., Deshmukh, S. P., Thopate, T. S., & Kshirsagar, S. R. (2019). Performance of Polyaniline Nanofibers (PANI NFs) as PANI NFs-Silver (Ag) Nanocomposites (NCs) for Energy Storage and Antibacterial Applications. ACS Omega, 4(3), 5741–5749. https://doi.org/10.1021/acsomega.8b02834

[55] Electronic properties of conjugated polymers. (1985). Philosophical Transactions of the Royal Society of London. Series A, Mathematical and Physical Sciences, 314(1528), 37–49. https://doi.org/10.1098/rsta.1985.0006

[56] Ismail, M., Ibrahim, M., & Abd El-Ghaffar, M. (1998). Polyaniline as an antioxidant and antirad in SBR vulcanizates. Polymer Degradation and Stability, 62(2), 337–341. https://doi.org/10.1016/s0141-3910(98)00016-0

[57] Long, D. A. (2004). Infrared and Raman characteristic group frequencies. Tables and chartsGeorge Socrates John Wiley and Sons, Ltd, Chichester, Third Edition, 2001. Price £135. Journal of Raman Spectroscopy, 35(10), 905. https://doi.org/10.1002/jrs.1238

[58] Porramezan, M., & Eisazadeh, H. (2011). Fabrication and characterization of polyaniline nanocomposite modified with Ag2O nanoparticles. Composites Part B: Engineering, 42(7), 1980–1986. https://doi.org/10.1016/j.compositesb.2011.05.029

[59] Gaylord, N. G., & Gaylord, N. G. (1962). Infrared Spectroscopy. Its Use as an Analyti-cal Tool in the Field of Paints and Coatings. Infrared Spectroscopy Committee of the Chi-cago Society for Paint Technology, 1350 South Kostner Avenue, Chicago 23, Illinois. Federation of Societies for Paint Technology, Philadelphia 7, pa. 160 pp. Journal of Applied Polymer Science, 6(23), S38. https://doi.org/10.1002/app.1962.07006232

[60] Stejskal, J., & Gilbert, R. G. (2002). Polyaniline. Preparation of a conducting polymer (IUPAC Technical Report). Pure and Applied Chemistry, 74(5), 857–867. https://doi.org/10.1351/pac200274050857

[61] Shukla, S., Bharadvaja, A., Tiwari, A., Parashar, G., & Dubey, G. (2010). Synthesis and Characterization of Highly Crystalline Polyaniline Film Promising For Humid Sensor. Advanced Materials Letters, 1(2), 129–134. https://doi.org/10.5185/amlett.2010.3105

[62] Kotresh, S., Ravikiran, Y. T., Vijaya Kumari, S. C., Ramana, C. V. V., Anu, A. S., & Ba-too, K. M. (2017). Optimised polyaniline–cadmium ferrite nanocomposite: synthesis, characterisation and alternating current response. Polymer Bulletin, 75(6), 2475–2490. https://doi.org/10.1007/s00289-017-2169-x

[63] Marjanović, B., Juranić, I., Ćirić-Marjanović, G., Pašti, I., Trchová, M., & Holler, P. (2011). Chemical oxidative polymerization of benzocaine. Reactive and Functional Poly-mers, 71(7), 704–712. https://doi.org/10.1016/j.reactfunctpolym.2011.03.013

[64] Guo, Y., He, D., Xia, S., Xie, X., Gao, X., & Zhang, Q. (2012). Preparation of a Novel Nanocomposite of Polyaniline Core Decorated with Anatase-TiO2Nanoparticles

in Ionic Liquid/Water Microemulsion. Journal of Nanomaterials, 2012, 1–7. https://doi.org/10.1155/2012/202794

[65] Rahman, S. U., Röse, P., Surati, M., Shah, A. U. H. A., Krewer, U., & Bilal, S. (2020). 3D Polyaniline Nanofibers Anchored on Carbon Paper for High-Performance and Light-Weight Supercapacitors. Polymers, 12(11), 2705. https://doi.org/10.3390/polym12112705

[66] Geethalakshmi, D., Muthukumarasamy, N., & Balasundaraprabhu, R. (2014). Effect of dopant concentration on the properties of HCl-doped PANI thin films prepared at different temperatures. Optik, 125(3), 1307–1310. https://doi.org/10.1016/j.ijleo.2013.08.014

[67] S., Brédas, J. L., Epstein, A. J., Woo, H. S., Tanner, D. B., Huang, W. S., & Mac-Diarmid, A. G. (1987). Polaron lattice in highly conducting polyaniline: Theoretical and optical studies. Physical Review Letters, 59(13), 1464–1467. https://doi.org/10.1103/physrevlett.59.1464

CHAPTER 4

SYNTHESIS AND CHARACTERIZATION OF ONION-LIKE CARBON

4.1 Introduction

OLCs (Onion-like carbon) are fullerenes composed of several layers that may take on a circular or noncircular shape. They are made up of multiple layers of sp^2 graphene sheets. They were given this name because the sheets are organized in an onion-like arrangement, which gives them their appearance [1]. OLCs are also known by a variety of other names, including "carbon onions," "multi-shelled fullerenes," "Bucky-onions," and "onion-like carbons," among others [2]. They typically have a diameter of between 2 and 200 nm, depending on the synthesis procedure and the conditions under which they are formed. A broad number of applications have benefited from the extraordinary features of carbon nano onions, which have prompted significant research interest in this area. OLCs exhibit remarkable electrical and structural properties as compared to other materials, such as the capacity to receive electrons transiently, a high specific surface area ratio, and broad absorbance bands (extended pi-system) [3].

OLCs are used in some broad applications because of their unique physical and chemical properties including electronics, optical limiting, catalysis, conversion and storage of energy, hyper lubricants, sensors, and applications in biology and the environment. Conductivity is one of the most fascinating physical properties of OLCs [4]. There are numerous methods for the production of OLCs and the most popular methods include thermal annealing of nano-diamonds (NDs), water submerged graphite electrodes in the arc-discharge process [5], flame synthesis or pyrolysis [6], CVD (chemical vapour deposition) [7], ion injection [8], and electron beam irradiation [9]. A variety of onion shapes and sizes are available, including miniature, medium, big, spherical, polyhedral, thickly cored, hollow cored, and hollow, thinly cored onions.

Even though some of these technologies can produce high-quality OLCs, creating OLCs on gram scales requires a series of complex operations. Transition metals may be used as catalysts in CCVD (catalytic chemical vapour deposition) for example. While high purity products may

be produced with this method, it is a costly technique because of the cost of the metallic catalyst(s) [10]. It is also necessary to use strong acids (like nitric acid) to remove the leftover metal catalyst nanoparticles from the as-synthesized OLCs [11]. A suction setup working at temperatures over 1000 °C is required for the thermal annealing of nano-diamonds to create higher quantities of OLCs [12].

Owing to the shortcomings of the aforementioned methodologies, researchers have examined the use of different carbon precursors to produce OLCs without or with fewer hurdles. Among the natural carbon sources that Ahmed et al. used were carrots and tomatoes [13]. In a previous study, OLCs were used in supercapacitor by Mohapatra et al. [14]. Essential oil-derived OLCs for photocatalytic studies were also reported by Tripathi et al. [15]. To manufacture more OLCs, the use of these precursors may be classified as a metal catalyst-free synthesis strategy, which is less expensive and less difficult to execute. Since they are less prone to contamination and production expenses, they offer an advantage over other procedures such as arc discharge and thermal annealing methods [16].

In this study, OLCs were synthesized utilizing a simple traditional flame synthesis technique (FP), which enables continual OLC creation in the air with minimal complications. This pyrolysis method uses petroleum products (e.g., ghee oil, flaxseed oil, paraffin oil, candle wax, etc.) to produce a large amount of OLCs on a gram scale. The synthesized OLCs will further be utilized (chapter 6) for gas sensing applications at room temperatures due to benefits such as simplicity of functionalization, the ease of surface modification with polymers, and the high density of active sites that make them ideal for gas sensing [17].

The structural morphologies of OLCs created using this method are similar to those of an onion, with circular multi-layers and a spherical architecture. Analysis of the prepared OLCs made use of XRD (X-ray diffraction), SEM (scanning electron microscope), TEM (transmission electron microscope), FTIR (Fourier Transform Infrared spectroscopy), UV-Vis (ultraviolet-visible spectroscopy), TGA/DTA (thermogravimetric Analysis and differential Thermal Analysis) and Raman spectroscopy.

4.2 Procedure for conducting experiments

4.2.1 Reagents

Ethanol used in this study was bought from MK Chemicals (South Africa). OLCs were obtained using candlesticks (Rite brand) purchased from Shoprite Supermarket in Johannesburg, South Africa. A polished brass collecting plate (BCP, 140x140x1.5 mm) and a metal stand (refer to Figure 4.1) were made in the physical sciences workshop at the University of the Witwatersrand.

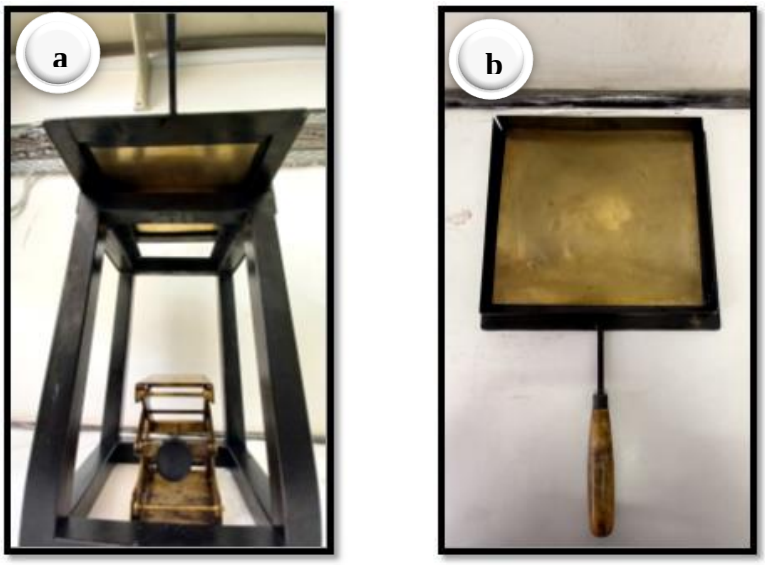


Figure 4.1 Photographs of (a) metal stand and (b) brass collecting

4.2.2 Synthesis of OLCs using candlesticks

For this study, OLCs were synthesized using a fairly simple approach (Figure 4.2) [18]. The OLCs were gathered by burning candlesticks with a polished brass collection plate placed on the surface of candle flame of the candle for 6 hours to collect the OLCs generated on the surface. After collecting enough material, OLCs were scraped from the brass collection plate with a clean spatula, refined in ethanol using a centrifuge, and stored in a vial after drying at 60 °C for 2 hrs.

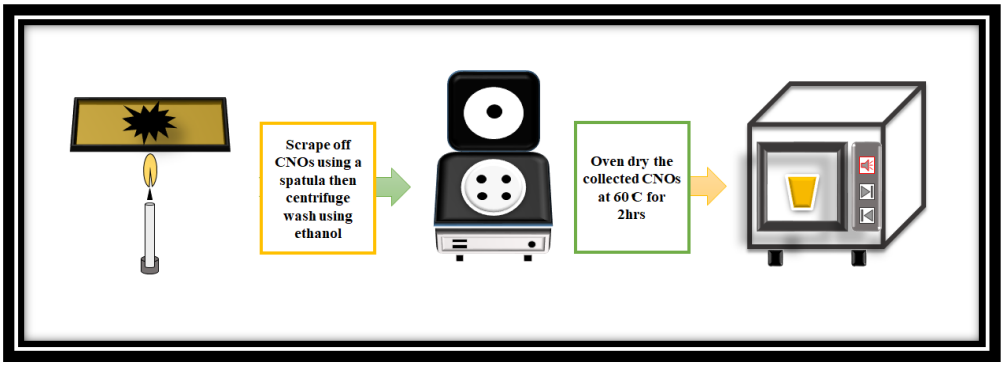


Figure 4.2 Graphical illustration of OLCs synthesis via flame pyrolysis method

4.2.3 Characterization techniques

A Bruker Tensor 27 Fourier Transform Infrared spectrometer was used for the FTIR spectroscopy analysis. After dispersing the samples in ethanol, dropping them on a carbon tape, and coating them with a layer (10 nm) of gold-palladium and a layer (10 nm) of carbon, SEM examination was done at 20 kV on a ZEISS SIGMA 03–39 FESEM. The materials were disseminated in ethanol by ultrasonication and then put onto a lace carbon copper grid for TEM examination using a Tecnai Spirit T12 at 120 kV. ImageJ analysis software was used to determine the particle sizes of TEM OLCs. The thermal analysis was performed on a Perkin Elmer TGA 6000 thermogravimetric analyser with high-purity nitrogen and air at a heating rate of 10 C/min and a gas flow rate of 10 mL/min. PXRD data were gathered using Cu radiation on a Bruker D2 Phaser. The surface area and pore volume were determined using a Micromeritics Tristar 3000 surface area and porosity analyser. A Bruker Raman Senterra spectrometer with a 514 nm excitation laser was used to make Raman spectroscopy observations.

4.3 Discussion of the findings

4.3.1 XRD

The XRD technique was utilized to identify and characterize the polycrystalline phase presented by the synthesized OLCs. By employing this approach, we were able to study the crystallinity and/or polycrystallinity of OLCs by examining the atomic arrangements acquired from X-ray diffraction. The diffractogram in Figure 4.3 demonstrates that the OLCs were predominantly constituted of polycrystalline carbon atom configurations free of extraneous impurities. OLCs patterns revealed carbon peaks at 25 ˚ and 43.5 ˚, correlating to carbon planes (002) and (004), respectively, confirming that the material is a polycrystalline carbon nanomaterial. The presence of a peak centred on 43.5 ˚, on the other hand, indicates that the OLCs generated include graphitic carbon domains [19].

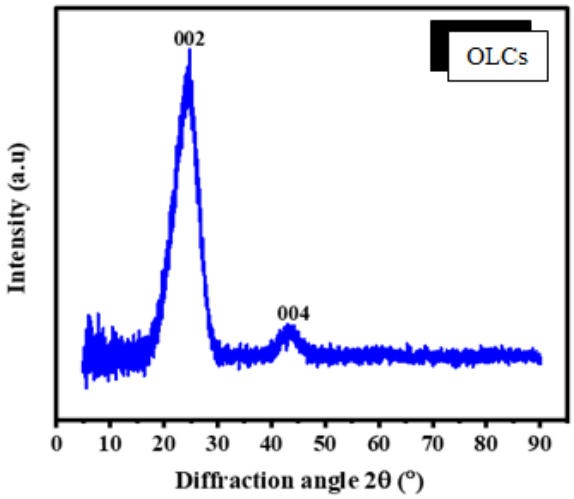


Figure 4.3 XRD profile of OLCs synthesized from candlesticks

4.3.2 TEM

The TEM images of OLCs nanoparticles are shown in Figure 4.4. These images show a spherical morphology Figure 4.4 (a). Figure 4.4 (b) indicates that these spheres are made up of layers, confirming the onion-like nature of the structure. The synthesized material contains nanoparticles that aggregate to create bigger conglomerates. As indicated in figure 4.4 (c) by the red arrows, the OLCs overlap to produce chain-like quasi-spheres, as a result, a solitary nanoparticle is rarely detected in the microscopy data The nanoparticles were discovered to have an average diameter of 38 ± 9 nm (figure 4.4 (d)). Although the synthesized OLCs are multi-layered, determining the number of shells was difficult.

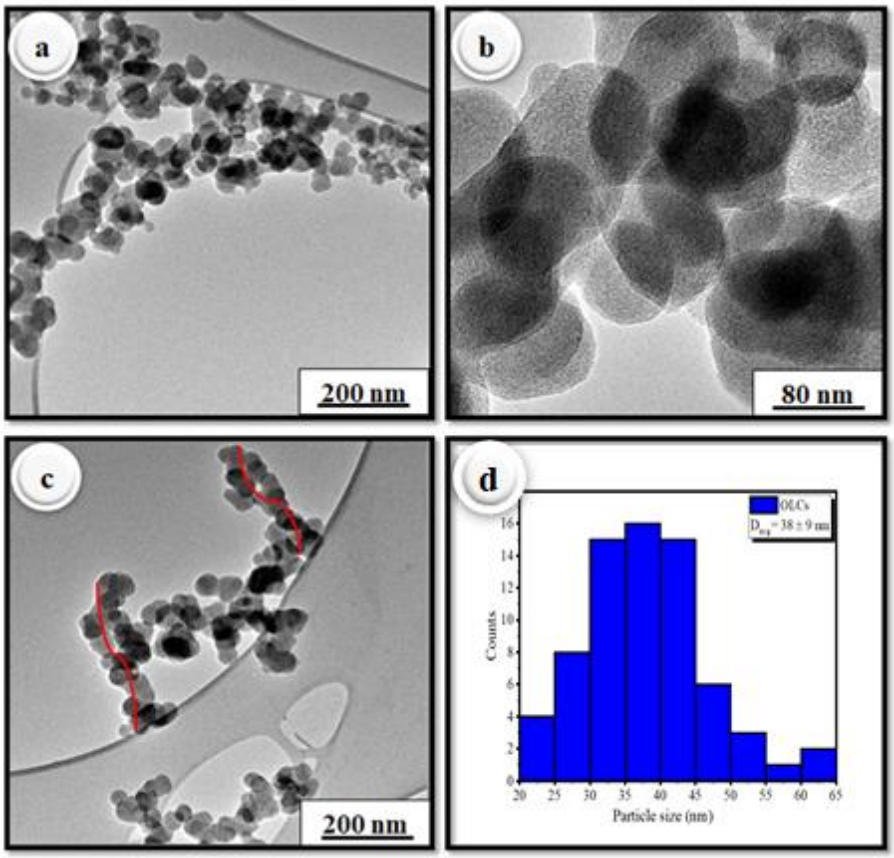


Figure 4.4 TEM micrograph, (a) NPs, (b) Multi layers, (c) Chain-like connection and (d) particle size distribution of OLCs

4.3.3 SEM

SEM was used to analyse the architecture of generated OLCs. The SEM images of OLCs are shown in Figure (4.5 (a & b). These images demonstrate the spherical shape of OLCs with average size of ~ 38 nm. The TEM study of OLCs, as shown in figure 4.4, corroborates with the SEM findings.

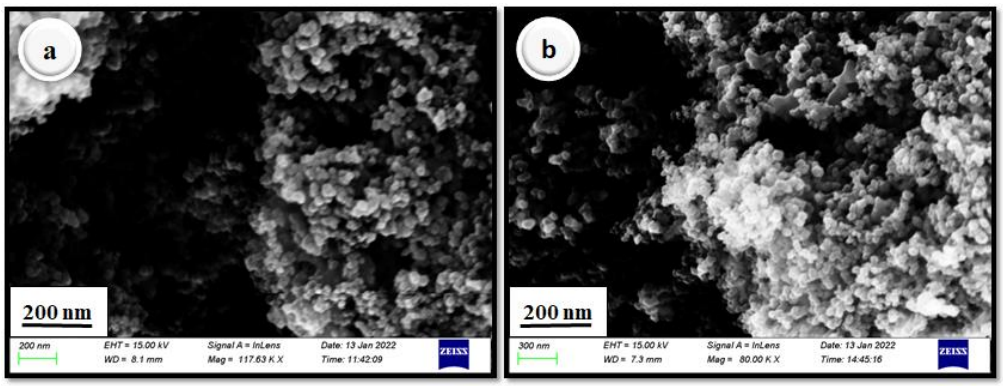


Figure 4.5 SEM micrographs of OLCs

4.3.4 BET

The surface area, pore size, and pore volume of the OLCs were determined using the BET technique. In nitrogen adsorption and desorption environments (Table 4.1 and Figure 4.6). The pore diameter was ~19.3 nm and the BET surface area was 85, 7 m^2/g, indicating that the material is mesoporous. OLCs have an adsorption-desorption isotherm that is a type I (Figure 4.6 (a)). According to Mongwe et al., the precursors utilized throughout the synthesis process have a significant impact on the BET surface characteristics of OLCs (surface area and pore size) [20]. Figure 4.6 (b) depicts the pore size distribution curve of OLCs, which have mostly mesoporous structures with pores ranging in diameter from 2 to 50 nm.

Table 4.1 BET surface area, pore size and pore volume distribution of OLCs

Measurements	OLCs
Surface area (m^2g^{-1})	85.7
Pore size (nm)	19.3
Pore volume (cm^3g^{-1})	0.38

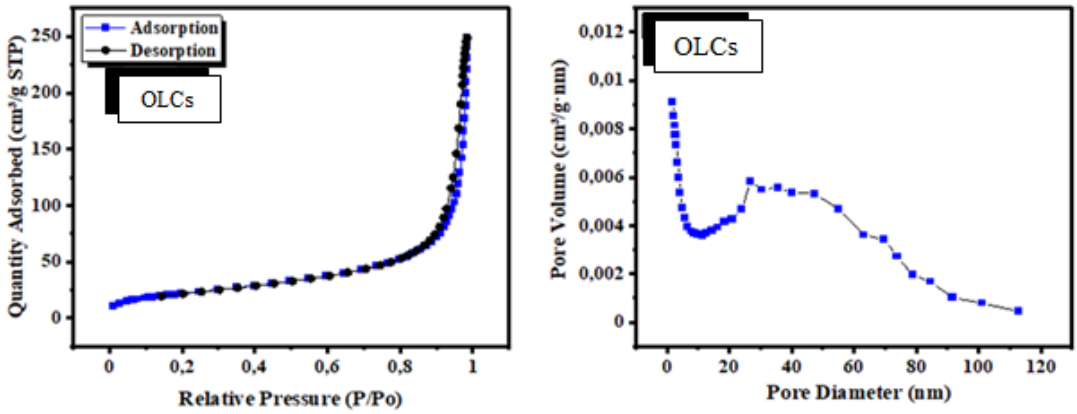


Figure 4.6 (a) BET isotherm curve and (b) Pore size distribution curve of OLCs

4.3.5 FT-IR

Figure 4.7 depicts the FTIR spectrum of the OLCs which exhibits graphitic carbon peaks. The doublet at ~2929 cm^{-1}, as well as the peaks at 2159-2112 cm^{-1}, suggest C-H unsymmetrical and symmetric stretching vibration modes and C-C stretching vibration modes respectively (see Table 4.2). These findings support the hypothesis that the sample is made of hy-

drocarbon-based compounds [22]. A strong peak arises about 2549 cm^{-1}; this peak can be attributed to carbon dioxide (CO_2), which is one of the pyrolysis (i.e. combustion) products trapped by the OLCs [23]. Additionally, other functional groups with selective peaks, such as C=C and C-C, appear at 1973 cm^{-1} and 938 cm^{-1}, respectively, as a result of bending or distortion vibration modes. [24 & 25].

Table 4.2 Assignments FTIR bands of OLCs

Wavenumber	Functional groups
2929	v(C-H)
2549	CO_2
2159-2112	v(C-C)
1973	C=C
938	C-C

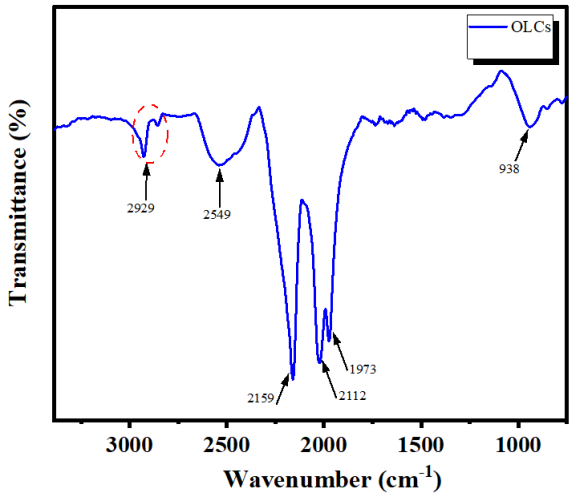


Figure 4.7 FTIR spectrum of OLCs

4.3.6 Raman spectroscopy

The Raman spectra of OLCs is depicted in Figure 4.8. The spectra were excited at 514 nm. Raman spectroscopy calculates the quantity of the order in a material by analysing the proportion of sp^2 to sp^3 carbon atoms, which is related to the intensity and shape of the D and G bands [26]. The most distinct signals, located at approximately 1337cm^{-1} and 1592 cm^{-1}, are referred to as the D band and G band, correspondingly. The G band is linked with the E_{2g} mode of sp^2 hybridized carbons, while the D band is linked with the breathing mode of the sp^2 carbon rings,

which is activated by defects in the fullerene network caused by the presence of oxygen-rich functional groups, as well as an increase in the sp^3 hybridized carbons as a result of the increasing disorder caused by covalent functionalization [27].

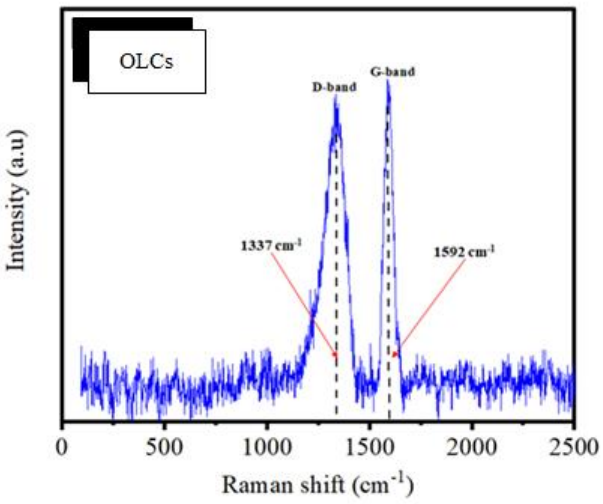


Figure 4.8 Raman spectrum of OLCs

4.3.7 Thermal stability

Figure 4.9 illustrates the Thermogravimetric Analysis (TGA) and Differential Thermogravimetric (DTA) curves of OLCs in air. The TGA curve demonstrates that the OLCs decompose completely (zero percent sample residue) through the heat combustion process, as illustrated in figure 4.9 (a). As a result, the TGA profiles observed imply that the materials undergo fast oxidative decomposition [28]. Figure 4.9 (b) depicts the first-order derivative weight loss curve for OLCs. The first-order derivative weight loss (FDW) graph indicates that the decomposition peak occurs around 667 degrees Celsius, the rapid mass-loss shift associated with OLC burning demonstrates that the material is a homogenous single phase with minimal impurities [28].

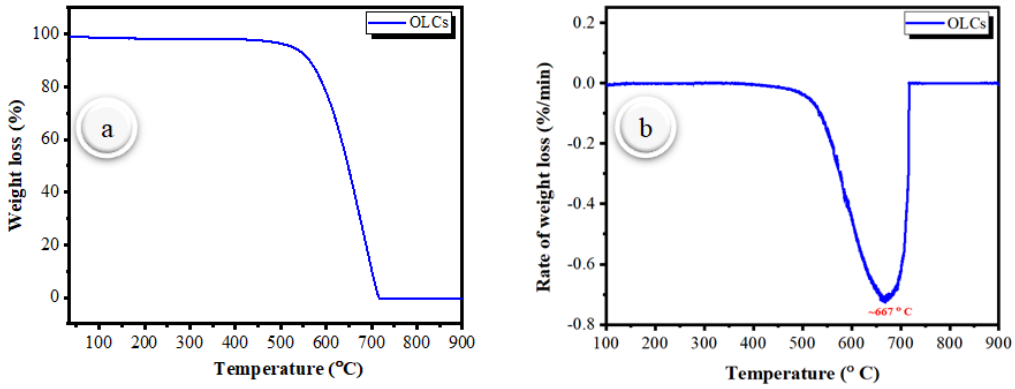


Figure 4.9 Thermographic profile (a) and (b) first derivative weight loss curve of OLCs

4.4 Conclusion

OLCs that have been produced are mostly observed as quasi-spherical nanoparticles with an average diameter of 38±9 nm and circular multi-layers. The OLCs were primarily polycrystalline and clean of unwanted impurities, according to XRD analysis. FT-IR analysis demonstrated that OLCs were successfully synthesized, with multiple peaks of interest. SEM showed that the synthesized OLCs are spherical in agreement with the TEM data. The BET surface area, pore size, and pore volume were determined to be 85.7 m^2g^{-1}, 19.3 nm, and 0.38 cm^3g^{-1}, respectively. According to the literature, the features of OLCs such as surface area and pore volume are dependent on the type of precursor utilized. TGA analysis revealed that OLCs completely decompose following heat treatment and that the decomposition occurred at around 667 degrees Celsius. Raman spectroscopy revealed a D-band (1337 cm^{-1}) and G-band (1592 cm^{-1}) that are both characteristics of OLCs.

4.5 References

[1] Fu-Dong, H., Yao, Bin, Y., & Yu-Jun, B.(2011) .Preparation of Carbon Nano-Onions and Their Application as Anode Materials for Rechargeable Lithium-Ion Batteries," Physical chemistry,.115(18), pp. 8923-8927.

[2] Wang,Y et al .(2011).Carbon dots of different composition and surface functionalization: cytotoxicity issues relevant to fluorescence cell imaging. Experimental biology and medicine, .236(11), pp. 1231-1238.

[3] Neil J. Coville,J.N., Mhlanga, S.D., Nxumalo, E.N., & Shaikjee, A.(2011).A review of shaped carbon nanomaterials," South African journal of science,.107(3-4), p.p 15.

[4] Guldi,D.M., & Martin,N.(2002).Fullerene architectures made to order; biomimetic motifs — design and features.Material chemistry,12, pp. 1959-1963.

[5] Borgohain,R., Yang,J., John P. Selegue,J.P., Kim,D.Y.(2014).Controlled synthesis, efficient purification, and electrochemical characterization of arc-discharge carbon nano-onions. 66, pp. 272-284.

[6] Palkar A et al. (2007).Reactivity Differences between Carbon Nano Onions (CNOs) Prepared by Different Methods.An Asian journa. 2, pp. 625-633.

[7] Carrasco J.A et al. (2016) .CVD synthesis of carbon spheres using NiFe-LDHs as catalytic precursors: structural, electrochemical and magnetoresistive properties.Material chemistry.4, pp. 440-448.

[8] Heer, W.A., & Ugarte, D. (1993). Carbon onions produced by heat treatment of carbon soot and their relation to the 217.5 nm interstellar absorption feature. Chemical Physics Letters, 207, 480-486.

[9] Ugarte, D. (1992).Curling and closure of graphitic networks under electron-beam irradiation. Nature 359, 707–709. https://doi.org/10.1038/359707a0

[10] Street, K., Marchetti, M., Vander Wal, R. et al. (2004).Evaluation of the Tribological behavior of Nano-Onions in Krytox 143AB. Tribology Letters 16, 143–149. https://doi.org/10.1023/B:TRIL.0000009724.01711.f4

[11] Rotundi, A., Rietmeijer, F.J.M., Borg, J. (2006). Natural C60 and Large Fullerenes: A Matter of Detection and Astrophysical Implications. In: Natural Fullerenes and Related Structures of Elemental Carbon. Developments in Fullerene Science, vol 6. Springer, Dordrecht. https://doi.org/10.1007/1-4020-4135-7_5

[12] Cabioc'h,T.H., Thune,E., & Jaouen,M.(2002).Mechanisms involved in the formation of onion-like carbon nanostructures synthesized by ion implantation at high temperature," Physics review.65(13), pp. 1-3.

[13] Dr. Yang,T et al.(2014).Hydrogen Abstraction/Acetylene Addition Revealed.53(30), pp. 7740-7744. https://doi.org/10.1002/anie.201607509 (Accessed August 2021)

[14] Mohapatra,D., Badrayyana,S., & Parida,S. (2016) .Facile wick-and-oil flame synthesis of high-quality hydrophilic onion-like carbon nanoparticles," Material chemistry and physics , .176, pp. 112-119.

[15] Tripathi,K.M et al.(2017).Green Fluorescent Onion-Like Carbon Nanoparticles from Flaxseed Oil for Visible Light-Induced Photocatalytic Applications and Label-Free Detection of Al(III) Ions, ACS Sustainable chemistry & engineering.5(5), pp. 3982-3992.

[16] Dhurvey, Y.R., Kawtikwar, P.S., & Sakarkar D.M. (2012).Evaluation of physicochemical properties of cow ghee before and after hydrogenation. Int.J.ChemTech Res.4 (1), pp. 185-189.

[17] Okechukwu,V,O.,Mavumengwana,V., Ivo A. Hümmelgen,A.I., & A.M, Ma-mo.(2019).Concomitant in Situ FTIR and Impedance Measurements to Address the 2-Methylcyclopentanone Vapor-Sensing Mechanism in MnO2–Polymer Nanocomposites," ASC Omega, 4(5), pp. 8324-8333.

[18] Raghu, A.V., Karuppanan,K.K., & Pullithadathil,B.(2019).Highly Surface Active Phosphorus-Doped Onion-Like Carbon Nanostructures: Ultrasensitive, Fully Reversible, and Portable NH3 Gas Sensors. ACS Applied electronic matrials.1 (11), pp. 2208-2219.

[19] Mongwe,T.H et al. (2018).Synthesis of chain-like carbon nano-onions by a flame assisted pyrolysis technique using different collecting plates Diamond and Related Materials.Diamond related materials,90, pp. 135-143.

[20] Zeiger,M et al.(2016).Influence of carbon substrate on the electrochemical performance of carbon/manganese oxide hybrids in aqueous and organic electrolytes," RSC Advances. 6(109).

[21] Dr. Martha E et al. (2011).Electrochemical properties of oxidized carbon nano-onions: DRIFTS-FTIR and Raman spectroscopic analyses," A European journal of chemical physical chemistry.12 (14), pp. 2659-2668.

[22] Osswald, S., Havel,M.,& Gogotsi,Y.(2007).Monitoring oxidation of multiwalled carbon nanotubes by Raman spectroscopy.Journal of Raman Spectroscopy.38(6), pp. 728-736.

[23] Tovar,C.D et al.(2019).Preparation of Chitosan/Poly (Vinyl Alcohol) Nanocomposite Films Incorporated with Oxidized Carbon Nano-Onions (Multi-Layer Fullerenes) for Tissue-Engineering Applications," Biomolecules.9(11), pp. 684.

[24] Galli, G., Gygi,F., & Golaz,J.C.(1998).Vibrational and electronic properties of neutral and negatively charged C20 clusters. Phys.RevB.57 (3), pp. 1860-1867.

[25] Shamsudin,M.S., & Sanip,S.M.(2015).A Review on Graphene Evidenced by Raman Spectroscopy, Advanced materials research.1109, pp. 509-513.

[26] Iijima S et al. (1999).Nano-aggregates of single-walled graphitic carbon nano-horns," Chemistry physics letter.309 (3-4), pp. 165-170.

[27] Boi,S.F et al.(2017).UV absorption investigation of ferromagnetically filled ultra-thick carbon onions, carriers of the 217.5 nm Interstellar Absorption Feature"," Applied physics , pp. 122-224.

CHAPTER 5

SYNTHESIS AND CHARACTERIZATION OF PANI/In_2O_3/OLCs COMPOSITE FOR ROOM TEMPERATURE GAS SENSING APPLICATION

5.1 Introduction

Ammonia (NH_3) is a poisonous chemical that is used in technical installation operations and is commonly used in biological processes (cooling systems, chemical industry, and automotive industry). The American Conference of Industrial Hygienists has set limits of 25 ppm for long-term (8-hrs) exposure and 35 ppm for short-term (15-minute) exposure to NH_3 [1]. In medicine, NH_3 levels in the breath between 2500 and 5000 parts per billion (ppb) are linked to organ malfunction and diabetes [2]. As a result, developing new methodologies and sensors that can identify minor ammonia concentrations accurately and quickly is very desirable. High sensitivity, increased selectivity, fast response time, reproducibility, high reliability, reduced energy consumption, low cost, safety, and broad range of measurement at varied operation temperatures, are all required for such sensors [3].

Consequently, portable and low-cost, solid-state chemiresistive-type gas sensors seem to be one of the effective options for gas detection. An elevated operating temperature of 200 to 400 °C is required for typical metal oxide semiconductors with broad energy band gaps, which necessitates a high power supply and hence limits their widespread use [4]. Elevating the working temperature is an effective method for overcoming the material's high activation energy and so improving the gas detecting performance of chemiresistive-type sensors [5]. When compared to a sensor functioning at room temperature, a thermally enhanced sensor is more extensively employed. For inflammable and explosive gas detection, the thermal-activated approach, on the other hand, poses too many risks [6]. In addition, raising the working temperature may impair the gas sensors' appropriateness and dependability, as has been previously noted [7].

Incorporating n-type metal oxide semiconductors, such as In_2O_3, SnO_2, CeO_2, and $CoFe_2O_4$, into carbon-based materials and CPs (conducting polymers) may increase the sensing capabilities of manufactured nanocomposites [8]. Carbon materials such as OLCs have been identified as possible candidates for gas sensing at room temperature [9]. Particularly, the wide surface

area, ballistic charge transport, and low noise properties of carbon materials all contribute to this enhanced sensing capability at low temperatures [10-11].

Using conducting polymers (CPs) as a sensing material is advantageous since the electronic transmission between CPs and gas molecules increases as gas vapour adsorption increases. For sensing applications, polyaniline (PANI) is widely used because of its simple synthesis, great doping/de-doping chemical reaction, high conductivity, amazing environmental stability, and good NH_3 response [12]. Xue et al. discovered that a PANI/carbon nanotube (CNT) composite outperformed pure PANI in terms of sensing performance and stability at ambient temperature [13]. PANI and SnO_2 were used to create a flexible thin-film sensor by Yu et al. For ammonia and benzene gas, the manufactured nanocomposites demonstrated an enhanced reaction time and decreased recovery time, according to the researchers' findings [14].

By drop casting a PANI/$CeFe_2O_4$ nanocomposite on flexible PET film, Saleh et al. created an ammonia gas sensor. Their findings demonstrated good ammonia gas detecting capability in the 1–50 ppm range at ambient temperature [15]. The present study discusses the production of a novel ternary nanocomposite using the conducting polymer PANI, In_2O_3 nanoparticles, and OLCs as electrode layers for gas sensors that detect ammonia at concentrations range of 25-125 ppm. TEM (transmission electron microscope), SEM (scanning electron microscope), XRD (X-ray crystallography), FTIR (fourier-transform infrared spectroscopy), and BET (Brunauer-Emmett-Teller) were used to characterize the synthesized ternary nanocomposites.

5.2 Procedure for conducting experiments

5.2.1Reagents

Dimethylformamide (DMF) was acquired from ACE chemicals and used without further purification. B-In_2O_3, Y-In_2O_3, PANI and OLCs were synthesized in this work (Chapter 3, 4 & 5) and they were also used without further treatment.

5.2.2 Synthesis of In_2O_3/PANI/OLCs nanocomposite

Known amounts (refer to table 5.1 and figure 5.1) of B/Y-In_2O_3, PANI, and OLCs were dispersed separately in known amounts of DMF, and then the B/Y-In_2O_3 and OLC solutions were

added dropwise to a PANI solution. For 48 hours, the ternary solution was agitated. After centrifuging the solution for 20 minutes, the DMF supernatant was decanted, and the In_2O_3/PANI/OLCs precipitate was oven dried for 24 hours at 100 ° C.

Table 5.1: Variation of Y-In_2O_3 and B-In_2O_3 loadings on the composites

Composites	In_2O_3	PANI	OLCs
In_2O_3/PANI/OLCs	1.5mg	30 mg	10 mg
B-In_2O_3/PANI/OLCs	3mg	30 mg	10 mg
Y-In_2O_3/PANI/OLCs	3mg	30 mg	10 mg
In_2O_3/PANI/OLCs	4.6mg	30 mg	10 mg
In_2O_3/PANI/OLCs	6mg	30 mg	10 mg

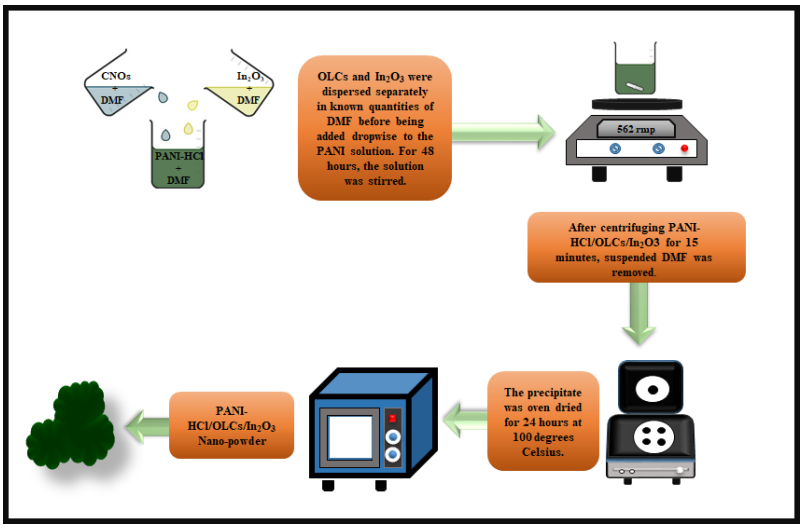


Figure 5.1 Graphical illustration synthesis of In_2O_3/PANI/OLCs

5.2.3 The preparation of sensing electrode

10 mg of each composite powder was dispersed in 8 ml of DMF, stirred for 30minutes and the solutions were sonicated for 30 minutes, after which 10 micro litters of each solution was drop casted on an interdigitated electrode and allowed to air dry for 24 hours (Figure 5.2).

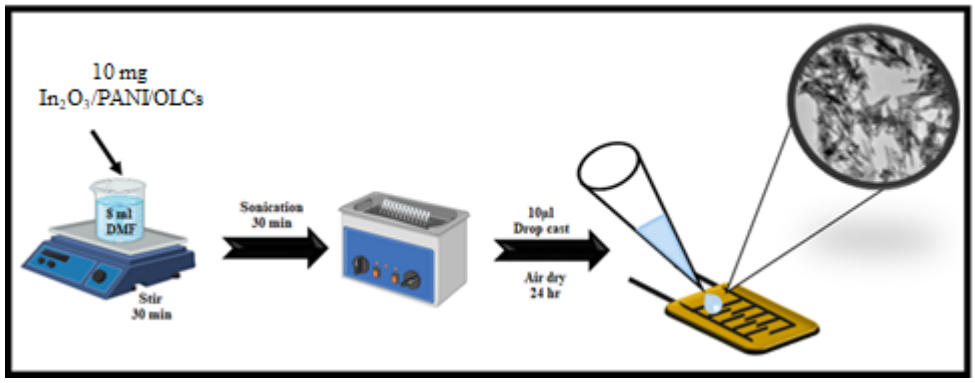


Figure 5.2 Graphical illustration of the preparation of In_2O_3/PANI/OLCs sensing electrode

5.2.4 Characterization techniques

A Bruker Tensor 27 Fourier Transform Infrared spectrometer was used for the FTIR spectroscopy analysis. On a ZEISS SIGMA, SEM analysis was performed. The TEM examination was performed at 120 kV using a Tecnai Spirit T12, and the samples were ultrasonically dispersed in ethanol before being put onto a lace carbon copper grid. PXRD data were acquired using Cu radiation on a Bruker D2 Phaser, with each scan lasting 1 hour. The PXRD metal particle sizes were calculated by applying the Scherer equation to the most prominent peaks in the relevant PXRD diffractogram using the Eva diffraction software. The surface area and pore volume were determined using a Micromeritics Tristar 3000 surface area and porosity analyser.

5.3 Discussion for conducting experiments

5.3.1 TEM

Figure 5.3 (a-e) depicts TEM images that were taken to examine the morphology of OLCs/PANI/In_2O_3 composite materials. Figure 5.3 (a) depicts the image of a B-IPC_1 composite. It is difficult to identify B-In_2O_3 nanoparticles on the composite structure due to a low B-In_2O_3 loading while a mixture of OLCs and PANI can be noticed. Figure 5.3 (b & c) exhibit B-IPC_2 and Y-IPC composites respectively. Both samples exhibit a sheet-like morphology of a mixture of OLCs and PANI with apparent (circled in blue) B-IPC_2 nanoparticles on the surface, however, Y-IPC nanoparticles appeared sparsely on the composite surface. As the mass loading of B-In_2O_3 on B-IPC_3 and B-IPC_4 was increased to 4.6 and 6 mg respectively, bigger sheets of PANI formed as illustrated by the area highlighted red cursive brackets in Figure 5.3 (d).

Because of the large mass loading, nanoparticles were more consistently distributed when compared to composites with lower indium oxide loadings. The morphology of OLCs is preserved throughout the composites, as indicated by the yellow circles.

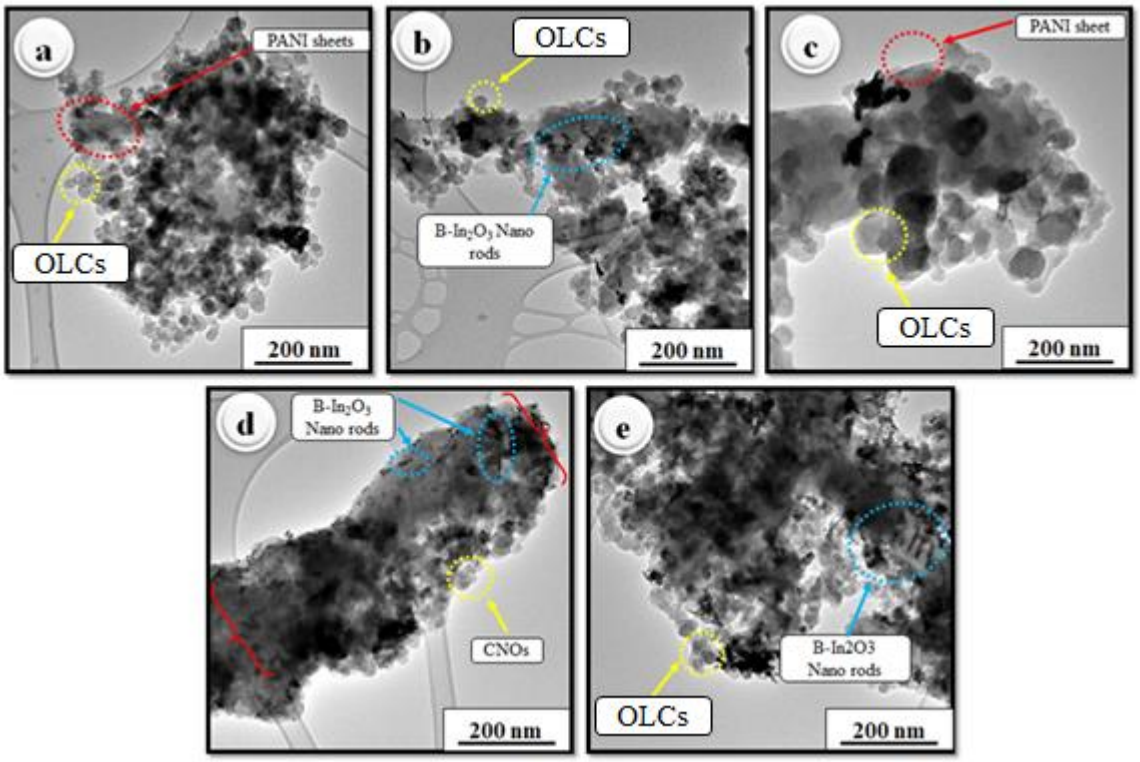


Figure 5.3 TEM micrographs of In_2O_3/PANI/OLCs composites, (a) B-IPC$_1$, (b) B-IPC$_2$, (c) Y-IPC, (d) B-IPC$_3$ and (e) B-IPC$_4$

5.3.2 SEM

SEM images of the ternary In_2O_3/PANI /OLCs composites are shown in Figure 5.4. As shown from Figure 5.4 (a), the morphology of B-IPC$_1$ appears to have formed stacked plates and cannot be differentiated from individual particles. Figure 5.4 (b) display an irregular morphology of B-IPC$_2$. The morphological examination of Y-IPC nanocomposite is shown in Figure 5.4 (c), the composite has an uneven shape and the particles are larger and smoother than those of B-IPC$_2$. In Figure 5.4 (d & e), a massive sheet-like morphology emerges alongside aggregates. Arulmani et al. described the transformation of PANI's morphology in the presence of Ni^{2+} (nickel ion) is caused by the coordination of nitrogen in the polymer backbone with Ni^{2+}, resulting in the morphological transition of nanofibers to enlarged nanofibers. They also reported that sonication facilitates the coordination [16].

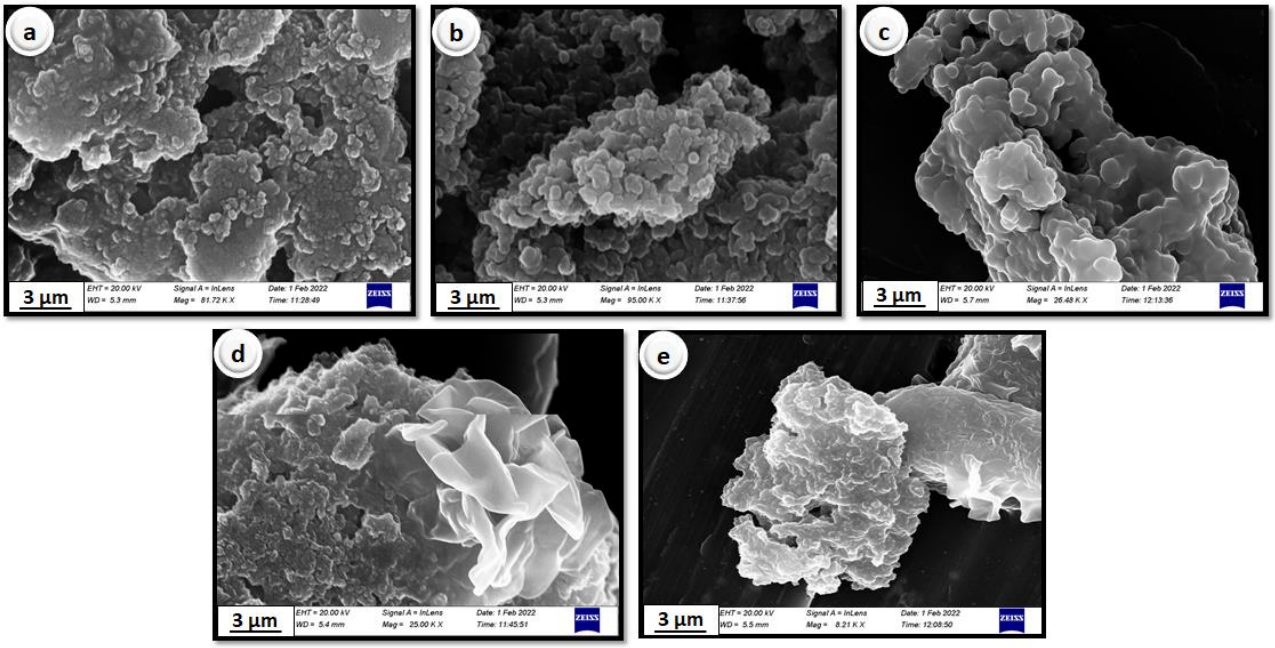


Figure 5.4 SEM micrographs of In_2O_3/PANI/OLCs composites, (a) B-IPC$_1$, (b) B-IPC$_2$, (C) Y-IPC, (d) B-IPC$_3$ and (e) B-IPC$_4$.

5.3.3 XRD

Figure 5.5 shows the XRD analysis used to study the crystalline phases of the prepared samples. The B-IPC$_1$ diffractogram displays peaks that correspond to PANI and OLCs with lower In_2O_3 loading. Both PANI and OLCs have a formation confirmation at roughly 25 θ degrees, PANI peak imbricated OLCs' peak, and this is also evident in other composites. As the indium oxide loading increases, all XRD patterns (B-IPC$_2$, Y-IPC, B-IPC$_3$ and B-IPC$_4$) reveal the presence of all constituents of the composite, and additional peaks on B-IPC$_4$ emerged (indicated by blue circles) in the composite structures, which are attributed to newly formed layers observed in Figure 5.4 (d & e), at high In_2O_3 loadings. The intensity of the In_2O_3 peaks in the Y-IPC composite is higher when compared to the intensity of the In_2O_3 in all the composites containing B-IPC, which may be owing to increased periodicity in Y-IPC nanoparticles when compared to B-IPC nanoparticles.

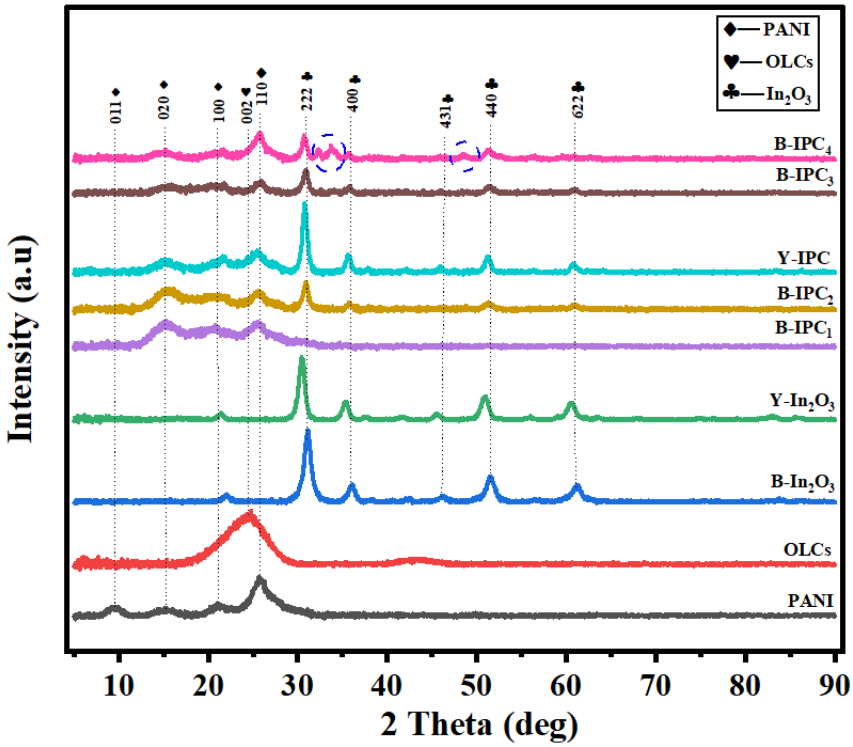


Figure 5.5 X-ray diffractogram of In_2O_3/PANI/OLCs nanocomposites

5.3.4 BET

The Brunauer-Emmett-Teller technique was used to investigate the specific surface area, pore size, and volume distribution in nitrogen adsorption and desorption environments (Figure 5.6 (a-e)). Table 5.2 lists the particulate features of samples, such as surface area, pore size, and volume distribution. For samples B-IPC_1, B-IPC_2, Y-IPC, B-IPC_3, and B-IPC_4, the BET surface areas were 20.7, 39.3, 36.9, 40.0, and 51.0 m^2/g^{-1}, respectively. The increase in B-In_2O_3 mass loading from 1.5 mg to 6 mg resulted in an increment in surface area, which can be ascribed to sufficient decorating of B-In_2O_3/OLCs on PANI matrix. When comparing Y-IPC to B-IPC_2, there is a decrease in surface area of Y-IPC, which may be due to annealing during the synthesis process of Y-In_2O_3, which led to particle expansion, resulting in a decreased surface area of Y-IPC composite. B-IPC_1 reveal an isotherm of type I that is a characteristic microporous material. At high relative pressures, Type-I isotherms exhibit a large increase in the amount of N_2 adsorbed and desorbed [16]. The rest of the composites reveal isotherms of type III that are characteristic of mesoporous materials. Pore sizes of all composites range between 4 and 50 nm (Figure 5.6 (f)).

Table 5.2 BET surface area, pore size and pore volume distribution of In_2O_3/PANI/OLCs composites

Composites	BET surface area(m^2g^{-1})	Pore volume(cm^3g^{-1})	Pore size(nm)
1,5mg (In_2O_3)/PANI/OLCs	20.7	0.020	5.3
3mg (B-In_2O_3)/PANI/OLCs	39.3	0.363	34.6
3mg (Y-In_2O_3)/PANI/OLCS	36.9	0.361	36.3
4,5mg (In_2O_3)/PANI/OLCs	40.0	0.342	32.5
6mg (In_2O_3)/PANI/OLCs	51.0	0.523	31.8

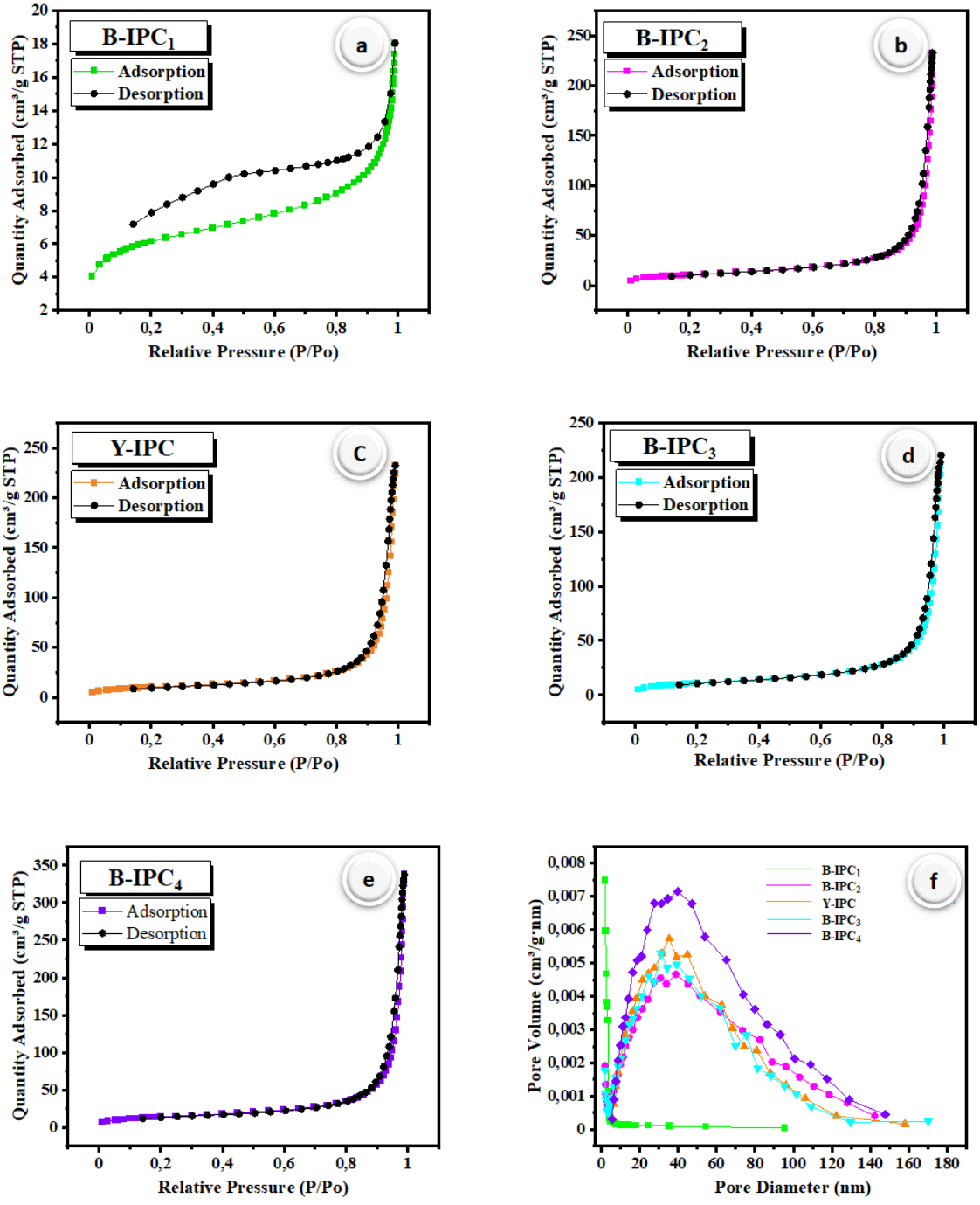


Figure 5.6 Gas adsorption-desorption isotherm curves of (a) B-IPC$_1$, (b) B-IPC$_2$, (C) Y-IPC, (d) B-IPC$_3$, (e) B-IPC$_4$ and (f) Pore size distribution curves of all composites.

5.3.5 FTIR

An infrared technique was used to investigate the bonding nature of In_2O_3/PANI/OLCs composites. Table 5.3 shows absorption bands in the composites. Interatomic vibrations in metal oxides produce absorption bands below 1000 cm^{-1} in most cases (indicated by a green rectangle), this attests that Indium oxide is present in the composite [17]. Figure 5.7 shows the absorption bands of the composites. The functional groups of OLCs are represented by the peaks indicated by the blue dot lines. A broadening peak at around 2345 cm^{-1} is due to carbon dioxide (CO_2), one of the pyrolysis (i.e. combustion) products trapped by the OLCs [18]. The band at 1749 cm^{-1} demonstrates the presence of a carboxyl group (i.e. C=O) in the OLCs structural matrix and the bands at 2001 cm^{-1} and 1082 cm^{-1} may be attributed to C-C and C-O stretching vibration modes respectively. PANI peaks are denoted by red dot lines. The peak at 2909 cm^{-1} is ascribed to aromatic bond C-H stretching vibrations induced by the chloride counter-ions. The peaks at 1580 cm^{-1} and 1475 cm^{-1} are due to the typical vibrational peaks of the PANI aromatic ring. The C=N bonds in quinoid rings and the C=C bonds in benzenoid rings are responsible for the emerged of the peak at 1280 cm^{-1}. Benzene rings have C-H bonds that vibrate both in and out of the plane, the peak at 807 cm^{-1} is caused by this.

Table 5.3 FTIR assignments bands of In_2O_3/PANI/OLCs

Wavenumber (cm^{-1})	Functional groups
2343	Atmospheric CO_2
2097	ν(C=O)
1580	C=C Quinoid rings
1475	C=C Benzenoid rings
1295	C-N in Benzenoid rings
1092	C-O Bond
807	(C-H) out of plane

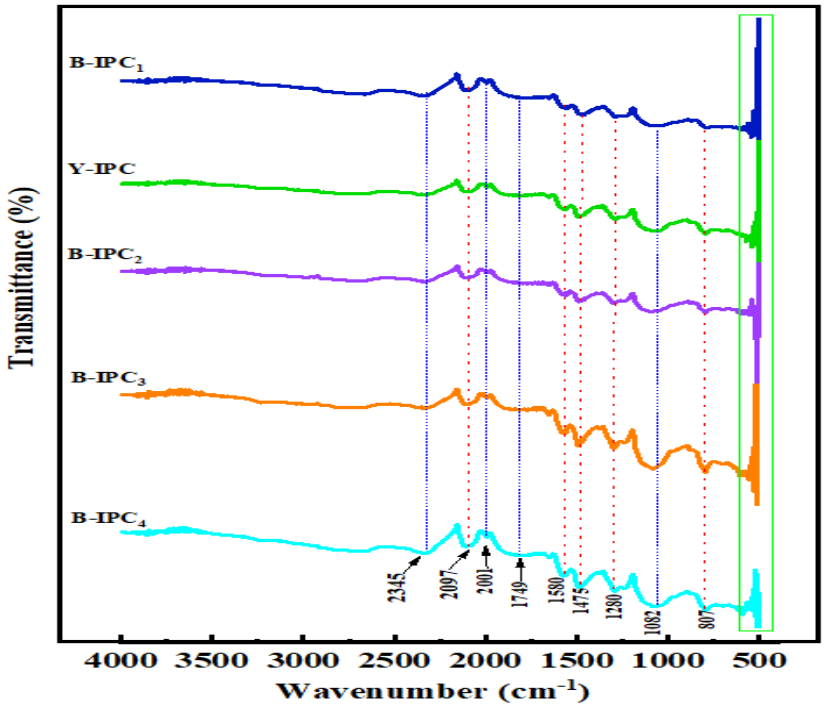


Figure 5.7 FT-IR spectra of In_2O_3/PANI/OLCs nanocomposites

5.3.2 Gas sensing applications

5.3.2.1 Plausible sensing mechanism

The p–n heterojunctions created by n-type OLCs/In_2O_3 and p-type PANI could be ascribed to another NH_3-sensing mechanism of the In_2O_3/PANI/OLCs nanofilm as depicted in figure 5.8 (a). The bandgap structure diagram in figure 5.8 (b) shows the locations of the conduction band (Ec) and valence band (Ev) in In_2O_3, HOMO (highest occupied molecular orbital) and LUMO (lowest vacant molecular orbital) for PANI, and the Fermi levels (Ef) related to the vacuum level [20-23]. PANI and In_2O_3 have band gaps of 2.96 and 3.2/3.7 eV, respectively [20]. The occurrence of a heterojunction between p-type PANI and n-type In_2O_3/OLCs nanofilms results in the formation of a changeless electronic field of depletion region. When exposed to NH_3 gas, the In_2O_3 electrons and PANI holes shift in opposite directions until the new Fermi level reaches equilibrium. The delay in electron transport from the n-type In_2O_3/OLCs nanofiber to the p-type PANI is due to the potential barrier, which increases the thickness of the depletion

layer and the sensor's resistance [20-21]. The p–n heterojunction acts as an indication amplifier, allowing for the effective detection of trace amounts of NH_3 [21].

5.3.2.2 Gas sensing measurements

All sensing experiments were conducted at room temperature with a relative humidity (RH) of 40–45%. By exposing produced sensors to varied vapour concentrations of ammonia, hexane, acetone, and isopropanol while monitoring a variation in sensor resistance at predefined time intervals, the sensing capabilities of the sensors were studied, Figure 5.8 shows (a) sensing mechanism ternary composite and (b) bandgap structure of the composite. Specific volumes (µl) of ammonia, hexane, acetone, and isopropanol were injected into a closed test chamber through the injection port using a 10 µl syringe to reach required concentrations in ppm. Equation 5.1 was used to calculate the vapour concentrations (ppm) inside the test chamber [22].Where C is the vapour concentration of the analyte in ppm, V denotes the volume of the test chamber (µl), Vs denotes the volume of analyte in liquid form (µl), is the density of in g/ml, T denotes the room temperature during testing (K), and M denotes the analyses' molar weight in g/mol.

$$C = \frac{22.4\ pTV_S}{273\ MV} \times 1000 \qquad 5.1$$

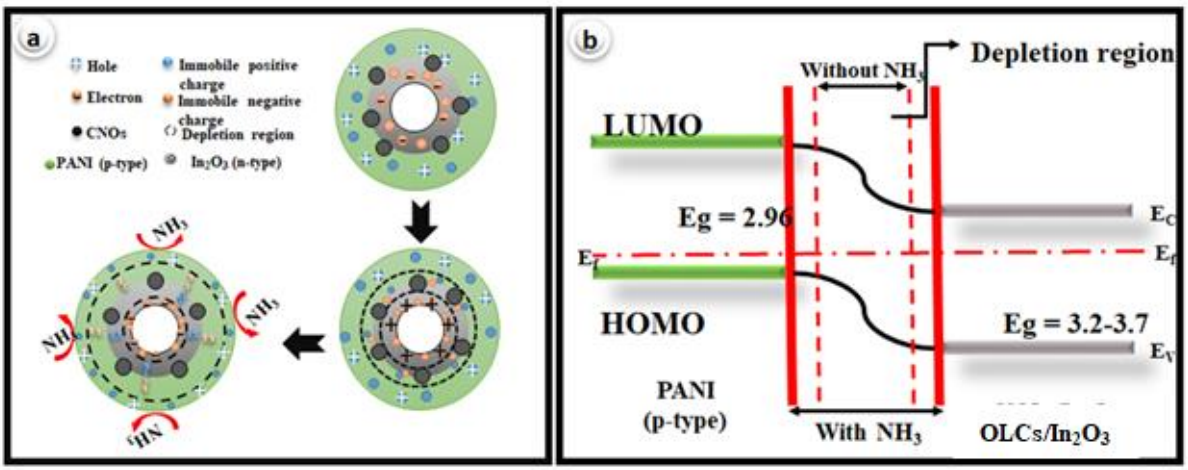


Figure 5.8 Schematic depiction of (a) sensing mechanism and (b) bandgap structure diagram of In_2O_3/PANI/OLCs nanocomposites (adopted from [20])

Particular volumes of ammonia, hexane, acetone, and isopropanol in microliters were injected separately inside a closed test chamber using a micro syringe for gas sensing measurements (Figure 5.9). Resistance increased after a brief induction period, indicating that a chemical change had occurred on the detecting film's surface. This chemical change was translated into a legible output signal, such as a change in resistance signal, by the LCR 6300 multimeter (response). To reverse the chemical change, a vacuum pump was used to pump out the gas analyte inside the test chamber and replace it with ambient air. A response vs recovery phenomenon [23] is another name for this reversible process. Changes in resistance were calculated as a function of analyte gas concentrations in this study.

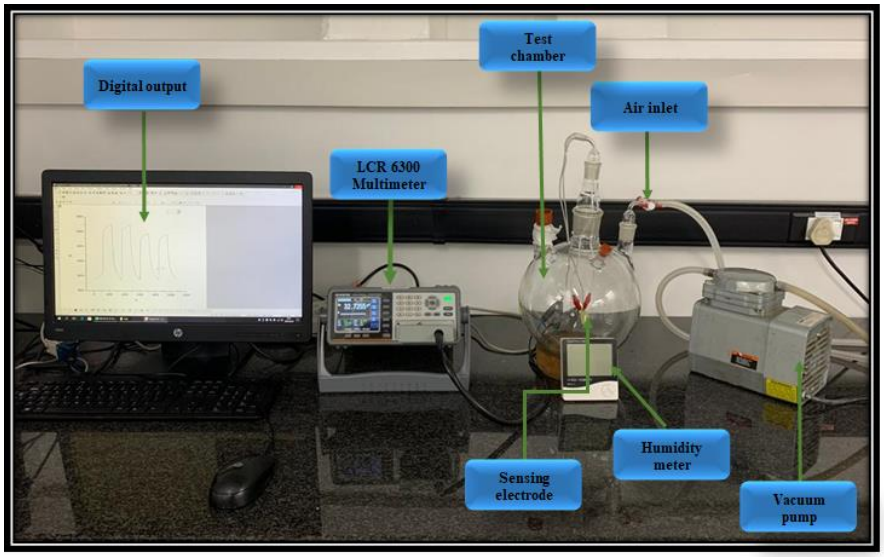


Figure 5.9 Image of gas sensing equipment used in this study

5.3.2.3 NH_3 sensing performance of In_2O_3/PANI/OLCs nanocomposite

The In_2O_3/PANI/OLCs nanocomposite sensor was used to detect NH_3 at room temperature at concentrations ranging from 25 ppm to 125 ppm and to assess the NH_3-sensing capability of the composite sensor, which can be used in the automotive and chemical industries. Figure 5.10(b) compares the NH_3, sensing performance of the In_2O_3/PANI/OLCs sensor to that of the PANI, OLCs and PANI/OLCs sensors. It is clear that composite sensors have a higher response than sensors that solely contain PANI, OLCs, or PANI/OLCs.

Figure 5.10 (a) depicts the detecting performance of five In_2O_3/PANI/OLCs ternary nanocomposite sensors; the results indicate that all five sensors' responses had nearly the same pattern, but the response values of the sensors at the same concentration were extremely diverse. The B-IPC$_4$ sensor undoubtedly had the highest response of the five sensors tested. Since B-IPC$_4$ has the highest response among all sensors, response time, reproducibility, and the ability to detect other gases was primarily reported on it; however, as stated in Chapter 3, the efficacy of sensors based on B-In_2O_3 and Y-In_2O_3 was also compared.

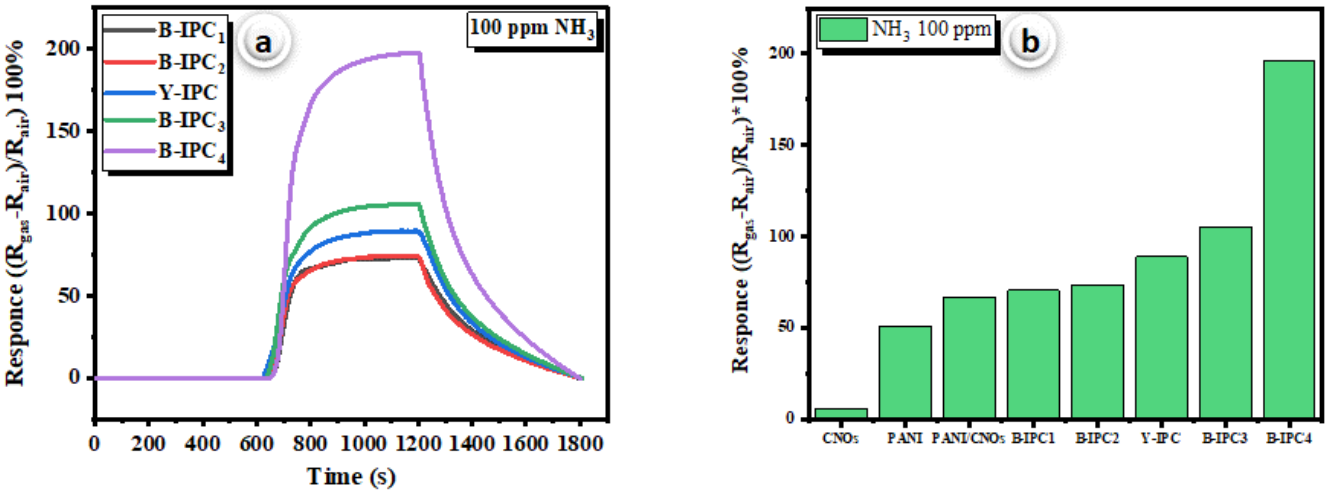


Figure 5.10 (a) dynamic response–recovery curves of In_2O_3/PANI/OLCs and (b) response of all nanocomposite constituents

5.3.2.4 Sensing performance of B-IPC$_4$

The B-IPC$_4$ sensor is shown in Figure 5.11(a) detecting ammonia NH_3 at concentrations ranging from 25 ppm to 125 ppm. These results demonstrate that the sensor's response increases rapidly as the concentration of NH_3 increases and subsequently decreases significantly to its initial value following exposure of the sensor to air. The response and recovery times of any sensor are among the most essential factors; they indicate how quickly the sensor responds in the vicinity of analyte vapour and how quickly it can recover in air (after exposure to the analyte is terminated). As a result, the response time was considered a prerequisite for the sensor to attain 90% of its maximum response (saturation) after the test gas was injected, and the recovery time was described as the time needed for the sensor to regain 90% of its response after the analyte gas was removed [24]. Sensor B-IPC$_4$ had the reaction time of 2.2 minutes and the recovery time of 4.6 minutes at 100 ppm ammonia concentration (see Figure 5.11 (b)). At 100 ppm of analyte vapour concentration, the repeatability of the B-IPC$_4$ sensor was evaluated. The

test was repeated four times, as indicated in figure 6.11(c); after four rounds, the sensor retained its initial sensing capabilities without losing sensitivity. Figure 6.11(d) shows the sensitivity curve derived from dynamic response-recovery curve of B-IPC$_4$, with 0.6434 ppm and R^2 value of 0, 9986.

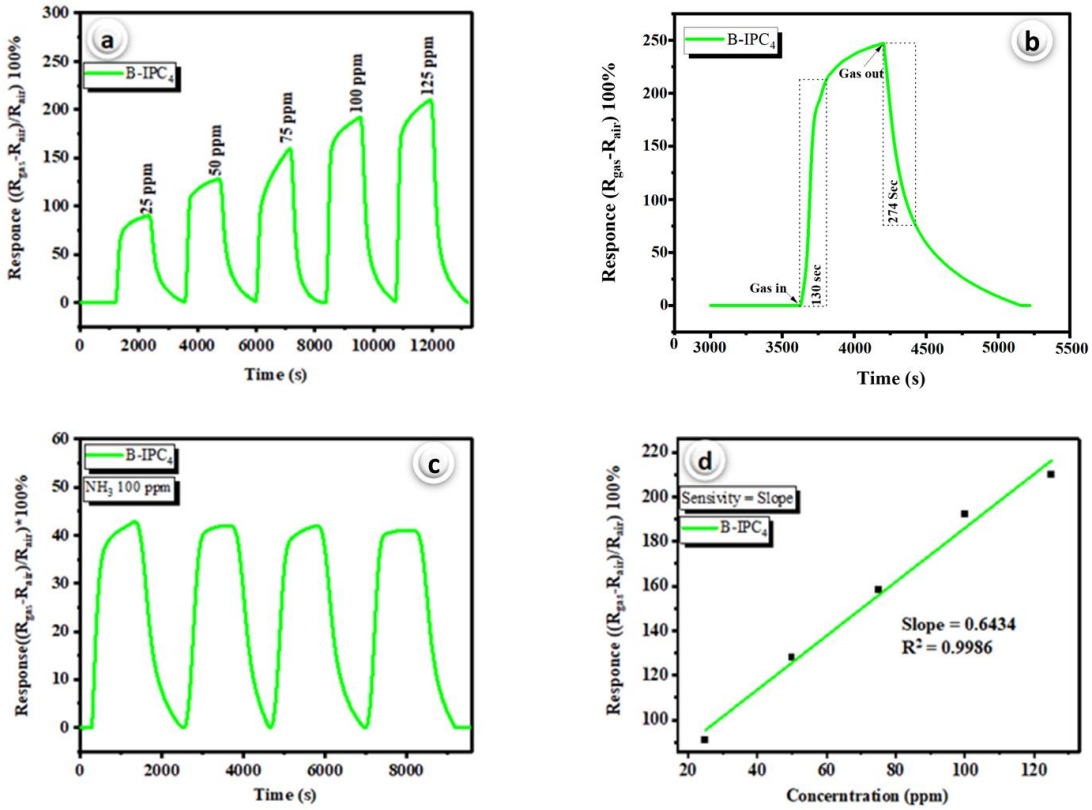


Figure 5.11 (a) dynamic response-recovery curve, (b) response-recovery time plot, (c) reproducibility curves and (d) sensitivity curve of B-IPC$_4$ sensor

The selectivity of synthetic gas sensors is crucial for practical applications. Actually, gas sensors are typically exposed to a wide range of analytes, and it is presumed that the analyte of interest is accurately detected without interference from other gases. At a concentration of 100 ppm, Figure 5.12 shows the selectivity of the B-IPC$_4$ sensor toward ammonia (NH_3), isopropanol (C_3H_8O), hexane (C_6H_{14}), and acetone (CH_3COCH_3). It was clearly demonstrated that the B-IPC$_4$ sensor had a high-level response characteristic to ammonia but little response to other gases.

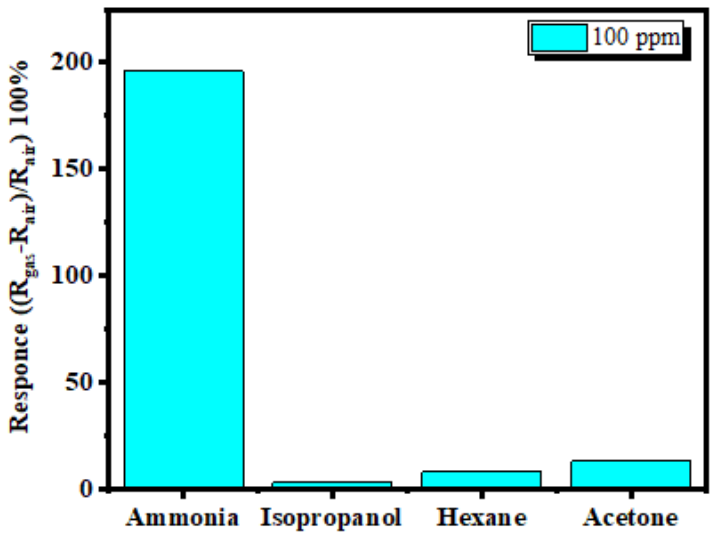


Figure 5.12 The selectivity of B-IPC$_4$ tested at 100 ppm towards NH_3, C_3H_8O, C_6H_{14} and CH_3COCH_3

5.3.2.5 NH_3 sensing performance of Y-In_2O_3 and B-In_2O_3

The response curves for B-IPC$_2$ and Y-IPC are depicted in figure 5.13(a). In the concentration range of 25 ppm to 125 ppm of NH_3 at ambient temperature, Y-IPC exhibits the strongest response compared to B-IPC$_2$. Figure 5.13 (b) depicts the gradients of the plots which were utilized to determine the sensors' sensitivities, the estimated gradients of 0.432 ppm and 0.320 ppm belong to gas sensors Y-IPC and B-IPC$_2$, correspondingly. Y-IPC had an R^2 value of 0.9263 while sensor B-IPC$_2$ had an R^2 value of 0.9901. The R^2 value for B-IPC$_2$ is greater than that for Y-IPC, because the graph demonstrated a more linear relationship. This is due to the reduction free accessible volume required for vapour diffusion due to the particle sizes (refer to table 3.1.3) [25, 26] small particle size results in increased vapour diffusion on the sensing material's surface. Over four cycles, the repeatability of both sensors was determined, and both sensors preserved their sensitivities. Response times were 2.4 minutes for B-IPC$_2$ and 2.8 minutes for Y-IPC, and recovery times were 5.4 minutes for both B-IPC$_2$ and Y-IPC at 100 ppm ammonia concentration.

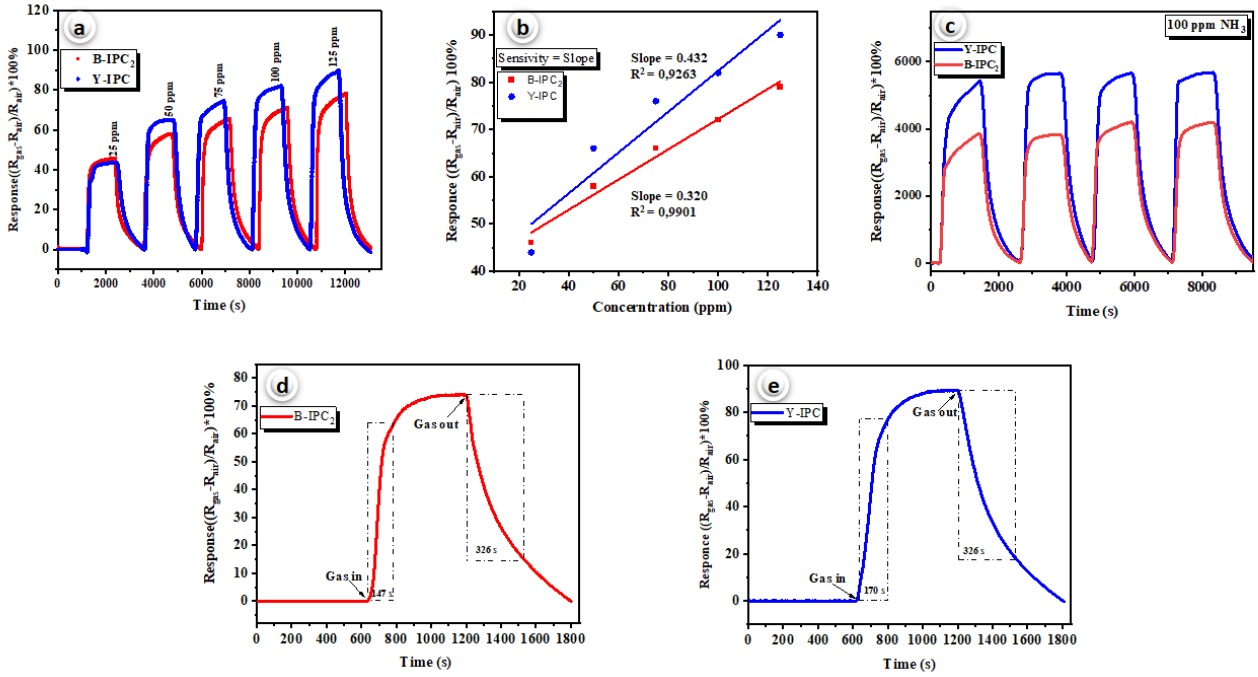


Figure 5.13 (a) Response–recovery curves, (b) sensitivity curves of B-IPC$_4$ & Y-IPC, (c) reproducibility curves, (d) and response-recovery time plots of B-IPC$_2$ & Y-IPC sensors

5.4 Conclusion

In_2O_3/PANI/OLCs hybrids as sensing materials were successfully fabricated. TEM and SEM revealed that mass loading increment of Y/B-In_2O_3 led to the emergence of sheet-like morphology of PANI nanofibers. The presence of the principal bands of all constituents in FTIR verified the development of Y/B-In_2O_3/PANI/OLCs composites. XRD analysis revealed that the prepared composites are polycrystalline, with the appearance of new additional peaks as the indium oxide loadings increased. The BET surface area rose as the metal loading increased, and the composites have pore diameters ranging from 4 to 40nm. Sensors based on the Y/B-In_2O_3/PANI/OLCs ternary nanocomposite were successfully fabricated; sensor B-IPC$_4$ demonstrated the highest response of all sensors, with response and recovery times of 2.2 minutes and 4.6 minutes, respectively. B-IPC$_4$ was found to be selective for ammonia when tested against NH_3, C_3H_8O, C_6H_{14}, and CH_3COCH_3. Y-IPC sensor outperformed B-IPC$_2$ sensor in terms of response.

5.5 References

[1] Kohl, D. (2001). Function and application of gas sensors. Topical review, pp. 125-149.

[2] Docquier, N., & Candel, S. (2002). "Combustion control and sensors. Energy combustion science, vol. 28, pp. 107-150. Doi: 10.1016/S0360-1285(01)00009-0

[3] Riegel, J., Neumann, H.D., & Wiedenmann, H. (2002). Exhaust gas sensors for automotive emission control. Solid State Ionics, 152, 783-800.

[4] Chauhan, P.S., & Bhattacharya, S. (2019). Hydrogen gas sensing methods, materials, and approach to achieve parts per billion level detection: A review. International Journal of Hydrogen Energy.

[5] Mariammal, R.N., Ramachandran, K., Renganathan, B., & Sastikumar, D. (2012).On the enhancement of ethanol sensing by CuO modified SnO_2 nanoparticles using fibre-optic sensors. Sensors and Actuators B: Chemical, 169, pp. 199-207

[6] Matawee P et al. (2017).Roles of cobalt doping on ethanol sensing mechanisms of flame spray-made SnO_2 nanoparticles-electrolytically exfoliated graphene interfaces. Applied surface science, 425, pp. 351-366, 2017.

[7] Shankar, P., & Bosco, J. Monomer design of ZnO nanostructures (nanobush and naonowire) and their room-temperature ethanol vapour sensing signatures.(2017).ACS applied material,9(43), pp. 38135-38145.

[8] Hong, S.Z et al.(2021)The room temperature highly sensitive ammonia gas sensor based on polyaniline and nitrogen-doped graphene quantum dot-coated hollow indium oxide nanofiber composite," Polymers (Basel), 13 (21), pp. 3676.

[9] Yavari,F, F., & Koratkar, N. (2012).Graphene-based chemical sensors," The journal of physical chemistry letters, 3(13), pp. 1746-1753.

[10] Liu, X., Li, L., Meng, C., & Han, Y. (2012).Palladium nanoparticles/defective graphene composites as oxygen reduction electrocatalysts. The journal of physical chemistry, 116(4), pp. 2710-2719.

[11] Zhao, C., & Wu, H. (2018).A first-principles study on the interaction of biogas with noble metal (Rh, Pt, and Pd) decorated nitrogen-doped graphene as a gas sensor: A DFT study. Applied surface science.435, pp. 1199-1212.

[12] Zhu, C et al. (2018).Enhanced sub-ppm NH_3 gas sensing performance of PANI/TiO_2 nanocomposites at room temperature. Front chemistry.6, pp. 493.

[13] Xue, L et al. (2017).Flexible polyaniline/carbon nanotube nanocomposite film-based electronic gas sensors. Sensors and actuators B, vol. 244, pp. 47-53.

[14] Feng, Q et al. (2021).Preparation and gas sensing properties of PANI/Sn_2O hybrid material. Polymers, 13(9), p. 1360.

[15] Yang, W., Shen, H., Ge, J., & Xu, B.(2021).Improving TiO_2 gas sensing selectivity to acetone and other gases via a molecular imprinting method. Nanotechnology, 32, 155503

[16] Zengyang, P et al. (2016).A room temperature ammonia gas sensor based on cellulose/TiO_2/PANI composite nanofibers. Colloids Surface, pp. 248-255.

[17] Zhang, D., Wu, Z., Li, P., Zong, X., Dong, G., & Zhang, Y. (2018). Facile fabrication of polyaniline/multi-walled carbon nanotubes/molybdenum disulphide ternary nanocomposite and its high-performance ammonia-sensing at room temperature. Sensors and Actuators B-chemical, 258, 895-905.

[18] Alharthy, R.D., & Saleh, A. (2021).A novel trace-level ammonia gas sensing based on flexible PANI-$CoFe_2O_4$ nanocomposite film at room temperature. Polymers, .13(18), pp. 3077.

[19] De azevedo, W.M. (2001).Polyaniline-poly (Vinyl alcohol) conducting composite material with easy processabilty and novel application potential," Synthetic metals, 123(1), pp. 21-31.

[20] Shankarananda, A., Lagashetty, A., & Kalyani, S. (2009).Chemical oxidation method for the synthesis of polyaniline-In_2O_3 composite," Polymer composites, 1(10), pp. 59-64.

[21] Blacic, J., Mathez, E., Maggiore, C., Mitchell, T. & Fogel, R. (1991). Oxygen in Diamond by the Nuclear Microprobe: Analytical Technique and Initial Results. International Kimberlite Conference: Extended Abstracts. 5, (Feb. 1991), 20–22. DOI:https://doi.org/10.29173/ikc2449

[22] Wang,X., Cui,F., Lin,J., Ding,B., Yu,J., Al-Deyab,S.S. (2012).Functionalized nanoporous TiO_2 fibres on quartz crystal microbalance platform for formaldehyde sensor," Sensors and actuators B, 171, pp. 658-665, 2012.

[23] Nalage, SR et al. (2015).Preparation of camphor-sulfonic acid doped PPy-NiO hybrid nanocomposite for the detection of toxic nitrogen dioxide. Synthetic metals, 209, pp. 426-433.

[24] Okechukwu,V,O.,Mavumengwana,V., Ivo A. Hümmelgen,A.I., & A.M, Mamo.(2019).Concomitant in Situ FTIR and Impedance Measurements to Address the 2-Methylcyclopentanone Vapor-Sensing Mechanism in MnO_2–Polymer Nanocomposites," ASC Omega, 4(5), pp. 8324-8333.

5.6 Supplementary data

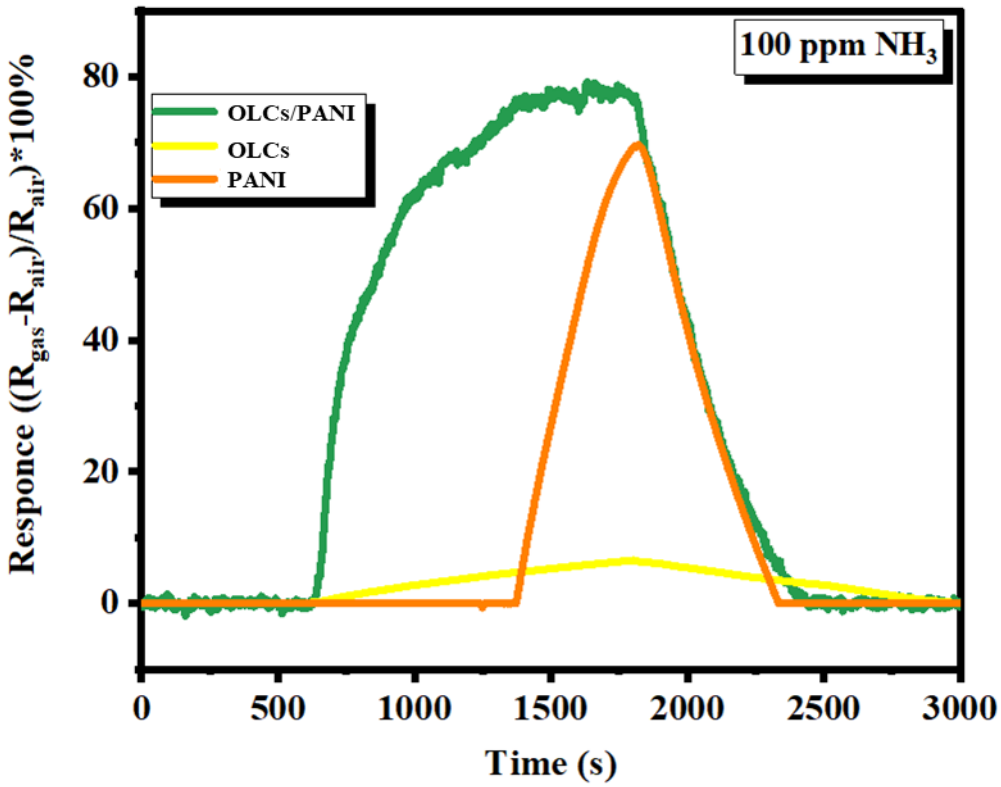


Figure 5.14 Response–recovery curves for bare PANI/OLCs and PANI/OLCs

CHAPTER 6

CONCLUSIONS AND RECOMMENDATIONS

6.1 General conclusions

The overall goal of this work was to develop room-temperature gas sensors on the basis of In_2O_3/PANI/OLCs ternary nanocomposite using In_2O_3 material obtained through green chemical methods. As of yet, no reports have described a room temperature gas sensor using the above-mentioned composite. The outcomes of experiments presented in chapters 3, 4, 5, and 6 reveal that the precise objectives outlined in chapter 1 were met. Study findings are summarized as follows:

Historically, In_2O_3 materials have been obtained through simple chemical methods. However, microwave hydrothermal processing has rarely been used to fabricate these materials. The solution-phase approach and ligand-free method were used successfully to synthesize Y-In_2O_3 nanograins and B-In_2O_3 nanorods, with the use of microwave radiation at 700 watts for ten minutes. The average crystallite size of B-In_2O_3 and Y-In_2O_3 was estimated at approximately 9.4 nm and 10.7 nm, respectively. A variety of characterizations were performed, including TEM, SEM, XRD, FT-IR, UV-vis, BET and XPS.

A rapid polymerization method was used to produce PANI nanofibers with an average size of around 37 ± 9nm utilizing aniline as a monomer and ammonium sulphate as an oxidant. The conductivity of polyaniline was enhanced by doping it with 1M of HCl. Analysis of XRD patterns and UV-vis spectroscopy confirmed the doping effectiveness. Additional characterizations by FTIR and BET, confirmed successful formation PANI, due to the existence of 1632 cm^{-1} and 1474 cm^{-1} vibration modes (FTIR), which were ascribed to the quinoid and benzenoid rings, and BET surface area was found to be 30.2 m^2g^{-1}. A flame pyrolysis method was used to produce quasi-spherical onion like-carbon from candle wax. The particles were 39 ± 9 nm in diameter and exhibited Raman spectroscopy-confirmed D- and G-bands at 1337 cm^{-1} and 1592 cm^{-1}, respectively. A thermal stability of about 667 ° C and a BET surface area of 85.7 m^2g^{-1} were also determined for the OLCs.

Synthesis of In_2O_3/PANI/OLCs nanocomposites was achieved through physical mixing, and the effect of In_2O_3 loadings were studied using TEM, SEM, XRD, FT-IR, and BET. According to the results, different loadings of In_2O_3 into the composites resulted in a notable increment in the BET specific surface areas, in contrast to the bare constituents of the composites. Furthermore, at higher indium oxide loadings ((4.6 mg) B-In_2O_3/PANI/OLCs), additional peaks in XRD were discovered, which are attributed to newly formed layers observed in SEM analysis, figure 6.4 (d &e), at high In_2O_3 loadings.

Various sensors were used to study sensing of NH_3 at room temperature conditions by comparing sensing performance of In_2O_3/PANI/OLCs nanocomposites at different Y/B-In_2O_3 loadings to that of bare PANI, OLCs and PANI/OLCs. The sensors that incorporated the composites had a higher ammonia response. When subjected to 100 ppm ammonia vapours for up to four cycles, composites sensors displayed good repeatability of the sensing signal. When sensors made from Y-In_2O_3 (Y-IPC) and B-In_2O_3 (B-IPC_2) were compared towards ammonia sensing at 100 ppm concentration, they both had a similar response and recovery times of 2.8 and 5.4 minutes ,2.5 and 5.4 minutes, respectively, and the sensor made from Y-In_2O_3 (Y-IPC) had a relatively higher response. The (4.6 mg) B-In_2O_3/PANI/OLCs (B-IPC_4) sensor demonstrated a response time of 2.2 minutes and a recovery time of 4.6 minutes when exposed to ammonia vapour at 100 ppm concentration. Furthermore, due to the high response values when compared to other sensors, the B-IPC_4 was tested for the detection of hexane, isopropanol, and acetone; the response for ammonia was significantly high in comparison. The high response observed for the (4.6 mg) B-In_2O_3/PANI/OLCs sensor was attributed to the high surface porosity, which allowed for efficient analyte gas adsorption and desorption.

7.2 Recommendations

The rod morphology of the indium oxide synthesized in the presence of the ethanol solvent was unique and this could be interesting to investigate for future electronic applications. New approaches for the synthesis of In_2O_3/PANI/OLCs nanocomposites should be investigated in order to improve overall morphological outline. Atomic force microscopy study of the sensing devices should be performed to ascertain their surface roughness and layer thickness. More research on the synergistic effects of In_2O_3/PANI/OLCs should be conducted to improve sens-

ing and better understand the underlying sensing mechanisms. The influence of humidity fluctuations on our composites' sensing behaviour should also be explored. Furthermore, it is recommended that all the sensors be investigated in the future in order to discuss the sensor's response and recovery times, state of linearity, and the type of response. As such, the statement "The dynamic characterization (i.e., response and recovery time as well as sensitivity) for B-IPC_1, B-IPC_2, B-IPC_3, and Y-IPC should be investigated and contrasted or compared with that of B-IPC_4" , Furthermore, because the source of NH_3 is ammonia solution (NH_3OH), which contains approximately 25% NH_3, appropriate calculations should be performed before calculating ammonia concentrations to be detected.